
13

OPTICAL MEASUREMENT TECHNIQUES: FUNDAMENTALS AND APPLICATIONS

CHRISTOPHER M. SORENSEN

Department of Physics, Kansas State University, Manhattan, Kansas

JOSEF GEBHART

Dietzenbach, Germany

TIMOTHY J. O'HERN AND DANIEL J. RADER

Sandia National Laboratories, Albuquerque, New Mexico

13.1	Introduction	270	13.2.6	Multiple Scattering	280
13.2	Light Scattering and Extinction Theory	270	13.2.7	Scattering from Ensembles of Particles	281
13.2.1	Cross Sections	270	13.2.8	Nonspherical Particles	281
13.2.1.1	The Differential Cross Section	270	13.3	Dynamic Light Scattering	281
13.2.1.2	The Total Scattering Cross Section	271	13.3.1	DLS Experimentation	281
13.2.1.3	Efficiencies	271	13.3.2	Flowing Systems	283
13.2.1.4	Extinction and the Albedo	271	13.4	Experimental Methods for the Laboratory	283
13.2.1.5	Polarization	271	13.5	Optical Measurement Techniques: <i>Ex Situ</i> Sensing	284
13.2.2	Small Particles: Rayleigh Scattering	272	13.5.1	Introduction	284
13.2.2.1	Introduction	272	13.5.2	Single Particle Optical Counters	284
13.2.2.2	Rayleigh Differential Cross Section	273	13.5.2.1	General Remarks	284
13.2.2.3	Rayleigh Total Cross Section	273	13.5.2.2	Calibration Procedures	285
13.2.2.4	Rayleigh Absorption Cross Section	274	13.5.2.3	Optical Systems	285
13.2.2.5	Rayleigh Extinction Cross Section	274	13.5.2.4	Pulse Processing	288
13.2.3	“Soft” Particles: Rayleigh-Debye-Gans Scattering	274	13.5.2.5	Range of Number Concentration	288
13.2.4	Spheres of Arbitrary Size and Refractive Index: The Mie Theory	276	13.5.2.6	Sensitivity and Sample Flow Rate	290
13.2.4.1	The Mie Differential Cross Section	276	13.5.2.7	Sizing Accuracy and Resolving Power	292
13.2.4.2	The Mie Guinier Regime	277	13.5.3	Multiple Particle Optical Techniques	293
13.2.4.3	The Mie Ripples	278	13.5.3.1	General Considerations	293
13.2.4.4	The Mie Total Cross Section	278	13.5.3.2	Performances in Use	294
13.2.5	Rayleigh-Debye-Gans Fractal Aggregate Scattering	279	13.6	Optical Measurement Techniques: <i>In Situ</i> Sensing	295
13.2.5.1	Fractal Aggregates	279	13.6.1	Introduction	295
13.2.5.2	Scattering and Absorption by Fractal Aggregates	279	13.6.2	Overview	296
			13.6.2.1	Particle Properties	297
			13.6.2.2	Instrument Properties	297
			13.6.2.3	Environmental Properties	299

13.6.3	Single Particle Counters: Intensity-Based	299	13.6.3.6	Single Particle Counters: Phase-Based	302
13.6.3.1	Forward-Scattering Spectrometer Probe	299	13.6.3.7	Phase Doppler Particle Analyzer	303
13.6.3.2	90° White Light-Scattering Analyzers	300	13.6.3.8	Particle Dynamics Analyzer	303
13.6.3.3	Particle Counter Sizer Velocimeter (PCSV)	301	13.6.3.9	Phase Doppler Performance and Applications	303
13.6.3.4	Dual-Beam and Top-Hat Beam Systems	301	13.6.4	Single Particle Counters: Imaging	305
13.6.3.5	Single Particle Counters: Laser Doppler Velocimetry Visibility Based	302	13.7	Conclusions	305
			13.8	List of Symbols	306
			13.9	References	307

13.1 INTRODUCTION

We see the physical universe around us via light scattering. This is true except for the few luminous objects in our world, such as the sun or various light sources, which provide their own light. Everything else, the blue of the sky, the white of clouds, the faces of our friends, and this page of this book, scatters light to our detecting eyes. The scientist takes advantage of light scattering by systematic and quantifiable observation to use light scattering as a probe of material systems. Our concern here is largely aerosol systems and one quickly appreciates the importance and potential usefulness of light scattering when the word “aerosol” engenders in the mind’s eye a *cloud* of particles.

Light scattering in aerosol science provides a method to probe unobtrusively and in real time such systems to determine size, morphology, and concentration of the constituent particles, and the dynamics of their motion, aggregation, or dissipation. Moreover, particles in our environment scatter and absorb light and thereby affect visibility and the earth’s global environment.

This chapter will describe light scattering and absorption due to particles relevant to aerosol science. It will also describe application of light scattering and absorption to various measurement techniques designed to obtain information regarding the concentration and size distribution of particles in aerosol systems. As such it is divided into two major sections. The first section presents a modern review of theoretical results for light scattering and extinction. In the second section, excellent reviews by Gebhart (2001) and Rader and O’Hern (2001) of application of the light-scattering theory for instruments and techniques to make both *ex situ* and *in situ* measurements of aerosol systems will be revisited.

13.2 LIGHT SCATTERING AND EXTINCTION THEORY

The bulk of this section will describe static light scattering which involves the angular scattering pattern, total scattering,

and absorption. The development here contains all the usual pieces but relates them in an unconventional manner. The general description for scattering from an arbitrary sphere, so-called Mie scattering, is shown to have patterns that evolve from the simpler models of scattering that rely solely on wave diffraction. These patterns lend order to the complex results and physical intuition for the most complex situations. Regardless of the novel approach, the results are the same. For more extensive treatments of static light scattering the reader can look to some classic books on the subject (Kerker 1969; van de Hulst 1981; Bohren and Huffman 1983; Mishchenko et al. 2002). A brief description of dynamic light scattering is also given. Dynamic light scattering makes use of temporal fluctuations in the scattered light that are related to the diffusive motion of particles that in turn are related to the particle size. More extensive treatments of dynamic light scattering are described in Berne and Pecora (1976).

13.2.1 Cross Sections

13.2.1.1 The Differential Cross Section The differential scattering cross section, $dC_{\text{sca}}/d\Omega$, describes the power scattered, P_{sca} , per unit solid angle, Ω (W/steradian), for an incident intensity¹ (W/m^2) I_0 .

$$\frac{P_{\text{sca}}}{\Omega} = \frac{dC_{\text{sca}}}{d\Omega} I_0 \quad (\text{Eq. 13-1})$$

Thus, the units of $dC_{\text{sca}}/d\Omega$ are $\text{m}^2/\text{steradian}$.

The scattered intensity is the scattered power per unit area of detection

$$I_{\text{sca}} = P_{\text{sca}}/A \quad (\text{Eq. 13-2})$$

The solid angle subtended by the detector a distance r from the scatterer is

$$\Omega = A/r^2 \quad (\text{Eq. 13-3})$$

¹Precisely speaking, W/m^2 is an *irradiance*, watts/steradian is an *intensity*, but common usage often finds *intensity* applied to W/m^2 .

Thus, from Equations 13-2 and 13-3, we obtain

$$I_{\text{sca}} = I_0 \frac{dC_{\text{sca}}}{d\Omega} \frac{1}{r^2} \quad (\text{Eq. 13-4})$$

This equation contains the well-known $1/r^2$ dependence due to the three-dimensional (3D) geometry of space. Note that the scattered intensity is directly proportional to the differential cross section. Because of this, they will often be referred to in a synonymous manner.

13.2.1.2 The Total Scattering Cross Section The total scattering cross section is found by integration of the differential cross section over the entire solid angle

$$C_{\text{sca}} = \int_{4\pi} \frac{dC_{\text{sca}}}{d\Omega} d\Omega \quad (\text{Eq. 13-5})$$

This integral must include polarization effects described below. The differential element $d\Omega$ in 3D Euclidean space is

$$d\Omega = d\theta d(\cos \varphi) \quad (\text{Eq. 13-6})$$

(See Fig. 13-1, below, for the polar coordinates θ and φ .)

13.2.1.3 Efficiencies The efficiency Q for scattering or absorption is a dimensionless ratio of either total cross section to the projected, along the incident direction onto a plane, area of the scatterer:

$$Q_{\text{sca or abs}} = \frac{C_{\text{sca or abs}}}{A_{\text{proj}}} \quad (\text{Eq. 13-7})$$

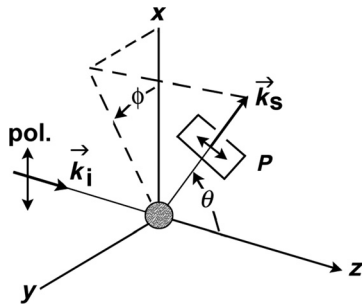


Figure 13-1 Geometry of scattering for an incident light wave traveling along the positive z axis with propagation direction defined by the incident wave vector \vec{k}_i and with polarization (pol.) in the vertical x direction. Light is scattered from the small, spherical particle to the detector in the direction of the scattering wave vector \vec{k}_s . The scattered polarization will be in the direction of the projection of the incident polarization at the scatterer onto the plane P , which is perpendicular to the detector direction \vec{k}_s .

For a sphere of radius a

$$A_{\text{proj}} = \pi a^2 \quad (\text{Eq. 13-8})$$

Efficiencies are physically intuitive because they compare the optical cross section to the geometric cross section. If light were not a wave, that is, solely a particle, the sum of the scattering and absorption efficiencies would be unity independent of size.

13.2.1.4 Extinction and the Albedo Attenuation of light when it passes through a system of particles is called extinction. It is described by an exponential decrease of the intensity as it passes through the medium known as the Lambert-Beer law

$$I_{\text{trans}} = I_0 e^{-\tau x} \quad (\text{Eq. 13-9})$$

Here τ is the turbidity of the medium. The turbidity is related to the number density of particles n and their individual extinction cross section C_{ext} by

$$\tau = n C_{\text{ext}} \quad (\text{Eq. 13-10})$$

Extinction is due to both scattering, which deviates light from the incident path direction, and absorption, which converts the light into other forms of energy (e.g., heat),

$$C_{\text{ext}} = C_{\text{abs}} + C_{\text{sca}} \quad (\text{Eq. 13-11})$$

The albedo, ω , is the ratio of scattering to extinction

$$\omega = C_{\text{sca}} / C_{\text{ext}} \quad (\text{Eq. 13-12})$$

A related parameter is the Rayleigh ratio which for a particulate system is equal to the scattering cross section, either differential or total, times the particle number density. Hence Rayleigh ratios have units of either (meters · steradian) $^{-1}$ or meters $^{-1}$. Rayleigh ratios are usually used in the context of describing light scattering and attenuation in gases and liquids (Kerker 1969).

13.2.1.5 Polarization The polarization direction of light is parallel to its electric field vector. This is always perpendicular to the direction of propagation and hence there are two independent polarizations. Natural light that is emitted by the sun and typical home and industrial sources such as light bulbs and fluorescent lights has waves with random polarizations. This situation can be resolved into equal amounts of two independent polarizations. Such light is sometimes called “unpolarized,” but this is a bit of a misnomer and “randomly” polarized might be a better term. Modern scientific light sources are usually lasers, and these are very often, but not always, polarized. A typical laboratory setup positions a laser shining its beam in the horizontal direction with the polarization in the vertical direction. This

configuration will be used to describe scattering. From this the rules for scattering in other arrangements and for natural, “unpolarized” light are easily perceived.

Consider a light wave traveling in the positive z direction incident upon a particle at the origin as drawn in Figure 13-1. The direction of propagation is described by the incident wave vector \vec{k}_i with magnitude $|\vec{k}_i| = 2\pi/\lambda$ where λ is the wavelength of the light in the medium. The incident light is polarized along the vertical x axis. The y - z plane is horizontal and is called the “scattering plane.” Light is scattered in the direction of the scattered wave vector \vec{k}_s . We consider only elastic scattering; hence,

$$|\vec{k}_s| = |\vec{k}_i| \quad (\text{Eq. 13-13})$$

Because these magnitudes are equal, we represent each simply by $k = 2\pi/\lambda$.

For particles that are small compared to the wavelength, the polarization of the scattered light is in the direction of the projection of the incident polarization at the particle onto a plane perpendicular to \vec{k}_s . In vector notation this is equivalent to the double cross product, $(\hat{k}_s \times \hat{x}) \times \hat{k}_s$, where \hat{k}_s is the unit vector in the scattering direction, that is, $\hat{k}_s = \vec{k}_s/|\vec{k}_s|$. Either of these methods yield the scattered intensity to obey the proportionality

$$I_{\text{sca}} \propto 1 - \cos^2 \phi \sin^2 \theta \quad (\text{Eq. 13-14})$$

Most experiments are confined to the scattering plane; hence, $\phi = 90^\circ$, as drawn in Figure 13-2. Then the polarization projects completely onto plane p of Figure 13-1 with no angular dependence. The angle θ is the scattering angle; $\theta = 0$ is forward scattering. We now consider incident light with either vertical, V , or horizontal, H , polarization. The scattered light can be detected through a polarizer set in either the V or H directions. Thus, four scattering arrangements can be obtained described by the scattered

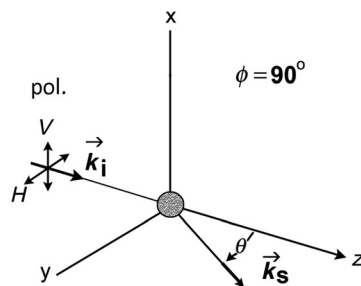


Figure 13-2 A typical scattering arrangement in which light is incident along the positive z axis with either (or both) horizontal or vertical polarization. Scattered light is detected in the horizontal, yz , scattering plane at a scattering angle of θ .

intensities as

$$I_{VV}, I_{VH}, I_{HV}, \text{ and } I_{HH}$$

where the first subscript describes the incident polarization, the second the detected polarization of the scattered light. I_{VV} is the most common scattering arrangement.

For particles that are small compared to the wavelength, these four intensities are dependent on θ in simple ways. Larger particles yield more complex functionalities but bear the imprint of these simple functionalities. The polarization rule above and the concept of projection embodied in Equation 13-14 can be used to infer the four intensities. The most common scattering arrangement measures I_{VV} , which is independent of θ , hence isotropic in the scattering plane. The projection rule or Equation 13-14 imply $I_{VH} = I_{HV} = 0$, and $I_{HH} \propto \cos^2 \theta$.

Unpolarized light is the incoherent sum of two equal components with polarization that differ in direction by 90° . To determine the polarization state of light scattered from an unpolarized incident beam one need only apply the rules above for polarized light to the two polarized components in linear combination. Figure 13-3 is an example.

13.2.2 Small Particles: Rayleigh Scattering

13.2.2.1 Introduction A small particle has all its dimensions small compared to λ , the wavelength of light. Scattering from small particles is called Rayleigh scattering. A simple dimensionality argument can be made for the length functionalities, of which there are two, in Rayleigh scattering. Since the particle is very small compared to the wavelength of light, the phase of the incident light is uniform across the volume of the particle. If one subdivides the particle into infinitesimal subvolumes, all subvolumes see the same phase. Furthermore, again since the particle is relatively small, the light scattered to the detector from all subvolumes of the particle has traveled essentially the same distance. This means that no relative phase has accumulated due to this travel. With all this, light from each subvolume of the particle has the same phase at the detector. Then, the total scattered

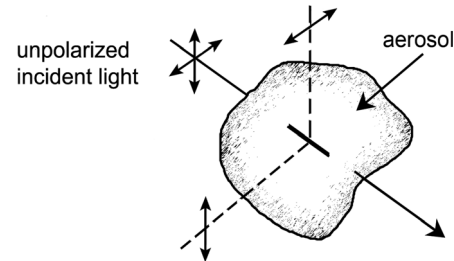


Figure 13-3 Unpolarized incident light scatters from an aerosol to yield polarized scattered light as indicated.

field at the detector is directly proportional to the number of subvolumes, which is in turn proportional to the particle volume, V_{part} . Intensity is field amplitude squared, thus

$$I \propto V_{\text{part}}^2 \quad (\text{Eq. 13-15})$$

Cross section is an effective area, hence it has units of length squared. So far in Equation 13-15 we have V_{part}^2 , which is length to the sixth power. Thus, a factor of length to the inverse fourth power is missing. There are only two length scales in the problem, particle size and optical wavelength, λ . Particle size has already been used with the V_{part}^2 . Thus, to achieve the proper units for cross section, a factor of λ^{-4} must be included to yield a cross section with the proper units. Thus,

$$C_{\text{sca}} \sim \lambda^{-4} V_{\text{part}}^2 \quad (\text{Eq. 13-16})$$

This simple derivation did not depend on particle shape; thus the result is independent of shape. Nor did it depend on scattering angle; thus the scattering is independent of scattering angle, that is, the scattering is isotropic (if we ignore possible polarization effects, see Section 13.2.1.4).

13.2.2.2 Rayleigh Differential Cross Section Electromagnetic theory can obtain an exact theoretical expression for Rayleigh scattering for the simplest case of a spherical particle of radius a . We may then define the size parameter as

$$\alpha = 2\pi a/\lambda \quad (\text{Eq. 13-17})$$

which is a dimensionless ratio of the two length scales involved. The conditions for Rayleigh scattering are

$$\alpha \ll 1 \quad (\text{Eq. 13-18})$$

$$m\alpha \ll 1 \quad (\text{Eq. 13-19})$$

Where m is the relative index of refraction of the particle

$$m = n_{\text{particle}}/n_{\text{medium}} \quad (\text{Eq. 13-20})$$

The differential scattering cross section is

$$\frac{dC_{\text{sca}}}{d\Omega} = k^4 a^6 \left| \frac{m^2 - 1}{m^2 + 2} \right|^2 \quad (\text{Eq. 13-21})$$

$$= \frac{16\pi^4 a^6}{\lambda^4} \left| \frac{m^2 - 1}{m^2 + 2} \right|^2 \quad (\text{Eq. 13-22})$$

By Equation 13-4,

$$I_{\text{VV}} = \frac{k^4 a^6}{r^2} \left| \frac{m^2 - 1}{m^2 + 2} \right|^2 I_0 \quad (\text{Eq. 13-23a})$$

If the incident light is unpolarized this expression modifies to

$$I = \frac{k^4 a^6}{2r^2} \left| \frac{m^2 - 1}{m^2 + 2} \right|^2 (1 + \cos \theta) I_0 \quad (\text{Eq. 13-23b})$$

Recall $k = 2\pi/\lambda$. Often the term involving the refractive index, the Lorentz term, is abbreviated as $F(m) = |(m^2 - 1)/(m^2 + 2)|^2$. This makes Equation 13-21 simply

$$\frac{dC_{\text{sca}}}{d\Omega} = k^4 a^6 F(m) \quad (\text{Eq. 13-24})$$

Rayleigh scattering has a number of important characteristics:

1. *Isotropy.* The I_{VV} scattering is *independent of θ* in the scattering plane. $I_{\text{VH}} = I_{\text{HV}} = 0$, and $I_{\text{HH}} = I_{\text{VV}} \cos^2 \theta$.
2. *The λ^{-4} dependence.* Blue light scatters more than red. This is associated with the blue of the sky and the red of the sunset (Minneart 1993; Pesic 2005), but other (lesser) factors are involved. In perfectly clean air (no particles) molecular scattering occurs due to small, thermodynamic fluctuations in the air density. Since the fluctuations are small compared to the wavelength, the Rayleigh λ^{-4} dependence ensues.
3. *The Tyndall effect.* The strong size dependence of $V_{\text{part}}^2 \sim a^6$ leads to an increase in scattering as a system of particles coarsens. To see this consider that the total scattering from a particulate system of Rayleigh scatterers of n particles per unit volume has the proportionality

$$I_{\text{sca}} \propto n V_{\text{part}}^2 \quad (\text{Eq. 13-25})$$

If the only growth process in the system is aggregation, the total particulate mass is conserved. Hence, nV_{part} is constant. On the other hand V_{part} increases during aggregation. Rewriting Equation 13-25 as

$$I_{\text{sca}} \propto n V_{\text{part}} \cdot V_{\text{part}} \quad (\text{Eq. 13-26})$$

shows that the scattered intensity increases proportional to V_{part} as the system aggregates. This is the Tyndall effect. Notice that there is an inverse Tyndall effect, which is to say that for a constant amount of matter, the more finely divided it becomes, the less it scatters.

13.2.2.3 Rayleigh Total Cross Section Integration of the differential cross section over the complete solid angle of 4π yields the total cross section. We consider the scattering arrangement in Figure 13-1 with incident light polarized in

the vertical direction to find

$$C_{\text{sca}} = \int \frac{dC_{\text{sca}}}{d\Omega} d\Omega \quad (\text{Eq. 13-27})$$

$$= \frac{dC_{\text{sca}}}{d\Omega} \int_0^{2\pi} \int_{-1}^1 (1 - \cos^2 \varphi \sin^2 \theta) d(\cos \theta) d\varphi \quad (\text{Eq. 13-28})$$

$$= \frac{8\pi}{3} \frac{dC_{\text{sca}}}{d\Omega} \quad (\text{Eq. 13-29})$$

Since the differential cross section is independent of angle, we see that the factor $8\pi/3$ comes from integration of the polarization. Equations 13-21 and 13-29 yield

$$C_{\text{sca}} = \frac{8\pi}{3} k^4 a^6 F(m) \quad (\text{Eq. 13-30})$$

Thus, the scattering efficiency, $Q = C_{\text{sca}}/\pi a^2$ is

$$Q_{\text{sca}} = \frac{8}{3} \alpha^4 F(m) \quad (\text{Eq. 13-31})$$

For Rayleigh scattering the size parameter $\alpha \ll 1$, thus Equation 13-31 implies that Rayleigh scatterers are not very efficient; that is, they scatter a lot less than the geometric cross section would imply.

13.2.2.4 Rayleigh Absorption Cross Section The Rayleigh absorption cross section is

$$C_{\text{abs}} = \frac{8\pi^2 a^3}{\lambda} \text{Im} \left(\frac{m^2 - 1}{m^2 + 2} \right) \quad (\text{Eq. 13-32})$$

where Im means imaginary part. We use the notation $m = n + i\kappa$ and $\text{Im}[(m^2 - 1)/(m^2 + 2)] = E(m)$. The absorption efficiency is simply

$$Q_{\text{abs}} = 4\alpha E(m) \quad (\text{Eq. 13-33})$$

As for scattering, a simple dimensionality argument can be made for the absorption cross section. Since the particle is very small, the wave completely penetrates the volume of the particle. Hence, all subvolumes of the particle absorb equally to imply $C_{\text{abs}} \propto V_{\text{part}}$. To make the units match we divide by the only other length scale of the system, the wavelength, to yield $C_{\text{abs}} \propto \lambda^{-1} V_{\text{part}}$. This is significantly different than scattering.

13.2.2.5 Rayleigh Extinction Cross Section Extinction is the sum of scattering plus absorption. If the particle's refractive index is purely real, there is no absorption, so extinction equals scattering. If there is an imaginary part to the particle's refractive index, the absorption will usually

dominate the scattering in the Rayleigh regime where the size parameter α is small because scattering has an extra factor of α^3 (compare Eqs. 13-30 and 13-32), which is much less than unity for a Rayleigh particle.

These facts open the possibility for light-scattering measurement of the particle size and number density for small particles. The scattered intensity at an arbitrary angle is proportional to the differential cross section and the number density of particles, n . Thus, from Equation 13-24, $I_{\text{sca}} \sim na^6 F(m)$.

Such a measurement is usually made by calibrating against a known scatterer such as a gas or liquid with known Rayleigh ratio. A simultaneous turbidity measurement can be made using Equation 13-9. The turbidity is related via Equation 13-10 to the number density and the extinction cross section which, in this limit, equals the absorption cross section. Then use of Equation 13-32 implies $\tau \sim na^3 E(m)$. We now have two equations and two unknowns, n and a , which can be determined.

13.2.3 “Soft” Particles: Rayleigh-Debye-Gans Scattering

If the refractive index contrast between the scattering particle and the medium is small, that is, if m is very nearly unity, then the interesting case of Rayleigh-Debye-Gans scattering can occur. The conditions for Rayleigh-Debye-Gans scattering are

$$|m - 1| \ll 1 \quad (\text{Eq. 13-34a})$$

$$\rho = 2\alpha|m - 1| \ll 1 \quad (\text{Eq. 13-34b})$$

Note that Equations 13-34a,b allow for particles of arbitrary size so long as they are “soft,” $m \rightarrow 1$. The parameter ρ in Equation 13-34b is called the *phase shift parameter* and represents the difference in phase between a wave that travels through a particle directly across its diameter and one that travels the same distance through the medium.

We remark that for X-rays the refractive index is near unity, hence the Rayleigh-Debye-Gans limit holds for such radiation. Indeed, much of what follows was developed to understand and describe small-angle X-ray scattering (SAXS) and small angle neutron scattering (SANS). Here we use this significant lineage as the basis for understanding scattering of light from particles of arbitrary refractive index.

For a sphere of radius a the Rayleigh-Debye-Gans differential scattering cross section in the scattering plane for vertically polarized light (Fig. 13-2) is

$$\frac{dC_{\text{sca}}}{d\Omega_{\text{RDG}}} = \frac{dC_{\text{sca}}}{d\Omega_{\text{R}}} \left[\frac{3}{u^3} (\sin u - u \cos u) \right]^2 \quad (\text{Eq. 13-35})$$

where

$$u = 2\alpha \sin(\theta/2) \quad (\text{Eq. 13-36})$$

or

$$u = qa \quad (\text{Eq. 13-37})$$

In Equation 13-35 the subscripts RDG and R denote Rayleigh-Debye-Gans and Rayleigh, respectively. In Equation 13-37, q is the **scattering wave vector** given by

$$q = (4\pi/\lambda) \sin(\theta/2) \quad (\text{Eq. 13-38})$$

The scattering wave vector, q , is a very important variable with a lineage to SAXS and SANS. The unit of q is inverse length; hence it can be shown that q^{-1} is the length scale of the scattering experiment. This means that when the experimenter adjusts the scattering angle to determine a q , the scattering is sensing length scales of q^{-1} in the scattering system. Application of this concept to scattering for a particle of any extent a implies that if q varies but qa remains less than unity, there will be no dependence on q , that is, no scattering angle dependence. This condition is when the scattering length scale $q^{-1} > a$ so it cannot resolve the object. This is the isotropic forward-scattering regime for any size particle. Only when $q^{-1} < a$ will the scattering resolve the object and then the scattered intensity show a q , hence an angular, dependence. Moreover, the functionality starts near $qa \simeq 1$, and this fact can be used to determine the size of the particle.

Rayleigh-Debye-Gans scattering is the diffraction limit of scattering; the electromagnetic nature is suppressed by the use of $m \rightarrow 1$. The term inside the brackets of Equation 13-35 is the Fourier transform of a sphere; hence it represents diffraction from a sphere. It is completely analogous to single-slit Fraunhofer diffraction of sophomore physics fame. Thus RDG is simply the Fourier transform of a sphere, squared. In quantum mechanics the analogue is the first Born approximation for weakly scattering potentials.

Rayleigh-Debye-Gans scattering is not limited to spheres. The scattering for an arbitrary shaped particle is, in analogy to Equation 13-35, the square of the Fourier transform of the shape times the Rayleigh scattering cross section.

A plot of RDG scattering is shown in Figure 13-4, double log versus qa . This figure shows that for $qa < 1$ the scattered intensity is constant with q , hence constant with scattering angle. This is called the “forward-scattering lobe.” The forward-scattering lobe starts near $qa = 1$, which corresponds to $\theta = \lambda/2\pi a$ for a small angle (i.e., $\sin \theta/2 \simeq \theta/2$). In this region the scattering magnitude is equal to the Rayleigh result, Equation 13-21. Interference ripples are seen for $qa > 1$ with spacing $\Delta u = \pi$, which corresponds to $\Delta q = \pi/a$ and $\Delta \theta = \lambda/2a$ and small θ ; recall single-slit diffraction. The envelope of this regime has a slope of -4 to imply the power law $(qa)^{-4}$. This is the so-called Porod regime. In fact, the -4 is equal to $-(d+1)$ where d is the dimensionality of the sphere, which is $d = 3$. These are all valuable observations for they persist, to some degree, in the general case for scattering from an arbitrary object.

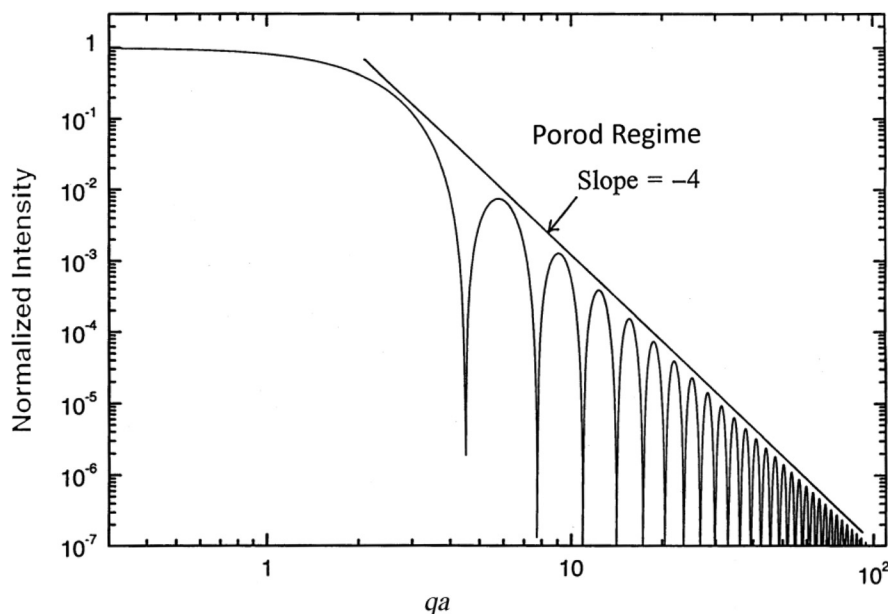


Figure 13-4 Normalized Rayleigh-Debye-Gans scattered intensity versus the dimensionless $u = qa$.

EXAMPLE 13-1

While walking at night you observe the moon through a thin cloud surrounded by a luminous disk of scattering from the cloud. The luminous disk has four times the apparent diameter of the moon. Estimate the radius of the water droplets in the cloud.

Answer: From Figure 13-4 we see that the forward-scattering lobe begins to fall off when $qa \approx 1$. From Equation 13-38 we find

$$qa = (4\pi a/\lambda) \sin(\theta/2) \approx 2\pi a\theta/\lambda \approx 1$$

$$a \approx \lambda/2\pi\theta$$

Since the angular size of the moon is $0.5^\circ \approx 0.5/60 = 1/120$ radian, the angular size of the forward lobe is $\theta = 4/120 = 1/30$ radian. We take $\lambda \approx 0.5 \mu\text{m}$ for white light and find

$$a \approx 0.5 \mu\text{m}/2\pi(1/30) \approx 2.5 \mu\text{m}$$

13.2.4 Spheres of Arbitrary Size and Refractive Index: The Mie Theory

The Rayleigh and Rayleigh-Debye-Gans theories of scattering and absorption represent solutions to Maxwell's equations in which approximations have been made due to small size and small index of refraction. For an arbitrary particle Maxwell's equations must be solved exactly. Mie first presented these solutions for the simplest case of a homogeneous sphere and the term *Mie scattering* is often applied to this case. The equations are, however, not particularly simple to use or to gain physical insight. Below we follow the lesson learned from RDG scattering and use the scattering wave

vector q as the independent variable (even better the dimensionless qa) for plotting the Mie scattering differential cross section. Then physical patterns appear (Sorensen and Fischbach 2000; Sorensen and Shi 2000, 2002; Berg et al. 2005), which lend a great deal of order to the description of scattering by an arbitrary sphere.

13.2.4.1 The Mie Differential Cross Section Figure 13-5a shows an example of Mie scattering, I_{VV} , for a sphere with an index of refraction $m = 1.50$ and a variety of sizes expressed as the size parameter α . The normalized intensity $I(\theta)/I(0)$ versus θ is plotted. A series of bumps and wiggles are seen with some periodicities, but with no particularly coherent pattern. The scattering angle θ , although conveniently measured in the laboratory, is not the best parameter for plotting the scattered intensity. Figure 13-5b shows the same intensity plotted versus the dimensionless product qa . Now the data fall into patterns described by power laws.

Figure 13-5b shows that at small qa a nearly universal "forward-scattering lobe" is seen. Near $qa \sim 1$, the falloff is approximately described by the Guinier equation, $I(q)/I(0) \sim 1 - q^2 a^2/5$ (see below). The enhanced backscattering, the "glory," visible in plots with $m = 1.50$, shows no particular pattern but is compressed into spikes at $2ka$ in the large qa part for each size parameter α . The key features are the envelopes of these plots with slopes -2 and -4 . Figure 13-5b includes lines that roughly describe these envelopes.

Figure 13-6a shows the Rayleigh-normalized Mie scattering intensity, that is, I_{VV} divided by the differential Rayleigh cross section, Equation 13-21. The calculations have been averaged over a small but finite size distribution to eliminate the ripples. Many of the features described above are contained in this figure. One sees a pattern of power laws with slope 0, -2 , and -4 . An important feature

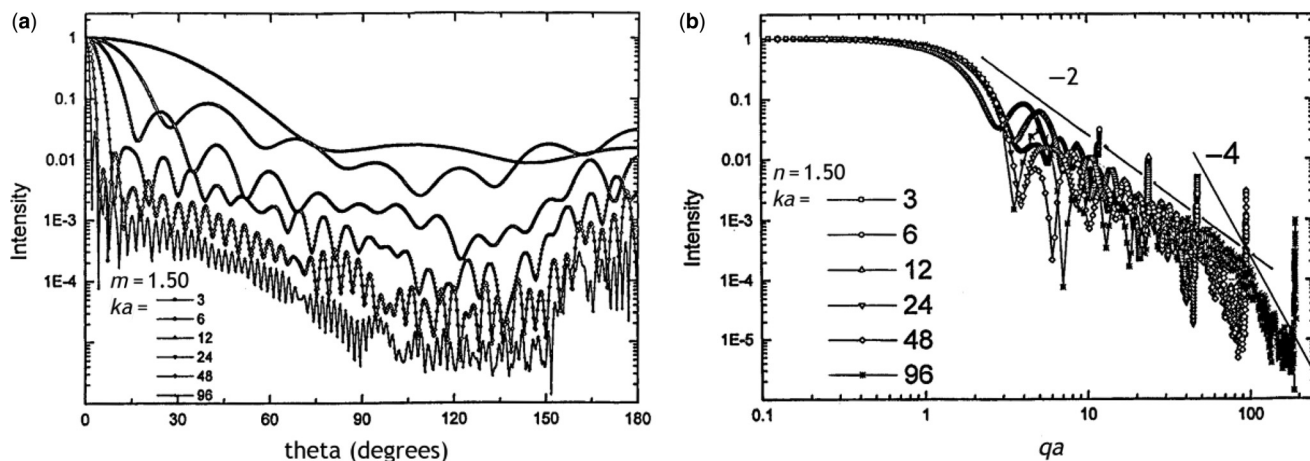


Figure 13-5 (a) Normalized Mie scattering curves as a function of scattering angle for spheres of refractive index, $m = 1.50$, and a variety of size parameters $\alpha = ka$; (b) same as (a) but plotted versus qa . Lines with slopes -2 and -4 are shown.

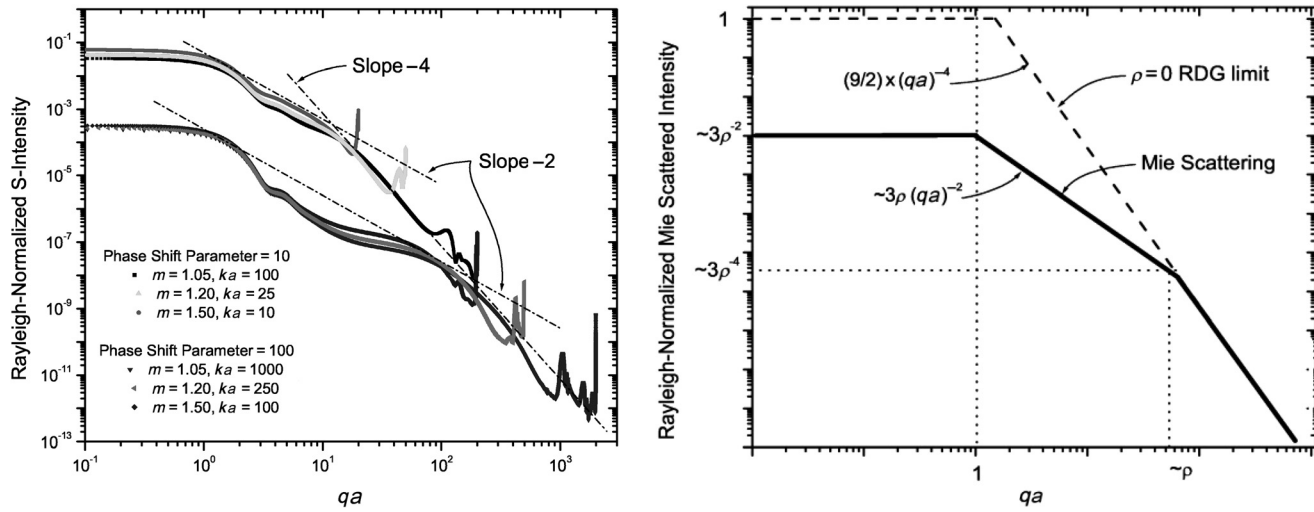


Figure 13-6 (a) Shown are two sets of Rayleigh-normalized Mie intensity curves. The three curves in each set have the same value of ρ but different values of the size parameter $\alpha = ka$ and refractive index m . The bounding envelopes are shown for both sets of curves and illustrate how the envelopes only depend on $\rho = 2ka|m - 1|$. (b) Diagram of the averaged Rayleigh-normalized Mie scattering patterns for uniform dielectric spheres of arbitrary size and real refractive index parameterized by ρ , thick solid line. In this example $\rho \approx 55$. The dashed line is the RDG limit, $\rho \rightarrow 0$.

is that Figure 13-6a demonstrates a quasi-universality of Mie scattering on the phase-shift parameter ρ (Eq. 13-34b). For each phase-shift parameter value shown, the values of m and $\alpha = ka$ vary widely. Despite this variation, the curves for the same ρ lie with each other, hence the curves are universal with ρ . This universality is not perfect, however, with variations of approximately a factor of 3 for the same ρ . Hence we use the term “quasi-universal” to describe the ρ functionality.

Figure 13-6b gives a general description of light scattering by a sphere of arbitrary size and real refractive index, Mie scattering. The Mie scattering patterns start at $\rho = 0$ with the RDG limit. For $qa < 1$ the RDG curve is flat, that is, $(qa)^0$ and equivalent to Rayleigh scattering. For $qa > 1$ it falls off with a negative four power law, the Porod limit, with magnitude $(9/2)(qa)^{-4}$ times the Rayleigh scattering cross section. This includes Rayleigh scattering in the limit $\lambda \gg a$ because then $qa \ll 1$ and only the flat part of the scattering function is obtained.

When $\rho > 1$, scattering in the Rayleigh regime decreases relative to true Rayleigh scattering. The relative decrease (remember, the unnormalized scattering increases with ρ) is proportional to ρ^2 as depicted in Figure 13-6b. For $qa > 1$ the scattering now falls off approximately as $(qa)^{-2}$ until this functionality crosses the RDG curve at $qa \simeq \rho$. For $qa > \rho$ the scattering is the same as RDG scattering, falling off as $(qa)^{-4}$ for all a and m as long as $qa > \rho$. The $(qa)^{-2}$ functionality between $qa = 1$ and ρ for $\rho > 1$ is exact only at those limits. The average Mie curves dip below the $(qa)^{-2}$ line. This dip is the first interference minimum near $qa \approx 3.5$ present in all Mie curves and is the strongest of all the minima.

In summary, if we ignore the ripples and the glory, Mie scattering displays three approximate power law regimes

$$I \propto (qa)^0 \quad \text{when } qa < 1 \quad (\text{Eq. 13-39a})$$

$$\propto (qa)^{-2} \quad \text{when } 1 < qa < \rho \quad (\text{Eq. 13-39b})$$

$$\propto (qa)^{-4} \quad \text{when } qa > \rho \quad (\text{Eq. 13-39c})$$

13.2.4.2 The Mie Guinier Regime The end of the isotropic forward scattering lobe, near $qa \sim 1$, in both the RGD and Mie scattering regimes, is called the Guinier regime. This regime is very important because it provides a simple and convenient way to size particles with little or no need to know the refractive index. This is also the region of crossover between the functionalities of Equations 13-39a, b. For $\rho \rightarrow 0$ it is described by

$$I(q) = I(0) \left(1 - \frac{1}{3} q^2 R_g^2 \right) \quad (\text{Eq. 13-40})$$

In Equation 13-40 R_g is the radius of gyration of the scattering object, which can have any shape. If spherical, $R_g = \sqrt{3/5} a$. We have found (Sorensen and Shi 2002) for spheres that Equation 13-40 must be modified when $\rho > 1$

$$I(q) \sim \left(1 - \frac{1}{3} q^2 R_{g,G}^2 \right) \quad (\text{Eq. 13-41})$$

In Equation 13-41 is $R_{g,G}$, which we call the “Guinier regime determined radius of gyration”. When $\rho = 0$ $R_{g,G} = R_g$.

Otherwise, the ratio $R_{g,G}/R_g$ follows a quasi-universal, oscillatory behavior with ρ described by Sorensen and Shi (2000), which has the limit as $\rho \rightarrow \infty$ $R_{g,G} = 1.12R_g$, the Fraunhofer diffraction limit. The important point is that use of a Guinier analysis with Equation 13-41 allows for a simple yet accurate experimental measurement of the particle R_g .

13.2.4.3 The Mie Ripples Recognize that the ripple structure that we have ignored above by considering only the envelopes will in an experiment be washed out by any modest particle size polydispersity of geometric width of 20% or more (Rieker et al. 1999). However, the ripple structure contains useful information. Let the symbol Δu designate the spacing between consecutive ripples when the intensity is plotted versus $u = qa$, and $\Delta\theta$ when plotted versus θ . Then (Sorensen and Shi 2000)

$$\Delta u = \pi \quad \text{for } \rho \lesssim 5 \quad (\text{Eq. 13-42a})$$

$$\Delta u = \pi \cos \theta \quad \text{for } \rho \gtrsim 5 \quad (\text{Eq. 13-42b})$$

Equation 13-42b is equivalent to

$$\Delta\theta = \pi/\alpha = \lambda/2a \quad \text{for } \rho \gtrsim 5 \quad (\text{Eq. 13-42c})$$

Equation 13-42c is identical to the angular fringe spacing for Fraunhofer diffraction from a single slit of width $2a$. Equation 13-42c suggests that for highly monodisperse systems, which would yield good ripple visibility, a measurement of the ripple spacing would yield the particle size (Maron and Elder 1963; Pierce and Maron 1964; Kerker et al. 1964).

13.2.4.4 The Mie Total Cross Section Figure 13-7 shows C_{sca} as a function of the size parameter $\alpha = ka = 2\pi a/\lambda$ for spheres with different refractive indices m . Curves of different m in the $ka < 1$ range show a clear m dependence, which is explained by the m functionality in Equation 13-21. As the size a grows to values for which $\rho > 3$, the a^6 dependence crosses over, through a ripple structure, to a geometric a^2 (i.e., the geometrical cross section of the sphere) dependence at large ρ , large ka . The separation between curves of different m in the Rayleigh regime begins to vanish. As a continues to increase, all curves converge onto a value of twice the geometrical cross section of the sphere, $2\pi a^2$, with no m dependence and the ripple structure decays away. This is a remarkable transformation from an optical entity dependent on the refractive index m , to an apparently “nonoptical” entity with no m dependence. Moreover, the remaining functionality is remarkable too for

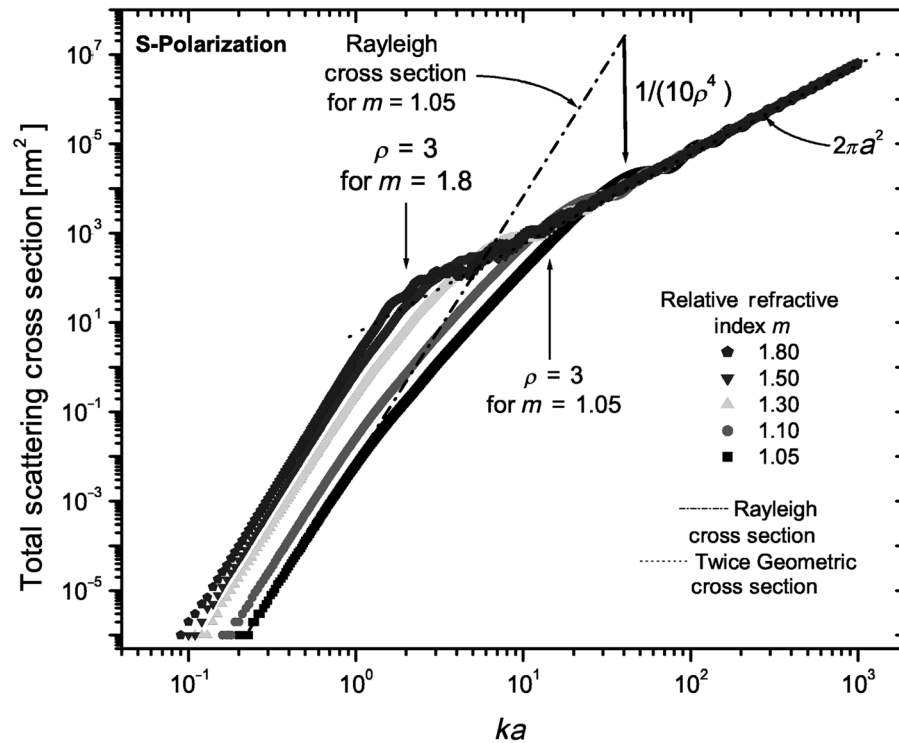


Figure 13-7 The total Mie cross section C_{sca} versus the size parameter $\alpha = ka = 2\pi a/\lambda$ for various m and incident light with V-polarization and $\lambda = 200\pi$ nm. The large ρ behavior of $C_{\text{sca}} \approx 2\pi a^2$ is shown as the dotted curve; the Rayleigh cross section is shown as the dot dashed line for $m = 1.05$. The vertical arrow shows the factor $1/(c^2\rho^4)$, where $c \approx \sqrt{10}$, relating the Rayleigh and Mie cross section for $m = 1.05$, in the $\rho > 1$ range. For clarity, the legend shows the data sets in the same order as they appear in the figure.

it claims that in the geometric limit the scattering cross section is twice the geometric cross section. How is it that the scattering from a large object, a rugby ball for example, is twice its shadow? This fact is known as the Extinction Paradox and has seen a number of explanations, the best of which is given by Berg et al. (2008a,b).

EXAMPLE 13-2

Estimate the total scattering cross section for a spherical water droplet with a diameter of $3.0\ \mu\text{m}$ and index of refraction of 1.33. The wavelength of the light is $0.488\ \mu\text{m}$.

Answer: The ρ value for these particles is

$$\rho = 4\pi(3.0\ \mu\text{m}/2)(1.33 - 1)/(0.488\ \mu\text{m}) = 12.7$$

This is large to imply the total cross section is about equal to

$$C_{\text{sca}} = 2\pi a^2 = 6.28(1.5 \times 10^{-4}\ \text{cm})^2 = 14 \times 10^{-8}\ \text{cm}^2$$

13.2.5 Rayleigh-Debye-Gans Fractal Aggregate Scattering

13.2.5.1 Fractal Aggregates The past 25 years have seen the development of the fractal concept for quantitative description of many aggregates that form in nature (Forrest and Witten 1979; Mandelbrot 1983; Jullien and Botet 1987). A fractal is an object that displays scale invariant symmetry; that is, it looks the same when viewed at different scales. Any real fractal object will have this scale invariance over only a finite range of scales. A consequence of this scale invariance is that the linear size scales with the mass with a power law; the exponent of this is called the fractal dimension, D . For an aggregate with an indefinite border the linear size can be well described by its radius of gyration, R_g . Then a fractal aggregate of N monomers or primary particles obeys

$$N = k_0(R_g/a)^D \quad (\text{Eq. 13-43})$$

In Equation 13-43 k_0 is a prefactor of order unity and a is the primary particle radius. Perhaps the most common aggregation process is diffusion-limited cluster aggregation (DLCA), which yields clusters for which $D = 1.75$ to 1.80 . With experimentation on soot aggregates we have found $k_0 = 1.23 \pm 0.07$ (Cai et al. 1995) and 1.66 ± 0.4 (Sorensen and Feke 1996). Some other workers have found larger values on the order of 2.4 for soot (Koylu and Faeth 1994a,b). With simulations, we have found $k_0 = 1.19 \pm 0.1$ (Sorensen and Roberts 1997) and 1.30 ± 0.07 (Oh and Sorensen 1997). Simulations of DLCA by Lattuada et al. (2003) found $D = 1.82$ and $k_0 = 1.19$.

13.2.5.2 Scattering and Absorption by Fractal Aggregates The scattering and absorption by fractal aggregates under the Rayleigh-Debye-Gans approximation, so-called RDGFA theory, is now fairly well known (Sorensen 2001). The Rayleigh-Debye-Gans approximation assumes that the effects of intracluster multiple scattering can be neglected. This assumption has been shown to be pretty good for $D < 2$. It is more suspect for $D > 2$ because such clusters are not “geometrically transparent”; that is, their projection onto a two-dimensional (2d) plane would fill the plane. Other factors that can lead to multiple scattering effects are large monomer a (or, better, its size parameter α), N , and m . Based on an analysis by Farias et al. (1996) and our own experimental tests (Wang and Sorensen 2002), we have concluded (Sorensen 2001) that a phase-shift parameter for the cluster aggregate, ρ^c , can be defined as

$$\rho^c = 2kR_g|m - 1| \quad (\text{Eq. 13-44})$$

When this is less than ≈ 3 , RDGFA is valid. An argument can be made that for $D < 2$, the RDGFA gets better with larger N . The matter is not yet settled, and this is an area of research interest.

Under RDGFA the scattering and absorption cross sections for a fractal aggregate of N monomers with radius a are simply related to the monomer cross sections as follows (Sorensen 2001).

$$C_{\text{abs}}^c = NC_{\text{abs}}^m \quad (\text{Eq. 13-45})$$

$$\frac{dC_{\text{sca}}}{d\Omega} = N^2 \frac{dC_{\text{sca}}^m}{d\Omega} S(q) \quad (\text{Eq. 13-46})$$

The superscripts c and m designate cluster and monomer, respectively. $S(q)$ is the static structure factor of the cluster, which is the Fourier transform of the cluster density function, squared, and hence it contains information regarding the cluster structure. The structure factor, see below, has the asymptotic forms $S(0) = 1$ and $S(q) \sim q^{-D}$ for $q \gg R_g^{-1}$.

The simple forms of Equations 13-45 and 13-46 have physical interpretation. Equation 13-45 implies that the absorption is independent of the state of aggregation; the monomers absorb independently. Equation 13-46 implies that at small q the scattering from N monomers is also independent of the state of aggregation; the N scattered fields add constructively to yield the N^2 dependence.

There are some variants on the form of the structure factor (Sorensen 2001). The best description is simply

$$S(q) = 1, \quad qR_g < 1 \quad (\text{Eq. 13-47a})$$

$$= (1 - q^2 R_g^2/3)^{-1} \quad qR_g \sim 1 \quad (\text{Eq. 13-47b})$$

$$= C(qR_g)^{-D} \quad qR_g > 5 \quad (\text{Eq. 13-47c})$$

where the coefficient $C = 1.0 \pm 0.1$.

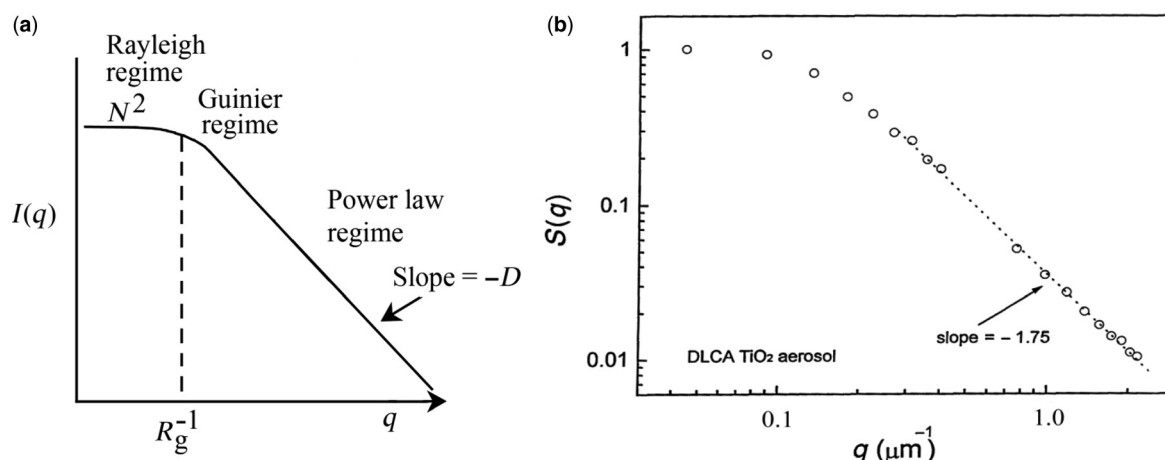


Figure 13-8 (a) Schematic of the general behavior of the structure factor for a single fractal aggregate of N primary particles with aggregate fractal dimension D , radius of gyration R_g , and monomer radius a . (b) Light-scattering structure factor obtained from a titania aerosol.

The general behavior of $I(q)$ is shown in Figure 13-8a. It has many features in common with the descriptions of non-cluster scattering above. At small q there is a scattering angle-independent forward-scattering lobe, the Rayleigh regime, where the cross section is N^2 times the monomer Rayleigh cross section (recall Eq. 13-15). Next follows a Guinier regime near $qR_g \sim 1$. This can be used to measure R_g . At yet larger q lies a power law regime, where $S(q) \sim q^{-D}$. This can be used to measure D . Finally, at very large q often inaccessible for light scattering but often observed with SAXS is the regime for which $q > a^{-1}$ (not drawn), where a is the length scale of the primary particles. In this regime the so-called form factor of the primaries would be seen. This is essentially the scattering from single dense particles, for example, Mie scattering, described above. Figure 13-8b shows an example of scattering from a titania aerosol.

EXAMPLE 13-3

For the aerosol in Figure 13-8b, (a) what is the approximate mean size of the aggregates? (b) What is the mean fractal dimension of the aggregates?

Answer: Comparing Figure 13-8a to Figure 13-8b we see that the Guinier regime is near $0.1 \mu\text{m}^{-1}$. This equals R_g^{-1} , so $R_g = 10 \mu\text{m}$.

Comparing Figure 13-8a to Figure 13-8b we see that the power law regime has a slope of -1.75 ; thus $D_f = 1.75$.

scattering here and then there before they reach the detector. If the light scatters from any of the particles in an aerosol only once, then the total scattering from the ensemble is easily interpreted as an average of single-scattering events. However, there is always a finite chance that the scattered light reaching the detector has scattered sequentially from more than one particle. This is multiple scattering.

Under the assumption that the photons act like classical particles and that their scattering is a Gaussian random process described by the Poisson distribution, one can show that the extinction of the light through a medium containing nonabsorbing particles obeys the classic Lambert-Beer law, Equation 13-9 (Mokhtari et al. 2005). Moreover, the turbidity is the inverse of the photon mean free path l between scattering events, viz.

$$l = \tau^{-1} = (C_{\text{sca}} n)^{-1} \quad (\text{Eq. 13-48})$$

The average number of scattering events for the photons $\langle s \rangle$ is the ratio of the photon mean free path to the length of the scattering volume

$$\langle s \rangle = x/l \quad (\text{Eq. 13-49})$$

Then the probability for s scattering events for a given photon is given by the Poisson distribution as

$$P(s) = \exp(-\langle s \rangle) \frac{\langle s \rangle^s}{s!} \quad (\text{Eq. 13-50})$$

Thus small $\langle s \rangle$ implies that the probability of more than one scattering event, that is, multiple scattering, is small. Fortunately the value of $\langle s \rangle$ is simply obtained either by calculation with Equation 13-48 or measurement. Measurement

13.2.6 Multiple Scattering

Multiple scattering is most easily envisioned with the photon concept of light. One can think of these little “bullets” as first

is particularly simple because $\langle s \rangle = x\tau$ by Equations 13-48 and 13-49, and τ is easily measured via Equation 13-9.

A common strategy to avoid multiple scattering is simply to dilute the sample. Sometimes this cannot be done without changing the system. Another strategy is to make the scattering length x smaller than the photon mean free path. This can be done by reducing the sample size. Then, by Equation 13-49, the average number of scattering events $\langle s \rangle$ can be made far less than one.

13.2.7 Scattering from Ensembles of Particles

For particles situated randomly in an aerosol, the most common situation, the total scattered intensity is simply the sum of the scattered intensities from each particle in the illuminated scattering volume. Most often the ensemble of particles is polydisperse with a size distribution $n(a)$ numbers per unit volume. Then the total scattering from the ensemble is

$$I(q) = \int I(a, q) n(a) da \quad (\text{Eq. 13-51})$$

An important aspect of light scattering is that big particles scatter more than smaller ones. Thus the total scattering is weighted in favor of the bigger particles in the distribution. This can be quite extreme in the Rayleigh regime where the scattering goes as a^6 . For example, if the distribution was bi-disperse with equal amounts of 40- and 80-nm particles, the 80-nm particles would scatter 64 times more light and hence dominate the scattering; the smaller ones would effectively not be seen.

Guinier analysis will yield a mean size of the particle distribution weighted by the scattering. This weighting can be complex in size regimes where the scattered intensity is a complex function of the size. In the small size, Rayleigh or RDG regimes, however, the functionality is simple, *viz.* $I \sim a^6$. Then Equation 13-51 is simple to calculate. A common approach is to define a z-average radius of gyration and write the Guinier equation as

$$I(q) = I(0)(1 - q^2 R_{g,z}^2/3) \quad (\text{Eq. 13-52})$$

This is particularly useful for scattering from aggregates of N primary particles where the RDG approximation leads to

$$R_{g,z}^2 = \int R_g^2(N) N^2 n(N) dN / \int n(N) dN \quad (\text{Eq. 13.53})$$

where $n(N)$ is the number of aggregates of size N per unit volume, that is, the aggregate size distribution.

The Guinier equation, Equation 13-52, implies that a graph of the inverse $I(0)/I(q)$ versus q^2 should be linear with a slope of $R_{g,z}$. This plot is similar to the Zimm plot of biophysics (Zimm 1948; Tanford 1961; Kerker 1969).

13.2.8 Nonspherical Particles

The problem of how an arbitrarily shaped particle scatters light is quite difficult but major advances have been made in the past two decades. One tack is to divide the particle up into a great many subvolumes that act as dipoles but interact with each other through their scattered fields. An iterative solution for the total scattering can be calculated numerically. This method is called the dipole-dipole approximation (DDA; Draine 1988; Draine and Flatau 1994). Another successful tack is the T-matrix formalism, which is also quite complex (Mackowski 1991, 1994; Mackowski and Mishchenko 1996). Both these methods are beyond the scope of this review.

There is some indication that the patterns in Mie scattering for spheres, discussed above and portrayed in Equations 13-39, persist for dense, irregular particles (Hubbard et al. 2008). Certainly, there is a Guinier regime that can yield semiquantitative size information.

13.3 DYNAMIC LIGHT SCATTERING

Dynamic light scattering (DLS), also known as quasi-elastic light scattering (QELS), photon correlation spectroscopy (PCS), and light-beating spectroscopy, is a technique that relies upon temporal fluctuations in the light scattered from an ensemble of particles to determine their motion. Usually the motion is random Brownian diffusion, which is quantified by a size-dependent diffusion coefficient. The DLS method measures the decay of the temporal fluctuations in the scattered light, which is related to particle diffusion; this, in turn, is related to particle size. Thus a size measurement can be made. Application of DLS to aerosols dates back to Hinds and Reist (1972); application to combustion aerosols dates back to King et al. (1982) and Flower (1983). The treatment here will give the salient highlights of DLS; those desiring a more extensive treatment are referred to Berne and Pecora (1976) and Dahneke (1983).

Dynamic light scattering yields an effective mobility size (radius) through the measurement of the particle's diffusion constant. Mobility is related to size and shape but also to the conditions of the particle's environment; hence DLS is less direct to the particle size and shape than static light scattering. On the other hand, DLS can yield size information for particle radii below ≈ 50 nm, where static methods fail due to a lack of asymmetry in the angular scattering patterns.

13.3.1 DLS Experimentation

DLS requires a coherent light source. The advent of the laser, as such a source, enabled the technique to be developed in the 1960s. Most common laboratory lasers such as HeNe, argon ion, and Nd:YAG, have enough coherence to be useful for DLS.

The second thing needed for DLS experimentation is a correlator. Correlators, which are available commercially (*MAL*, *BEC*, *BRK*, *WYA*),² calculate the temporal intensity-intensity correlation function of the scattered light. The light will be fluctuating if the particles from which it scatters are moving, and if the motion contains a random Brownian component, which it almost always will, the fluctuations are random. The intensity-intensity correlation function, which can quantify these fluctuations, is written as

$$g^{(2)}(t) = \langle I(\tau + t)I^*(\tau) \rangle \\ = B + A \exp(-2Dq^2t) \quad (\text{Eq. 13-54})$$

In Equation 13-54 the star means complex conjugate and the brackets $\langle \dots \rangle$ mean an ensemble or time average (assuming ergodicity), and we have made the reasonable assumption that the average only depends on the time difference, t (an assumption known as “stationarity”).

The “experimental” part of Equation 13-54 is the far right-hand side. A is the signal strength and B is the background. The size information is contained in the diffusion coefficient D . It is given by the Cunningham-corrected Stokes-Einstein relation

$$D = (kT/6\pi\eta a)Cc(Kn) \quad (\text{Eq. 13-55})$$

where k is Boltzmann’s constant, T is the absolute temperature, η is the suspending medium’s shear viscosity, and a is the particle’s radius, assumed spherical. $Cc(Kn)$ is the Cunningham factor, which is a function of the Knudsen number Kn .

The correlation function decays exponentially with a characteristic time called the correlation time, the primary parameter of DLS measurement. From Equation 13-54, it follows that the correlation time is given by

$$\tau_c = 1/2Dq^2 \quad (\text{Eq. 13-56})$$

It is worth noting the q^2 dependence. This can be used to adjust the correlation time into an easily measured regime. It is also a good consistency check; any experiment should show this q^2 dependence or else something is wrong.

²Refer to Appendix I for complete manufacturers’ addresses indexed to three-letter codes.

EXAMPLE 13-4

Consider 1.0- μm diameter particles in air at STP. The viscosity of air is 180 micropoise. What correlation time would you expect using an Ar^+ laser operating at 514.5 nm with a scattering angle of 90° ?

Answer: Use cgs units.

$$\begin{aligned} D &= (1.38 \times 10^{-16} \text{ erg/K}) 273 \text{ K} / 6(3.14) \\ &\quad \times (1.8 \times 10^{-4} \text{ g/cm} \cdot \text{sec})(5 \times 10^{-5} \text{ cm}) \\ &= 2.22 \times 10^{-7} \text{ cm}^2/\text{sec} \\ q &= [4(3.14)/5.15 \times 10^{-5} \text{ cm}] \sin(45) \\ &= 1.72 \times 10^5 \text{ cm}^{-1} \\ q^2 &= 2.97 \times 10^{10} \text{ cm}^{-2} \\ \tau_c &= 1/2Dq^2 = 1/2(2.22 \times 10^{-7} \text{ cm}^2/\text{sec})(2.97 \times 10^{10} \text{ cm}^{-2}) \\ &= 7.6 \times 10^{-5} \text{ s} \end{aligned}$$

As coherence declines, the signal to noise, A/B , declines. Coherence is a complex topic and will not be discussed here. Standard texts such as Hecht (1987) or Born and Wolf (1975) can be consulted. Here it is useful to know that both longitudinal coherence, related to the spectral bandwidth of the light, and transverse coherence are necessary. The former is fixed by the laser used and is typically pretty good. The latter is also a strong function of the laser but can be improved by spatial filtering transverse to the direction of the beam. Thus good transverse coherence can be gained if the laser is operating in the TEM₀₀ mode. This mode is characterized by a Gaussian beam profile. The donut profile TEM₀₁* will work too but with some loss of signal to noise.

Once the light is scattered by the medium, the experimenter has considerable control of transverse coherence and is encouraged to improve it. The concept is based on the van Cittert-Zernike theorem (Born and Wolf 1975), which states that transverse coherence of light from an incoherent source has an angular size of approximately $\theta \sim \lambda/d$ where λ is the light wavelength and d is the spatial extent of the source. This is the diffraction angle. For DLS this means we want a scattering source and an illuminated scattering volume, which is small so that θ is large enough to cover our detector’s photosensitive area at some reasonable distance. Notice it also implies we want a small detector.

As an example, suppose we have a photomultiplier tube with a 2.5-mm diameter cathode. Let’s place it 500 mm away from the scattering volume. Then it subtends an angle of $\theta_{\text{det}} \sim 2.5/500 = 5 \text{ mrad}$. If we use an unfocused laser beam with diameter of 1 mm, then according to van

Cittert-Zernike, the coherence angle is $\theta_{\text{coh}} \sim 0.5 \mu/1 \text{ mm} = 0.5 \text{ mrad}$. This is much smaller than the angular size of the detector so the signal to noise will be poor. If, however, we focus our incident beam to a diameter of 0.1 mm then $\theta_{\text{coh}} \sim 5 \text{ mrad}$ and good signal to noise will be achieved. Note this simple example considered diffraction in only the vertical direction, since the horizontally propagating beam was restricted by its diameter in the vertical direction. Horizontal is at work too, so we would want to spatially filter, that is, block, the light from the scattering volume in the horizontal direction as well. Imagine a little square of scattering volume. Ultimately the desire is to get about one *coherence area* on the photosensitive area for optimal signal to noise.

Commercial digital correlators are available to calculate the intensity correlation function, $g^{(2)}(t)$. As the name implies these devices are digital and rely on detection of single photopulses, hence the alias photon correlation spectroscopy. Their time scales are typically 0.1 μs to 1 s and more. Thus the associated detector and electronics should be this fast.

Clean detection of just the scattered light leads to a situation called *homodyne detection*. Then Equation 13-54 holds. Sometimes some of the incident light finds its way to the detector by scattering off nonmoving parts of the apparatus such as cell walls, windows, or lenses. This light can mix with the scattered light from the particles and beat against it as a so-called local oscillator. Then one enters the heterodyne regime. If the intensity of the local oscillator is at least 30 times more than the desired scattered light, the field correlation function is detected. This boils down to the experimental form in Equation 13-52 without the factor of 2 in the exponential, that is, the correlation time in heterodyne detection is $\tau_c = 1/Dq^2$. Sometimes in an experimental situation some stray light cannot be avoided and a mix of hetero- and homodyne detection occurs. This intermediate situation cannot be analyzed. Then the wise adjustment is to let lots of local oscillator in until it is 30 times greater than the scattering and you are safely in the heterodyne regime.

A finite size distribution of particles will lead to an average intensity correlation function as

$$\langle g^{(2)}(t) \rangle = \int g^{(2)}[t, \tau_c(a)] I(a)n(a) da / \int I(a)n(a) da \quad (\text{Eq. 13-57})$$

Equation 13-57 shows a complex weighting with the product of the size distribution $n(a)$ and the scattering intensity, $I(a)$. Some commercial devices claim to unfold this complexity, but caution for these claims is warranted. Even with accurate unfolding, remember that the averaging is weighted by the scattering that favors the larger particles. This problem is discussed by Taylor et al. (1985) and Scrivner et al. (1986).

Nonspherical particles will diffuse and yield correlation functions. They have an effective mobility radius that can be substituted into the equation for the diffusion coefficient. The manner in which this mobility radius is related to the shape and size is discussed elsewhere in this book (chapter 23).

13.3.2 Flowing Systems

Many aerosol situations involve motion due to flow as well as Brownian motion, for example, a sooty flame. This flow will have its own characteristic time scale and cause additional “beam transit” terms. A potential problem lies with the beam transit term if it decays more rapidly than the diffusional term (i.e., if the beam transit is fast compared to the diffusion); the beam transit will cut off the diffusion term so that it cannot be measured to determine particle size. Chowdhury et al. (1984) and Taylor and Sorensen (1986) discuss the subtleties involved and methods to circumvent this problem.

13.4 EXPERIMENTAL METHODS FOR THE LABORATORY

There might be as many experimental methods as there are experimental scientists. This section describes some laboratory apparatuses that have been successfully used by researchers to conduct light-scattering experiments with aerosol systems.

Figure 13-9 shows a diagram of a detection apparatus that allows the researcher to see what their photodetector is detecting. In this diagram, laser light scattered from an aerosol issuing from a tube is collected by an imaging lens. This lens forms a real image of the laser beam as it passes through

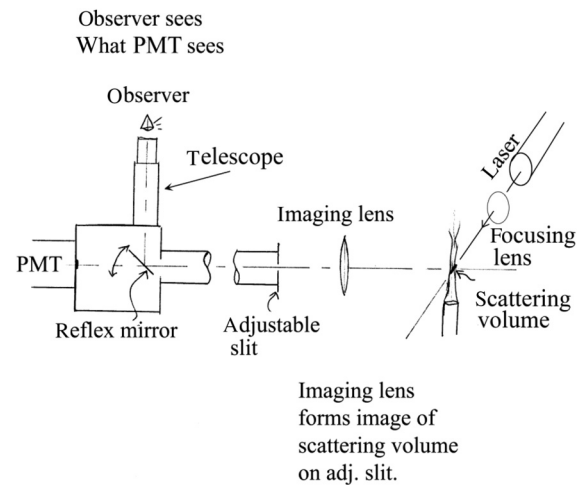


Figure 13-9 Scattering apparatus with adjustable slit and telescopic reflex observation.

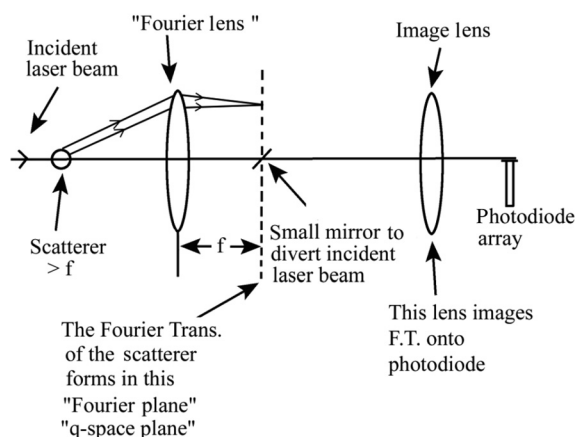


Figure 13-10 Small-angle (ca. $0.1\text{--}15^\circ$) scattering device.

and scatters from the aerosol onto either an adjustable slit or iris diaphragm (slits are better because irises rarely close to less than 1 mm). In this way the slit or iris can spatially filter the light and thereby select the portion of the scattering beam to pass on to the detector. Often the laser beam is horizontal and the slit is vertical, hence the resulting scattering volume is defined in these two directions. An observer can look through the short working distance telescope with the reflex mirror adjusted to a 45° angle and see this image masked by the slit or iris. In this way the observer knows exactly what part of the scattering aerosol will pass on to the detector when the reflex mirror is lowered out of the path. For DLS the beam can be narrowed by the focusing lens in the incident beam and the slit can be narrowed until good coherence is achieved on the detector. The entire detection side of this apparatus can be placed on an optical rail to pivot around the scatterer to different angles, hence different q value. The data in Figure 13-8b, above, were obtained with this apparatus.

Recent work in our lab has pioneered small-angle detection for measurement of large aggregates in aerosols. Our small-angle apparatus, Figure 13-10, is fashioned after that described by Ferri (1997). Laser light is scattered from an aerosol. The first lens, the "Fourier lens," is slightly farther than its focal length from the scattering aerosol in the exact forward direction. One focal distance behind this lens, scattered rays parallel each other and are scattered at the same angle and thus at the same q and focus off axis onto the Fourier plane of the lens. Here the Fourier transform of the scatterers forms in q -space; exactly what we want. On axis is a small mirror to eliminate the bright laser beam. A second lens, the "image lens," images the Fourier plane onto a smaller linear photodiode array. Each photodiode element receives light for a given angle, hence given q . Thus we obtain, $I(q)$. Examples of the kind of complex data that can be obtained with this small-angle apparatus are given in Sorensen et al. (2003) and Kim et al. (2004, 2006).

13.5 OPTICAL MEASUREMENT TECHNIQUES: EX SITU SENSING

13.5.1 Introduction

Light scattering and extinction by small particles suspended in gases are widely applied to obtain information on the concentration and size distribution of the particles. Devices based on this principle combine *in situ* measurements in the airborne state of the particles with a high degree of automation. For practical applications, two kinds of instruments exist: light scattering and extinction by single particles and light scattering and extinction by an assembly of particles. Single particle techniques based on light scattering cover a size range from about 70 nm to more than $100\text{ }\mu\text{m}$ and are capable of measuring concentrations of less than 10^3 particles/ m^3 (cleanroom monitoring) to about 10^9 particles/ m^3 (aerosol research). Ensemble scattering of light is applicable for concentration measurements of particulate matter in the atmosphere from a few $\mu\text{g}/\text{m}^3$ to several hundred mg/m^3 .

Section 13.5.2 is devoted to single particle techniques known as optical particle counters (OPCs). In an OPC, aerosol is drawn through a light beam and light flashes scattered by single particles are received by a photodetector. The number concentration is determined from the count rate of the photoelectric pulses and the size of the particles is estimated from the pulse height. Optical particle counters are widely used in basic aerosol research, air pollution studies, and cleanroom monitoring. Since these various applications require different specifications of an instrument, characteristic features of an OPC-like permissible range of number concentration, sensitivity, sampling flow rate, classification accuracy, and size resolution are discussed on the basis of experimental results.

Aerosol photometers are useful as real-time dust monitors in industrial hygiene, for concentration measurements of atmospheric aerosols, and in aerosol inhalation studies. The linearity range of light intensity versus aerosol concentration is limited at high concentrations by multiple scattering and at low concentrations by the stray-light background. The noise level of sensitive instruments is determined by Rayleigh scattering from the air molecules.

13.5.2 Single Particle Optical Counters

13.5.2.1 General Remarks An optical particle counter (OPC) measures the size and number concentration of aerosol particles in a limited size range by means of light scattering by single particles. For this purpose, a stream of aerosol is drawn through a condensed light beam. Light flashes scattered from single particles are received by a photodetector and converted into electrical pulses. From the count rate of the pulses, the number concentration, and from the pulse

height, the size of the particles is derived. The light power that an individual particle scatters is a function of its size, refractive index, and shape. Particle sizing based on this principle has been known for more than 50 years. Meanwhile, the technique has been steadily developed and for about 40 years OPCs using white light illumination have been commercially available (Lieberman 1986). The invention of the laser has allowed the successful replacement of the white light illumination by coherent and monochromatic laser light. Important characteristic features of an OPC are its permissible range of number concentration, its sampling flow rate, its sensitivity (lower detection limit), and its size-measurement accuracy. The requirements for an OPC change for different kinds of applications. Thus the specifications of an instrument have to be adjusted to the specific measurement problem. Optical particle counters that cover these various kinds of applications are offered, for instance, by *CLI*, *PAC*, and *PMS*. Trends in development are handheld, battery-operated counters with a laser-diode as light source.

13.5.2.2 Calibration Procedures In recent decades, many theoretical response functions of commercial OPCs have been published. Meanwhile, menu-driven programs for PCs are available to carry out light-scattering calculations for spherical particles (Reist 1990). In spite of these theoretical calculations, OPCs are usually calibrated with monodisperse test aerosols of known size and refractive index. Instruments using incandescent lamps for particle illumination were calibrated by Whitby and Vomela (1967), Liu et al. (1974a,b), Willeke and Liu (1976), and Fissan et al. (1984). Experimental calibrations of white light as well as laser light counters with various test aerosols have been carried out by Gebhart et al. (1983), Chen et al. (1984), and Liu et al. (1985). More recent papers published by Liu and Szymanski (1986), Plomb et al. (1986), and Szymanski and Liu (1986) report experimental work on laser particle counters.

To produce monodisperse test aerosols, several-generation techniques can be used. Aerosols with a high degree of monodispersity are obtained if aqueous suspensions of polystyrene latex (PSL) are nebulized, dried, and drawn into the OPC (Gebhart et al. 1980). Another technique is the vibrating-orifice generator, which allows the calculation of the particle diameter to an accuracy of about 1% from the operating parameters of the generator (Berglund and Liu 1973). By varying the frequency of vibration, the liquid feed through the orifice, and the concentration of the aerosol material in the volatile solvent, monodisperse aerosols from about 0.3 to 30 μm in diameter can be produced for calibration purposes. For the generation of submicrometer aerosol standards, the principle of electrostatic classification can be used (Liu and Pui 1974). The aerosol material is either dissolved in a liquid or prepared as a colloidal suspension and then atomized through a jet nebulizer. After the mist

is dried, a polydisperse aerosol consisting of solid particles or of low volatility droplets remains. The polydisperse aerosol is then passed through a differential-mobility analyzer and particles within a narrow size range are extracted according to their electrical mobility. Instrument calibration techniques are presented in greater detail in Chapter 21.

When applying an experimentally calibrated OPC to an unknown aerosol, one has to keep in mind that light-scattering signals generally depend on the optical properties of the test aerosol. To overcome these problems, direct field calibration of OPCs has been proposed. A direct aerodynamic particle size calibration of OPCs by means of inertial impactors was performed by Marple and Rubow (1976). To obtain a single calibration point, two runs are made with the OPC. During one run, an impactor is attached to the inlet of the OPC and during the second run the impactor is removed. An analysis of the data from the two runs yields a calibration point corresponding to the 50% cutpoint size of the impactor. Changing the size of the impactor nozzle allows different calibration points to be obtained. Similar aerodynamic calibration procedures have been applied to a white-light 90°-counter by Büttner (1983) using a sampling cyclone and by Friehmelt and Heidenreich (1999) using an aerodynamic particle sizer (*TSI*).

13.5.2.3 Optical Systems In the following discussion, typical optical arrangements used in laboratory and commercial OPCs are presented.

The optical setup of a forward-scattering instrument with converging illumination from an incandescent light source and a coaxial collecting aperture is shown in Figure 13-11. This configuration was used, for instance, in the former models PC 215, PC 245, PC 247, and PC 2102 (*HIA*) and is typical for an optical arrangement using forward scattering. Light from an incandescent lamp is concentrated in the sensing volume by a system of condenser lenses forming an illumination cone of 5° semi-angle. After passing the sensing volume, the primary light beam is absorbed in a concentric light trap with a half-angle of 16°. Light scattered by individual particles is collected through a coaxial aperture of 25° half-angle and directed onto the cathode of a photomultiplier. Considering the illumination cone, scattered light covering an angular range from about 10° to 30° is collected by the system.

Experimental response curves of the models PC 215 and PC 245 (*HIA*) measured with PSL spheres and droplets of dioctyl phthalate (DOP) were reported by Willeke and Liu (1976). A characteristic feature of this forward-scattering sensor is a multivalued region in the response curve between 0.7 and about 1.2 μm .

The counter model CI-208 (*CLI*) shown in Figure 13-12 utilizes an elliptical mirror in its optical system. In the detector, the particle-sensing zone is located at the primary focal point of the elliptical mirror. High-intensity light from a

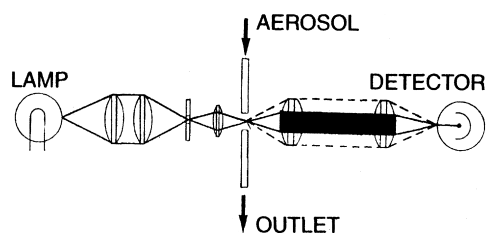


Figure 13-11 Optical system of a forward-scattering instrument using an incandescent light source.

quartz halogen lamp is focused on the sensing zone, where it illuminates each traversing particle.

Light scattered from each particle is collected over an angular range from 15° to 105° and is directed to a photodetector located at the secondary focal point of the ellipsoid. The sample air is surrounded by a sheath of clean filtered air, allowing the precise placement of the particles at the primary focal point. At a sample flow rate of $1.2 \times 10^{-4} \text{ m}^3/\text{s}$ [7 L/min], a size sensitivity of $0.3 \mu\text{m}$ is quoted by the manufacturer. Experimental calibrations of the Climet instrument were carried out by Clark and Avol (1979), Makynen et al. (1982), and by Chen et al. (1984). A monotonically increasing response function for PSL and DOP aerosols were found over the entire size range from 0.3 to $10 \mu\text{m}$.

Using laser light illumination, intensities can be realized in the sensing volume several orders of magnitude higher than those obtained with incandescent light sources. Furthermore, a collimated laser beam needs fewer optical elements, such as stops and lenses, reducing the stray-light background in the chamber considerably. Three kinds of particle illumination exist with laser light: (1) the output of a laser can be focused into the sensing volume like a common incandescent light source; (2) according to Knollenberg and Luehr (1976), high illumination intensities with a low-power laser can be achieved if the sensing volume is positioned inside the laser resonator (active scattering); and (3) in the passive cavity system, the original laser output is multiply reflected to create high-intensity illumination.

A high-resolution laser aerosol spectrometer for laboratory purposes was developed by Roth and Gebhart (1978) for the

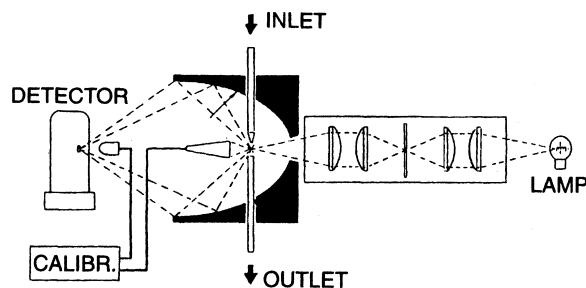


Figure 13-12 Optical system of the particle counter CI-208 (CLI). Reprinted from Gebhart (1991) with permission.

size range between 0.06 and $0.6 \mu\text{m}$. An argon ion laser ($\lambda = 0.5145 \mu\text{m}$) with an output of 2 W serves as external light source. The laser light is focused by an astigmatic system of lenses into the sensing volume. The light scattered by the particles is collected by a microscope objective at a mean scattering angle of 40° .

An example of an active cavity sensor is shown in Figure 13-13. It is contained in models LAS-X, MS-LAS, LPC 101 and MicroLPC0710 (PMS) and in the model 226/236 (HIA). This sensor employs a high-Q laser cavity to achieve a high illumination intensity ($\sim 500 \text{ W}/\text{cm}^2$).

The primary collector of the scattered light is a parabolic reflector. Particles in the sample stream intersect the laser beam within the cavity at the focus of the paraboloid, which focuses the scattered light onto a 45° flat mirror. The light reflected from this mirror is refocused onto a photodetector by an aspheric lens. The whole system collects scattered light from 35° to 120° providing a 2.2 steradian solid angle. The aerosol stream is aerodynamically focused. The theoretical response functions of this sensor have been published by Hinds and Kraske (1986) and experimental calibration data have been reported by Szymanski and Liu (1986).

The LASAIR series (PMS) are instruments with a passive cavity design. They are available at minimum sizing thresholds of 0.1 , 0.2 , 0.3 , and $0.5 \mu\text{m}$ and with sample flow rates from 9.44×10^{-7} to $4.72 \times 10^{-4} \text{ m}^3/\text{s}$ [0.002 to $1 \text{ ft}^3/\text{min}$].

Most OPCs utilize an aerosol nozzle to transport the particles through the beam of illuminating light. In this case, the sensing volume is limited by the cross section of the aerosol stream and the width of the light beam. Using an aerosol nozzle has the advantage that, under stable flow conditions, the sensing volume and the sample flow rate are well-defined. In most instruments, the aerosol stream is surrounded by a clean air sheath, which establishes a stable flow towards the outlet of the measuring chamber and, thus, avoids stray particles in the optical system. The clean air sheath can additionally be used to focus the aerosol stream aerodynamically down to a filament of less than 0.1-mm diameter. The problem that arises in connection with an aerosol nozzle is that a sample representative of all particle sizes has to be taken out of the sampled aerosol. Therefore, systems also have been developed that can count individual aerosol particles directly in the main stream of an aerosol.

Such an instrument is, for instance, the particle counter HC 15 (PLY), which forms its sensing volume by optical means only (Umhauer 1980). The optical system, which is schematically drawn in Figure 13-14, consists of two optical pathways, one for illumination and one for the collection of scattered light.

The lenses I and II project miniaturized images of square masks (stop I and II) into the measuring chamber, where the two optical axes cross at right angles. The images of stop I and II, which coincide with the crossing point of the two axes, form the sensing volume. Particles passing this

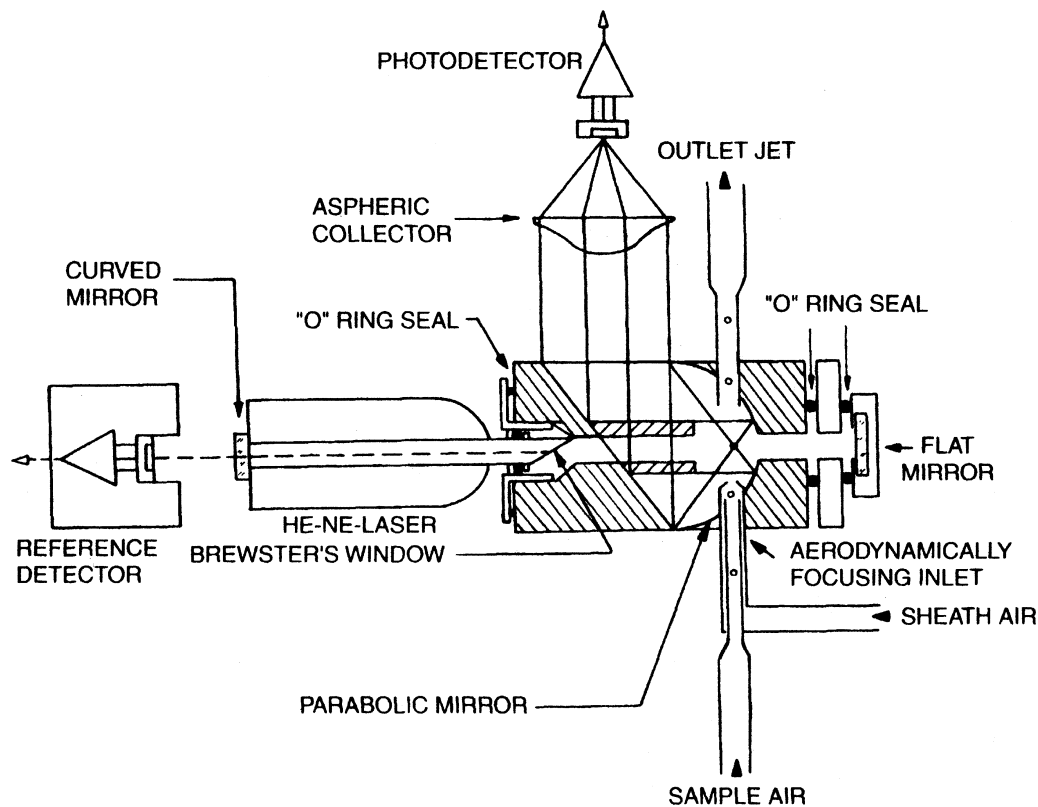


Figure 13-13 Setup of an active scattering laser spectrometer used in the models LAS-X, HS-LAS, and LPC 101 (*PMS*) and in the models 226/236 (*HIA*). Reprinted from Gebhart (1991) with permission.

optically defined sensitive area are illuminated with incandescent light and the light scattered by individual particles is collected at a mean scattering angle of 90° . Since an optically defined sensing volume can be made very small (about $100\ \mu\text{m}$ across), high concentrations can be measured with such an instrument. The advantage of such a system is that all difficulties associated with aerosol sampling through

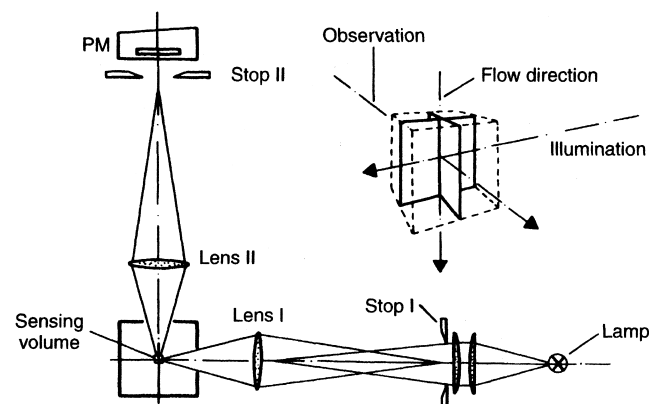


Figure 13-14 Arrangement of Counter HC 15 (*PLY*), which forms the sensing volume by optical means only. Reprinted from Gebhart (1991) with permission.

inlets and small nozzles are avoided. There exist, however, problems in exactly defining the sensing volume and the sample flow rate. Whereas small particles are only counted when they pass the central region of the stop, larger particles can also give rise to countable pulses at the periphery of the imaging. Since these pulses are smaller than if the particle passed through the center of the detection volume, they are sensed as coming from smaller particles. Thus, the effective sample flow rate is particle size-dependent. The bigger the particles, the more the peripheral detection contributes to the measured cumulative number distribution. This has been shown in an experimental analysis of the HC 15 counter by Helsper and Fissan (1980). The authors passed monodisperse $9\text{-}\mu\text{m}$ droplets through the sensing volume and found that about 50% of the count pulses were attenuated and simulated smaller droplets down to a detection limit of $0.3\ \mu\text{m}$.

A method to eliminate the effect of the border zone on the measured particle size distribution was reported by Knollenberg and Luehr (1976) and Umhauer (1983). Its principle of operation is illustrated in Figure 13-15.

A beam splitter behind the collecting optics directs the scattered light through masked apertures on two independent detectors. The signals from the two detectors, in conjunction with double pulse height analysis, lead to a system that determines the position of a particle in the light beam and rejects

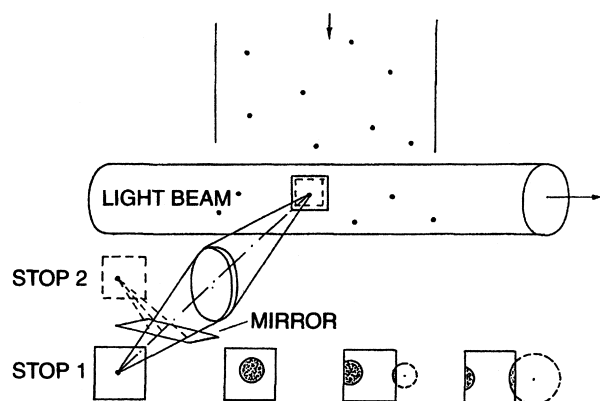


Figure 13-15 Elimination of particles traversing the periphery of the sensing volume by means of a two-beam system and masked apertures.

all counts originating from particles in the border zone. The model HP-LPC (*PMS*) contains a sensor of this kind that can be directly installed in a conduit for gases. Although the sensing area of this model covers only a fraction of a percent of the conduit's cross section, a unique linear relationship between count rate and number concentration is obtained for all particle sizes above the detection limit. Umhauer (1983) constructed two independent rectangular collector and detector units for the model HC 15 (*PLY*), which overlapped in the sensing volume and differed only in the size of the masks. The two different masks, in combination with double pulse analysis, allowed identification and rejection of those particles which passed the sensing volume in the border zone. An improved version of this two-channel detector device was investigated by Sachweh et al. (1998). A modified type of this instrument is commercially available (PCS-2000, *PAS*).

13.5.2.4 Pulse Processing The light flashes originating from individual particles in the sensing volume are converted into photocurrent pulses. Due to the fast time resolution of most photodetectors, the pulse shape follows the light intensity profile inside the sensing volume. The intensity profile is approximately a Gaussian one and has a pulse width from several to about 40 μs , depending upon the OPC used. The output pulses of the photodetector are usually fed to a current-to-voltage transducer, the main part of which consists of a high-frequency amplifier. Then a decision has to be made whether the pulse amplitude or its total charge (area) will be used as a measure of the scattered light. The charge integration method improves the resolution and the sensitivity of an OPC considerably, provided the pulse duration is very constant for all particles. A clean air jacket in conjunction with aerodynamic focusing of the aerosol stream results in a constant pulse duration necessary for charge integration. In general, a multi-channel analyzer requires a constant

pulse height of a few microseconds duration in order to read the signal height. Therefore, the amplifier output signal—which is proportional either to the amplitude or to the area of the original pulse—has to be stretched in a pulse converter. The pulse stretching introduces an electronic dead time during which no additional signals are processed. Additionally, the converter removes low-frequency components and DC offset from the incoming signal.

A further improvement of the signal evaluation is obtained, if the photomultiplier signals are digitized directly after the current-to-voltage transducer (Sachweh et al. 1989, 1998). By this procedure the raw signal containing electronic noise ripples is converted into nearly a square wave the base-line of which is given by the transit time of the particle through the sensing zone. This allows a well-defined determination of the mean pulse height.

Most OPCs have an analog output that can be connected directly to an oscilloscope. Observations of the pulse shape show that in some instruments many stray particles pass the sensing volume, producing pulses up to ten times longer than the normal ones. Since pulse times of this length exceed the recovery time of the electronics, multiple counts can originate from a single stray particle and be classified as small particles (Gebhart et al. 1983). The existence of the stray particles themselves may be explained by unstable flow conditions that prevent particles from being completely removed from the measuring chamber after their initial passage through the light beam.

13.5.2.5 Range of Number Concentration Number concentration c_0 of the aerosol, sample flow rate Q and counting rate dN_p/dt of a particle counter are connected by the relationship

$$dN_p/dt = c_0 Q \quad (\text{Eq. 13-58})$$

Equation 13-60 assumes that each particle contained in the sample flow produces a single count. In practice, however, counting losses due to coincidences occur. Less than 10% loss in particle counts approximately requires (van der Meulen et al. 1980)

$$c/c_0 = \exp\{-c_{\max} Q t_r\} \geq 0.9 \quad (\text{Eq. 13-59})$$

where t_r is the recovery time of the electronics between successive count events, including the transit time of the particle through the light beam and the pulse processing time of the multichannel analyzer. From Equation 13-59, it can be seen that for a given recovery time t_r , measurements at high number concentrations are only possible at the expense of the sample flow rate Q and vice versa. Some maximum permissible number concentrations derived from Equation 13-59 for a typical recovery time of $t_r = 20 \mu\text{s}$

TABLE 13-1 Maximum Permissible Number Concentration in an OPC in Relation to the Volumetric Flow Rate^a

Q (m ³ /s)	4.72×10^{-4}	4.72×10^{-5}	4.72×10^{-6}	4.72×10^{-7}	4.72×10^{-8}
c_{\max} (m ⁻³)	1.1×10^7	1.1×10^8	1.1×10^9	1.1×10^{10}	1.1×10^{11}

^aEvaluated from Equation 13-30 for an electronic recovery time of 20 μ s.

are shown in Table 13-1. As indicated, c_{\max} never falls below $3.5 \times 10^6/\text{m}^3$, which corresponds to ISO Class 8 (particles per $\text{m}^3 > 0.5 \mu\text{m}$) as defined in ISO 14644-1 (see Chapter 36). Coincidence errors, however, are important if OPCs are applied to laboratory or environmental aerosols.

EXAMPLE 13-5

A filter with an expected penetration of 0.01 for $0.5 \mu\text{m}$ is checked with an OPC. The OPC samples aerosol at a flow rate of $47.16 \times 10^{-6} \text{ m}^3/\text{s}$ [2.83 L/min] and has an electronic recovery time of 12 μs . Monodisperse $0.5\text{-}\mu\text{m}$ particles with a true number concentration of $c_0 = 4 \times 10^8 \text{ m}^{-3}$ serve as the test aerosol. Calculate the experimental error due to coincidence if no dilution steps are used.

Answer: The experimental penetration is c_2/c_1 , where c_1 and c_2 are the measured concentrations upstream and downstream of the filter. Using Equation 13-61, the count loss due to coincidence is:

$$\frac{c_1}{c_0} = \exp(-c_0 Q t_r) = \exp[(-4 \times 10^8 \text{ m}^{-3}) \times (47.1 \times 10^{-6} \text{ m}^3/\text{s}) \times (12 \times 10^{-6} \text{ s})] = 0.797$$

$$\frac{c_2}{c_0} = \exp(-0.01 c_0 t_r) = \exp[(-4 \times 10^6 \text{ m}^{-3}) \times (47.16 \times 10^{-6} \text{ m}^3/\text{s}) \times (12 \times 10^{-6} \text{ s})] \approx 1$$

The error is:

$$\Delta \frac{c_2}{c_0} = \left[\frac{c_2}{c_1} - \frac{c_2}{c_0} \right] = \frac{c_2}{c_0} \left[\frac{1}{0.797} - 1 \right] = 0.25 \frac{c_2}{c_0}$$

The lower limit c_{\min} of the detectable number concentration depends on the background noise according to:

$$c_{\min} > c_{\text{ns}} = [dN_p/dt]_{\text{ns}}/Q \quad (\text{Eq. 13-60})$$

where $(dN_p/dt)_{\text{ns}}$ is the rate of noise pulses and c_{ns} an apparent number concentration produced by noise. Count noise can originate from internal particle sources, the electronics, ionizing radiation, and instabilities of the power supply. There is a general agreement that reliable concentration measurements with an OPC should start only at levels more than one order of magnitude above the background, that is, $c_{\min} \geq 10 c_{\text{ns}}$. For the determination of the noise level of an OPC, filtered air is drawn through the instrument for several hours. Measurements of this kind have been reported by Gebhart and Roth (1986), Wen and Kasper (1986), Liu and Szymanski (1987), and Gebhart (1989a). Some results of background noise are presented in Table 13-2.

In most cases, particles originating from the internal flow system have been identified as being responsible for the count noise. This can be concluded from the wash-out effect of the instruments and their different behavior in the positions “pump on” and “pump off.” Wash-out here means that the rate of noise counts decreases with time when the instrument is supplied with particle-free air. After an exposure to environmental aerosols, the instruments needed up to 15 h to obtain a stable count rate at a low level (Gebhart and Roth 1986).

In general, OPCs with incandescent light sources have somewhat lower noise levels. After completion of the

TABLE 13-2 Specifications and Count Noise of a Selection of Commercial Optical Particle Counters^a

Light Source	Model	Receiver Optics	Q (m ³ /s)	Noise Counts per m ³	
				Pump On	Pump Off
Incandescent light	HIAC/ROYCO 4102	10°–30°	4.72×10^{-5}	530 > 21	Wash-out
	HIAC/ROYCO 5000	50° range	1.67×10^{-5}	84.8	~0
	CLIMET CI 8060	15°–150°	4.72×10^{-4}	0.95	~0
Laser light	PMS LAS-X	35°–120°	5.00×10^{-6}	10,840 > 210	Wash-out
	PMS LPC-110	35°–120°	4.72×10^{-5}	<17.6	~0
	HIAC/ROYCO 5100	60°–120°	4.72×10^{-4}	4236 > 28	Wash-out
	TSI 3755	15°–88°	4.72×10^{-5}	<35.3	
	CLIMET C1 6300	45°–135°	4.72×10^{-4}	<70.6	

^aData from Gebhart and Roth (1986) and Gebhart (1989a).

wash-out, most instruments with a sensitivity of $0.5\ \mu\text{m}$ are prepared to monitor ISO Class 4 or 3 (Table 36-5). For the detection of ISO Class 3, for instance, instruments with a sensitivity of $0.5\ \mu\text{m}$ must produce less than 3.5 noise counts per m^3 , whereas laser counters with a sensitivity of $0.1\ \mu\text{m}$ need a background level smaller than 100 counts per m^3 (see Chapter 36). In one model the count rate of noise in the first channel ($0.1\text{--}0.3\ \mu\text{m}$) increased with time of operation, indicating that heating during the course of operation may have affected electronic noise. The high background in another instrument was caused by a leak in the housing and vanished when the instrument was put in a filtered laminar flow box (Gebhart and Roth 1986). From these experimental findings it is obvious that a certain model does not necessarily guarantee a low noise level. It is rather the status of an individual device and its history (exposure to concentrated aerosols) that determines the background noise. Therefore, instruments used for monitoring cleanroom Class 100 or lower should be carefully checked before measurements are taken.

13.5.2.6 Sensitivity and Sample Flow Rate Manufacturers usually express the sensitivity of an OPC as the smallest particle diameter d_{\min} detectable with the instrument. According to a convention of the German standard setting organization [Verein Deutscher Ingenieure (VDI) 3491, number 3], however, sensitivity should be associated with counting efficiency and the particle size with 50% counting efficiency taken as the lower detection limit d_{\min} . For the determination of the counting efficiency η near the lower detection limit the measured concentration c has to be related

to the concentration c_0 obtained by independent reference methods according to

$$\eta = \frac{c}{c_0} \quad (\text{Eq. 13-61})$$

During an experimental run, instruments to be checked simultaneously sample a monodisperse test aerosol from a common reservoir together with a reference instrument. Using this procedure, counting efficiencies of OPCs were measured by van der Meulen et al. (1980), Gebhart et al. (1983), Gebhart and Roth (1986), Wen and Kasper (1986), Liu and Szymanski (1987), and Gebhart (1989a).

A difference between c and c_0 can originate from (1) coincidence losses, (2) an incorrect sample flow rate Q , and (3) a decreasing sensitivity of the instrument. The effects of these parameters on counting efficiency can be separated by means of the coincidence curve of an instrument, where the ratio c/c_0 is plotted versus the reference concentration c_0 . Coincidence curves of two instruments measured by Gebhart (1989a) are shown in Figures 13-16 and 13-17. Starting with test aerosols far above threshold, a single curve is obtained for all particle sizes in a semilogarithmic plot. If the extrapolation of this curve to zero concentration ($c_0 \rightarrow 0$) deviates from 1, the sample flow rate of the instrument is not correct. Deviations from this curve for particle sizes approaching the lower detection limit indicate a decreasing sensitivity of the instrument. If counting efficiencies are generally evaluated by extrapolating the measured concentration ratio c/c_0 back to zero concentration, coincidence losses are eliminated and the counting efficiency reflects a specific property of an instrument.

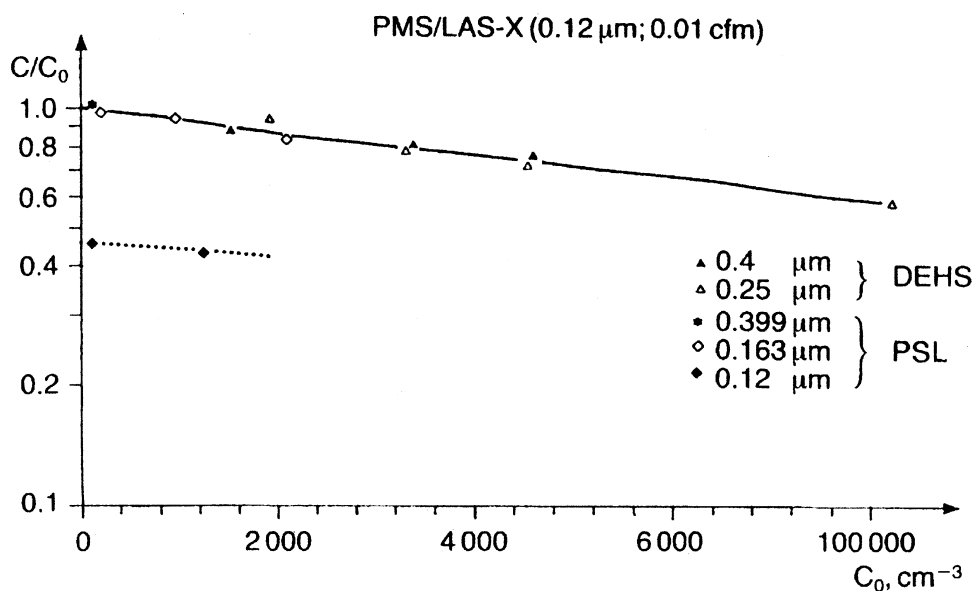


Figure 13-16 Experimental coincidence curve of the laser spectrometer LAS-X (PMS).

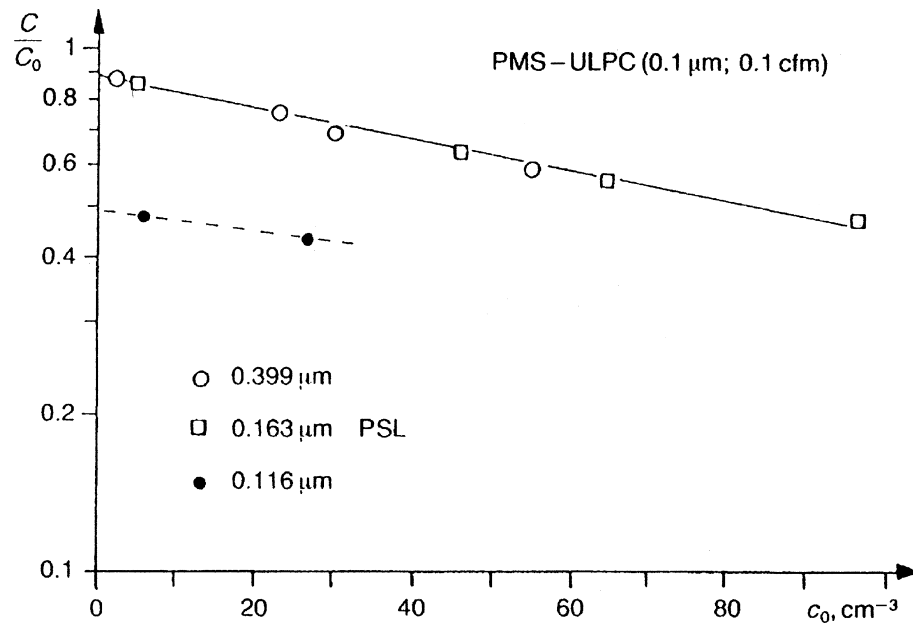


Figure 13-17 Experimental coincidence curve of the laser counter ULPC (PMS).

Counting efficiencies of different OPCs obtained by this extrapolation technique are summarized in Table 13-3 (Gebhart 1989a).

In the submicrometer size range, the counting efficiency decreases with decreasing particle size so that the lower detection limit is a gradual transition rather than a sharp

step. The data confirm previous findings by van der Meulen et al. (1980) and Gebhart et al. (1983) that instruments using incandescent light count 0.32-μm particles with an efficiency of less than 20%. For most laser instruments, on the other hand, counting efficiencies near 100% are achieved down to particle diameters of 0.1 μm. With the highly

TABLE 13-3 Specifications and Counting Efficiency of a Selection of Commercial Optical Particle Counters^a

			Counting Efficiency at Diameter d_p (μm)						
Incandescent Light	d_{\min} (μm)	Q (m ³ /s)	0.163	0.22	0.32	0.47	0.72	0.95	2.02
<i>Model</i>									
HIAC/ROYCO 227	0.3	4.72×10^{-6}			0.12	0.92		1.05	
HIAC/ROYCO 4102	0.3	4.72×10^{-5}			0.18	1.01		0.98	
HIAC/ROYCO 5000	0.3	1.67×10^{-5}			0.18	0.89	0.91		
CLIMET CI 8060	0.3	4.72×10^{-4}			0.15	1.02	0.98		
			Counting Efficiency at Diameter d_p (μm)						
Laser Light	d_{\min} (μm)	Q (m ³ /s)	0.068	0.082	0.109	0.12	0.163	0.22	0.32
<i>Model</i>									
PMS LAS-X	0.12	5.00×10^{-6}				0.46	0.98		1.02
PMS LAS-X	0.9	1.00×10^{-6}			0.98	0.98	0.99		
PMS LPC-110	0.1	4.72×10^{-4}				0.47	0.98	1.0	
PMS MS-LAS	0.065	5.00×10^{-6}	0.27	1.03	0.97		1.04		
HIAC/ROYCO 5120	0.2	4.72×10^{-4}			0.24	0.94	0.99	1.0	
HIAC/ROYCO 236	0.12	5.00×10^{-6}					1.03	0.99	1.0

^aData from Gebhart and Roth (1986) and Gebhart (1989a).

sensitive model MS-LAS (*PMS*), even particles of $0.07\text{ }\mu\text{m}$ can be counted with an efficiency of about 30% at a reduced sample flow rate of $300\text{ cm}^3/\text{min}$.

EXAMPLE 13-6

The sensitivity of a laser particle counter (LPC) has been determined with PSL spheres to be $d_{\min} = 0.1\text{ }\mu\text{m}$. The LPC shall now be applied to droplets of di-2-ethylhexyl sebacate (DEHS). Calculate the shift in the sensitivity of the LPC for DEHS droplets.

Answer: One has to calculate the diameter of a DEHS droplet that scatters the same flux of light as a PSL sphere of $0.1\text{ }\mu\text{m}$ in diameter. In the size range of $0.1\text{ }\mu\text{m}$, the Rayleigh approximation of Equations 13-21 and 13-30 can be applied, which for identical optical arrangements, reduces to:

$$d_{\text{PSL}}^6 \left| \frac{m^2 - 1}{m^2 + 2} \right|_{\text{PSL}}^2 = d_{\text{DEHS}}^6 \left| \frac{m^2 - 1}{m^2 + 2} \right|_{\text{DEHS}}^2$$

PSL: $m = 1.59$, $d = 0.1\text{ }\mu\text{m}$

DEHS: $m = 1.45$

$$\begin{aligned} d_{\text{DEHS}} &= d_{\text{PSL}} \left[\frac{\left| \frac{m^2 - 1}{m^2 + 2} \right|_{\text{PSL}}^2}{\left| \frac{m^2 - 1}{m^2 + 2} \right|_{\text{DEHS}}^2} \right]^{1/6} \\ &= d_{\text{PSL}} \left[\frac{\left| \frac{2.528 - 1}{2.528 + 2} \right|_{\text{PSL}}^2}{\left| \frac{2.103 - 1}{2.103 + 2} \right|_{\text{DEHS}}^2} \right]^{1/6} \\ &= 0.108\text{ }\mu\text{m}, \text{ a small change} \end{aligned}$$

In the supermicrometer size range, satisfactory results are obtained. However, for particle diameters above $2\text{ }\mu\text{m}$, inlet losses in the sampling system may again affect counting efficiency, especially if instruments with lower sampling rates are used in connection with plastic tubes. The sampling efficiency of the particle counter Royco 245 was investigated by Willeke and Liu (1976). Comprehensive studies of inlet characteristics and their effect on the counting efficiency of an optical sensor have been carried out by Tufto and Willeke (1982) and by Okazaki and Willeke (1987). Fissan and Schwientek (1987) performed a review of aerosol sampling and transport. Further information on sampling efficiency and aerosol transport is given in Chapter 6.

Table 13-3 indicates that the sensitivity of an OPC can be increased by using laser light illumination. On the other hand, it can be seen from this table that there exists a close connection between the sampling flow rate Q of a laser particle counter and its smallest detectable particle size d_{\min} . The

lower the sampling flow rate, the more sensitive is the instrument. This is because above a certain illumination intensity, light scattering by the air molecules within the sensing volume becomes the limiting factor for the sensitivity. Under these circumstances, the signal-to-noise ratio of an OPC can only be further improved by a reduction of the number of molecules that scatter light into the detector; in other words, an increase in sensitivity is only possible at the expense of the sensing volume and, in consequence, at the expense of the sampling flow rate. It can be shown that 1 mm^3 of air scatters about the same amount of light as a $0.22\text{-}\mu\text{m}$ particle with refractive index $m = 1.5$. This principal limitation of the sensitivity of an OPC exists regardless of the kind and intensity of illumination. The alternatives in cleanroom technology, therefore, seem to be either to use an instrument with high sensitivity ($0.1\text{-}\mu\text{m}$ diameter particles) but a lower sampling rate or a less sensitive device with a higher sampling rate ($4.72 \times 10^{-4}\text{ m}^3/\text{s}$ [$28.3\text{ L}/\text{min}$]).

In a more recent development by *PMS*, successful attempts have been made to overcome the problem of Rayleigh scattering on gas molecules. In these models an elongated sensing volume is imaged onto a photodetector array consisting of independent elements. Owing to the facet structure of the detector unit, each element views only part of the gas molecules of the sampling flow but records the total flux of light scattered by a single traversing particle. With this segmentation technique, laser particle counters can be constructed that combine a high sensitivity ($0.1\text{ }\mu\text{m}$) with a high sampling rate of $28.3\text{ L}/\text{min}$. For instance, the model LPC 110 (*PMS*) in Table 13-3 is an instrument based on this technique.

13.5.2.7 Sizing Accuracy and Resolving Power The sizing accuracy of an OPC describes its ability to measure the geometrical diameter of aerosol particles by classifying their photoelectric pulse heights into channels of given size intervals. For the evaluation of the sizing accuracy, cumulative size distributions of well-characterized test aerosols are compared to those measured with the OPC (Gebhart et al. 1983; Liu et al. 1985; Szymanski and Liu 1986). The count median diameter derived from these measured size spectra are compared to the true size of the test aerosol to provide a measure of the sizing accuracy. Examples of cumulative size spectra measured with different OPCs by Gebhart et al. (1983) are shown in Figure 13-18. The PSL test aerosols have been analyzed by electron microscopy.

Regarding the sizing accuracy, one has to distinguish between avoidable and unavoidable errors. Avoidable errors are systematic shifts on the size scale. They can be corrected by changing the linear amplification factor of the electronics. Unavoidable errors exist as long as the calibration curve has an ambiguous part or the calibration standard differs in refractive index from the aerosol to be investigated.

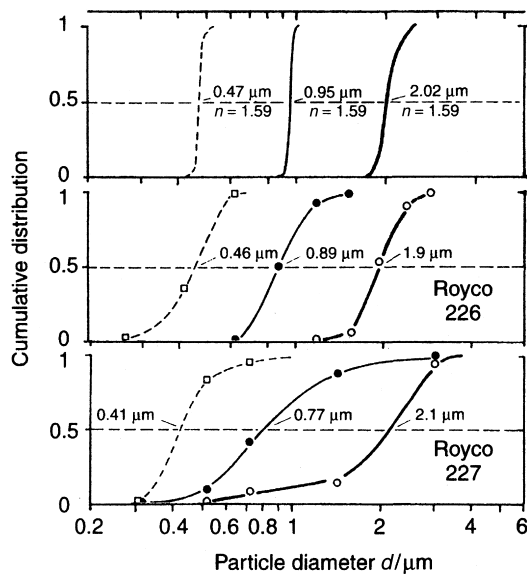


Figure 13-18 Cumulative size distributions of different PSL test aerosols (above) in comparison to measurements with different OPCs. Adapted from Gebhart et al. (1983).

Because of a multivalued part in the response function of the forward-scattering sensor shown in Figure 13-11, PSL spheres of 0.95 μm in diameter are classified as 0.77- μm particles (see Fig. 13-18). An extreme example of the effect of refractive index are measurements of opaque particles (coal dust, India ink) in an OPC that applies forward scattering and has been calibrated with transparent spheres (Whitby and Vomela 1967; Willeke and Liu 1976). In this case, particles of the same geometrical size differ by about one order of magnitude in the flux of scattered light, which reduces the measured size of the particles by about a factor of three.

The resolution power of an OPC describes its ability to distinguish two monodisperse aerosols of different mean particle size. It depends on the slope of the calibration curve and on the ability of an OPC to produce uniform pulses upon exposure to a monodisperse aerosol. The main factors influencing the resolution power are the homogeneity of illumination in the sensing volume and optoelectronic noise.

Since the homogeneity of illumination is affected by the alignment of the optics, instruments of the same model may not have the same resolution due to normal manufacturing tolerances. To measure the resolution power, a monodisperse aerosol of known size and standard deviation is sampled by the OPC and the instrumental broadening of the size distribution is determined. This can be done either directly by recording differential spectra (Liu et al. 1974a; Roth and Gebhart 1978) or by evaluating the slope of a cumulative size distribution (see Fig. 13-18).

A typical indication of nonuniform illumination of the particles is the recorded spectra having a sharp cutoff with

respect to bigger particles and a gradual cutoff with respect to smaller sizes. Optoelectronic effects on the resolution power of an OPC become important only near the lower particle size detection threshold, where the noise ripples are comparable to the particle signals. The modulation of the particle signal by quantum-statistical processes in the photodetector reduces the resolution power near threshold considerably, but has no effect for bigger particles that contain enough photons in their scattered light pulses (Liu et al. 1974a). For instruments with an optically defined sensing volume, the resolution power is additionally diminished by the effect of the border zone (Helsper and Fissan 1980).

With well-designed laser aerosol spectrometers, size resolutions comparable to that of electron microscopy can be achieved, especially in the size range below the wavelength of light (Roth and Gebhart 1978; Knollenberg 1989).

13.5.3 Multiple Particle Optical Techniques

13.5.3.1 General Considerations Multiple particle detection instruments, such as photometers or nephelometers, based on scattered-light intensity are useful for concentration measurements of aerosols if certain requirements are met. For the determination of concentration ratios or relative concentrations, the composition of the aerosol (particle size distribution, refractive index) must be constant during a series of experimental runs. For absolute measurements of mass concentration, the photometer must be calibrated with the aerosol to be investigated. In both cases, the instrument must be operated in its linear range, where the number of particles in the sensing volume is linearly correlated with the photometer signal. This range of linearity is limited at high concentrations by multiple scattering and at low concentrations by the stray-light background in the chamber.

Stray light originates from optical elements such as lenses, glass windows, and optical stops. Well-designed instruments are limited by Rayleigh scattering from the air molecules, resulting in nearly steady-state noise levels. By replacing air with a gas of known scattering properties, it is possible to calibrate a photometer in terms of scattering cross section. A measure of the stray-light background is the photometer response in the presence of particle-free air. Concentration ratios evaluated from photometer responses R_i are measured correctly only if the contribution of the background R_{ns} is either negligible or subtracted from the photometer reading:

$$\frac{c_1}{c_2} = \frac{R_1 - R_{ns}}{R_2 - R_{ns}} \quad (\text{Eq. 13-62})$$

In all cases where the analog signal is subjected to electronic data processing, the photometer should be adjusted to a zero response for particle-free air.

From the lower detection limit to onset of multiple scattering, the linearity range of a typical photometer can span at least three orders of magnitude in number concentration. Aerosol photometers in combination with inert aerosols are currently applied in filter testing and in aerosol medicine. They are also useful as real-time dust monitors in industrial hygiene (Chapter 25) and for continuous recordings of aerosol concentrations in the atmosphere (Chapters 26 and 27). In general, instruments based on light scattering are much more sensitive than light extinction systems.

13.5.3.2 Performances in Use

Aerosol Inhalation Studies Since the pioneering work of Altshuler et al. (1957), photometers in combination with monodisperse test aerosols have been used in aerosol research to measure the total deposition of aerosol particles in the human respiratory tract as well as to study gas mixing processes and deposition mechanisms inside the airways (Gebhart et al. 1988; Gebhart 1989b). An integral photometer developed for aerosol inhalation studies is shown in Figure 13-19.

Its cylindrical aerosol channel can pass sample flow rates up to $1 \text{ m}^3/\text{min}$. An expanded parallel beam (3-mm diameter) of a HeNe laser traverses a system of diaphragms, crosses the aerosol channel, and is absorbed in a light trap. Light scattered by the particles within the angular range of $90^\circ \pm 14^\circ$ is collected by a lens L_1 , which images the illuminated particles onto a slit stop. The slit stop confines the sensitive volume to about 100 mm^3 and keeps stray light from reaching the photomultiplier. A second field lens L_2 images the aperture of lens L_1 onto the cathode of the photomultiplier. The instantaneous aerosol concentration is represented by the anode current of the photomultiplier, which, after

amplification, can be used for data processing. The photometer technique permits continuous recording of the aerosol concentration close to the mouth during the entire course of a breathing cycle. From such records and simultaneous measurements of respiratory volumes and flow rates the amount of aerosol in successive fractions of inspired and expired air can be evaluated. Data of this kind provide new possibilities for lung function tests (Gebhart et al. 1988; Heyder 1994).

An improved version of this inhalation measurement technique is the Respiratory Aerosol Probe (**PAR**). In this device, the analog signals of aerosol number concentration and of respiratory flow rate are measured simultaneously at the entrance of the respiratory tract and fed to a personal computer for automatic data collection and processing (Westenberger et al. 1992). In the photometer unit, the beam of a 3 mW laser diode ($\lambda = 0.78 \mu\text{m}$) is collimated to illuminate about 70% of the cross section of an elliptically shaped respiratory channel. Light scattered by inspired particles within an angular range $90 \pm 32^\circ$ is collected and projected onto a miniaturized photomultiplier. The respiratory channel of the photometer is immediately connected with the mouthpiece and can be supplied with either clean air or aerosol by switching a set of pneumatic valves. The aerosol can be applied as a continuous flow or in boluses with volumes down to $2 \times 10^4 \text{ mm}^3$ [20 cm^3]. The respiratory flow rate is measured with a pneumotachograph, which yields the inspired air volumes after integration.

Occupational and Environmental Hygiene The TM digital μP (**HUN**) is an instantaneously reading respirable dust photometer constructed for concentration levels in workplaces. The portable, battery-supplied instrument measures the infrared light ($0.94 \mu\text{m}$) scattered by airborne dust particles at a mean scattering angle of 70° . Its open measuring chamber, which is insensitive to daylight, is filled by natural convection and includes coarse particles (total dust). The photometer reading, however, is calibrated against the mass concentration of respirable dust by means of a gravimetric respirable dust sampler (see Chapter 25). Experiments carried out by Armbruster et al. (1984) using monodisperse test aerosols and industrial dusts confirm the instrument's principle. The photometer values obtained for industrial dusts can be linearly converted into mass values of respirable dust as long as ultra-coarse particles are excluded.

A respirable aerosol monitor RAM (**MIE**) allows real-time assessment of respirable dust by light scattering after aerodynamic separation of this fraction in a cyclone (Lilienfeld 1983). A miniature real-time aerosol monitor (model MiniRAM, **MIE**) incorporates a pulsed near-infrared light-emitting diode, a silicon detector, and various collimating and filtering optics, collecting light scattered over a range of 45° – 95° . Air surrounding the instrument passes freely through its open sensing chamber and its measurement ranges cover mass concentrations from 0.01 to $100 \text{ mg}/\text{m}^3$.

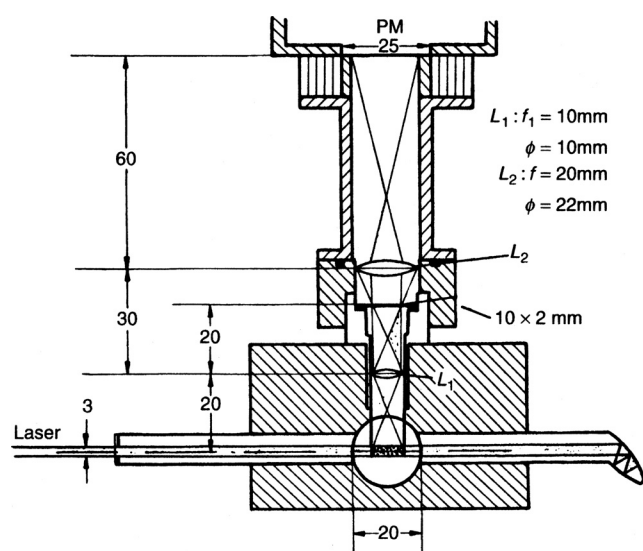


Figure 13-19 Photometer for aerosol inhalation studies.

A further step of development of real-time aerosol monitoring is the personal/Data RAM (*MIE*). This instrument is also available in a model (pDR-1200, *MIE*) using active sampling of aerosol through a size selective device to allow monitoring of respirable, thoracic and PM-2,5 fractions of environmental aerosols (see Chapters 25, 26, and 27).

Filter efficiencies can be checked within the linearity range of a photometer by measuring the concentrations of uniform test aerosols upstream and downstream of a filter by means of light scattering on an assembly of particles. In the case of high-efficiency filters, however, integral photometry requires a relatively high concentration upstream of the filter so that the use of an OPC or DMA is more reasonable.

Atmospheric Aerosol Measurement Common mass concentration levels for respirable as well as total dusts in workplaces are in the range $0.1\text{--}100\text{ mg/m}^3$, whereas typical aerosol mass concentrations in the atmosphere cover the range from $10\text{ }\mu\text{g/m}^3$ to about $200\text{ }\mu\text{g/m}^3$ (Charlson et al. 1967). Therefore, particulate pollution monitoring in the atmosphere requires nephelometers of high sensitivity. The integrating nephelometer was modified by Charlson et al. (1967) for air pollution and visibility studies. Its main component is a 0.15-m diameter, 2-m-long pipe containing all optical and sampling elements. The light source is a xenon flashlamp mounted on the pipe wall and powered at a rate of 1.2 flashes/s. An opal glass in front of the lamp provides a cosine characteristic of the light source. At one end of the pipe, a photomultiplier is mounted rigidly behind a series of collimating disks. The opposite end serves as a light trap, which is also constructed with collimating disks. Sample air is drawn through the central chamber at a flow rate of about $1.7 \times 10^{-3}\text{ m}^3/\text{s}$ [100 L/min]. The output from the phototube, a pulse of about $20\text{ }\mu\text{s}$, is amplified and averaged over time. The device has sufficient sensitivity to distinguish gases on the basis of their Rayleigh scattering so that different particle-free gases can be used to calibrate the instrument in terms of scattering cross sections. The results indicate that for aged atmospheric aerosols (accumulation mode), light scattering is proportional to the mass concentration of suspended particles (Charlson et al. 1967).

A newer generation of integrating nephelometers based on the same principle as described by Charlson et al. (1967), was developed by *TSI*. Model 3551 is a high-sensitivity, one-wavelength ($\lambda = 0.55\text{ }\mu\text{m}$) instrument that determines the scattering coefficient σ_s of atmospheric aerosol particles. The scattering coefficient is given by

$$\sigma_s = \int n(a)C_{\text{sca}}(a) da \quad (\text{Eq. 13-63})$$

Because of its high sensitivity, the nephelometer can measure scattering coefficients as low as $2 \times 10^{-7}\text{ m}^{-1}$. In

addition to Model 3551, *TSI* offers another model (Model 3563) using three wavelengths and a backscatter option. It is designed for short- and long-term measurements of the light-scattering coefficient σ_s of atmospheric aerosols, including visibility and air quality studies.

13.6 OPTICAL MEASUREMENT TECHNIQUES: *IN SITU* SENSING

13.6.1 Introduction

In the broadest sense, the instruments available for characterizing particles can be divided into two classes: extractive, hence *ex situ*, and *in situ*. In extractive sampling, a particle-laden volume of gas is removed from its environment and transported to a separate location where the particle measurement is made. Many of the most common aerosol measurement techniques operate in this mode, as described in previous sections, as it allows the careful control of the conditions under which the measurement is made. The success of extractive techniques, however, relies on the ability to sample and transport particles without biasing the properties of interest. This condition is sometimes difficult to meet. Inlet inefficiencies, wall losses, and rapid aerosol dynamics (evaporation, condensation, coagulation) are examples of physical processes that can alter the particle size distribution. Extractive techniques can also fail when measurements need to be made in hostile environments: extremes in pressure or temperature, reactive or corrosive environments, and so on. *In situ* (noninvasive) measurement techniques can overcome many of these limitations, allowing particle characterization under conditions where extractive techniques are not suitable.

Most of the *in situ* aerosol measurement techniques currently available are optically based, as the combination of optical imaging and laser illumination has provided a wealth of measurement possibilities. In fact, such a wide array of *in situ* optical techniques are available that it is necessary to limit the scope of the present review in three ways. First, we restrict discussion to instruments that are commercially available. This is a fairly strict limitation, as the laboratory development of new noninvasive particle characterization techniques is an area of active research. This decision was motivated by the desire to promote techniques which are: (1) readily available to the reader (without undue investment in hardware or time), and (2) reasonably portable. Even using commercial techniques, the researcher will find that these systems are generally expensive and require significant investments in time for training. Portability is desirable as many aerosol measurements must be made in field environments.

As a second limitation, we generally consider only real-time or direct-reading equipment. This is not a serious restriction, as the majority of *in situ* techniques readily lend

themselves to on-line analysis and presentation. It should be noted, of course, that subsequent (and more sophisticated) data analysis is often essential to ensure data integrity. One exception is that holography is considered. Although holograms must be first developed and later reconstructed for analysis, automated techniques are beginning to appear and so this powerful technique has been included. Finally, we restrict discussion to techniques that provide size distribution measurements; excluded by this restriction are techniques that provide only limited information about the particle cloud. One example is a transmissometer that is capable of measuring either particle volume concentration or Sauter mean diameter (Holve and Self 1980).

In short, this section reviews commercially available, direct-reading, optically based, *in situ* aerosol measurement instruments. Among them, capabilities exist for measurement of individual particle sizes from about 0.1 to above 1000 μm , concentrations as high as 10^6 cm^{-3} , and speeds in the kilometer/second range. Ensemble techniques can measure mean diameters as low as 1 nm. While *in situ* instruments overcome many of the limitations encountered with extractive methods, they do suffer (as a class and individually) from a wide range of new limitations. To describe these limitations, the next section provides an overview of *in situ* optical particle sizing systems. The section continues with a review of the instruments that are currently commercially available to the researcher. The individual reviews are by necessity short, but sufficient references are provided to help the reader to explore each method further. Although every effort has been made to include all of the available equipment, some manufacturers may have been overlooked. The section concludes with a discussion on the crucial topic of performance verification, including the issues of standards, calibration generators, and instrument comparisons.

13.6.2 Overview

The *in situ* measurement of particles by optical methods has been an area of active research. Thus, many excellent reviews are available on the topic (Hirleman 1983, 1984, 1988; Hovenac 1987; Lefebvre 1989; Tayali and Bates 1990; Black et al. 1996; Koo and Hirleman 1996). Several sets of proceedings contain current applications and discussions of *in situ* techniques (Gouesbet and Grehan 1988; Hirleman 1990; Hirleman et al. 1990; Kuo 1996).

It is helpful to divide optical *in situ* techniques into two general classes, based on whether they analyze single particle events or aggregate cloud properties. Single particle counters (SPCs) generally make a size determination on one particle at a time by analyzing its scattering behavior while it passes through a well defined (usually small) volume of high intensity (usually laser) light. Intensity, phase, or image information in the scattered light have all been used for particle sizing. A size distribution is obtained by sizing a number of

particles sufficient to ensure statistical accuracy. This class of instruments is similar in principle to the extractive, optical techniques covered in the previous chapter, except that the measurement volume is now located external to the instrument. Single particle counters generally provide a wealth of information on the counted particles, providing correlations among particle properties such as size, velocity, and time of arrival, and allowing spatial characterization of the particle field. At high number concentrations, however, single particle-counting techniques suffer from coincidence errors, which occur when more than one particle occupies the sensing volume at the same instant.

The second class of *in situ* systems, collectively called ensemble techniques, generally operates by illuminating a volume containing a large number of particles and analyzing the collective scattering. An illustrative example of an ensemble technique would be a photographic snapshot (or a hologram in 3D), which captures the state of a particle distribution at one instant in time. A drawback of photographic systems is that it is difficult to obtain a real-time readout of results. Real-time ensemble techniques are available that remedy this limitation, but require a mathematical inversion of the data to determine the size distribution. Ensemble techniques are well suited for measurements at high particle concentration, but become ineffective at low concentration. Generally, ensemble techniques do not provide as detailed information as SPCs, since individual particle information is lost in the averaging. Real-time ensemble techniques provide only limited spatial resolution of the particle field.

Generally, ensemble techniques measure particle concentration (number/volume), while SPC systems measure particle flux (number/area/time) (Hirleman 1988). That is, ensemble techniques report the number (and sizes) of particles present in the sampling volume over the measurement time (spatial averaging), whereas SPCs report the number (and sizes) of particles *passing through* the sampling volume during the measurement time (temporal averaging). To obtain aerosol concentration, SPCs require additional particle velocity information. As Hirleman (1988) points out, the distributions measured by concentration- or flux-based techniques will differ if a systematic correlation exists between particle size and velocity.

As each SPC or ensemble particle-sizing technique offers distinct strengths and weaknesses, an ideal instrument can only be defined in terms of measuring a specific set of properties for a specific aerosol in a specific environment. In this vein, Hovenac (1987) and Hirleman (1988) outline an approach to *in situ* optical sizing in terms of instrument operating envelopes. The central idea is that the choice of instrument must be a two step process: first, identify the particle properties that need to be measured and the conditions under which the measurement must be made, and second, establish that these conditions fall within the instrument's operating envelope. The final step is critical. As Hirleman

(1988) points out, many instruments will continue to “merrily report erroneous data and not notify the user.” An instrument operating envelope will be defined by the ability of the instrument to measure the desired property over an appropriate range to an acceptable accuracy. Hirleman (1988) groups the parameters that comprise the operating envelope into three domains: particle, instrument, and environmental properties. Based on Hirleman’s scheme, a general overview of the operating envelopes of *in situ* methods follows.

13.6.2.1 Particle Properties A variety of particle properties can be of interest, including size, shape, concentration, velocity, and index of refraction. Each of these properties can be distributed among a population of particles, and the problem becomes one of measuring the related distributions. With nonspherical particles, an ambiguity arises in selecting a dimension to characterize particle size. Moreover, most measurement techniques actually infer particle size indirectly from an observation of some particle behavior (settling speed, light-scattering intensity, etc.). Thus, size distribution measurements must be reported in terms of equivalent diameters: optical, aerodynamic, hydrodynamic, or electric mobility equivalent diameters are commonly reported. Care must be taken even when comparing among optical techniques, as the scattering behavior of the same particle will depend greatly on the details of the measurement technique used to observe it. Besides size, the particle concentration (number, surface area, or mass of particles per unit volume of gas) is also frequently of interest. A further complication arises as all particle properties can show spatial or temporal variation.

Measurement of particle size distributions demands that both particle sizing and counting be accomplished with great accuracy. High spectral resolution is required when the size distribution is itself of fundamental importance. For example, an exact description of the size distribution can be essential in understanding or predicting physical processes or in identifying origin or formation mechanisms. In some settings, however, accuracy may be less important than reproducibility. Typically, the mean size, the spread, and the shape of the distribution are all of interest. Ideally, the selected instrument’s sizing range should suitably span the actual particle size range. This can complicate the characterization of wide distributions, as particle sizing over more than one order of magnitude in size is difficult to cover with one instrument in one configuration. The distribution’s behavior at its tails can be important, particularly when transforming from a frequency to a mass weighted distribution.

A second property of interest is particle concentration: aerosol mass, area, and number per volume of gas are each of interest in some context. The ranges of concentrations that are encountered in particle measurement is impressive, ranging from a few particles per cubic meter in ultraclean areas to trillions of particles per cubic meter in some industrial settings. Obviously, one technique cannot be expected to

cover this entire range. In most situations, it is impractical (or impossible) to characterize every particle present; thus, it becomes necessary to infer the true aerosol properties from a measurement of some subset. Difficulties arise when the particles are only present in small numbers, as is typical at larger sizes or in clean environments. Instrument noise (phantom counts) can become important under this condition, and an effort must be made to ensure statistical significance. Instrument limitations also become evident at high concentrations, as will be discussed in Section 13.6.2.2. Concentration measurement errors can be amplified when extrapolating volume or mass distributions from measured frequency distributions.

The particle velocity distribution can be important in understanding dispersal, transport, or flux. In some applications, the correlation between particle size and velocity is desired. Even when particle velocity is not of interest itself, it may be a limiting factor in system performance. For example, particles moving at high speeds can pose signal-processing and response-time difficulties in SPCs. If the electronics are not fast enough, the signal from a high-speed particle will broaden and its intensity peak will diminish; the result is that the particle is undersized. Size-velocity correlations can also adversely influence system performance. Generally, SPCs provide particle velocity information while ensemble systems do not (a notable exception being pulsed photography or holography). For SPCs, a velocity measurement is typically required to infer particle concentration from the measured distribution of particle size: otherwise, faster particles will be counted preferentially in a flux-based measurement. Lower limits for particle velocity in SPCs are discussed by Hovenac (1987), upper limits are typically about 300 m/s but some systems can operate in the kilometer per second range.

Particle shape and index of refraction are less commonly of interest to the researcher, but are always important through their role in determining a particle’s scattering characteristics. Note that some of the imaging systems discussed below are capable of recording particle shape.

13.6.2.2 Instrument Properties An accurate determination of a particle size distribution requires that the instrument must both size and count particles accurately. Hovenac (1987) describes factors that adversely effect SPC sizing and counting performance. Although both size and count sensitivity are crucial for ensemble techniques as well, the discussion is complicated by the averaging nature of the measurement. The discussion below focuses on the measurement limits imposed by instrument features.

Perhaps the most difficult aspect of making an accurate *in situ* measurement is in defining the sample volume, as particle velocities and trajectories cannot be controlled as in sampling-type instruments (Holve 1980). This difficulty applies to both ensemble and SPC techniques, and can lead

to both sizing and counting errors. For most *in situ* systems, the sample volume is determined by the intensity profile of the illuminating beam and by the geometry and characteristics of the receiving optics (apertures, stops, lenses, filters, etc.). Laser beam intensity nonuniformities within the sampling volume (in either the axial or radial directions) result in trajectory-dependent scattered intensity profiles for even monodisperse particles. For the common case of a laser beam with a Gaussian intensity profile, a particle passing through the axis of a laser beam will scatter more light than if it passed through the edge of the beam. Thus, a small particle passing through the beam axis and a large particle passing through the beam edge could give comparable scattering amplitudes ("trajectory ambiguity," Grehan and Gouesbet 1986). For intensity-based SPC techniques, such multivalued response degrades instrument accuracy. Moreover, the combination of a nonuniform beam profile and photodetector sensitivity creates the situation where the effective sample volume becomes size dependent, for example, small particles are detected only by passing through the central portion of the beam whereas large particles are detected over a much larger cross section. Both ensemble and SPC *in situ* techniques can suffer this counting bias, and all SPCs require some form of sample volume correction (e.g., Holve and Self 1979a,b; Holve 1980).

One of the key parameters of interest is particle size. Several issues arise with regard to particle sizing with *in situ* techniques: precision (repeatability), accuracy (resolution), sensitivity (lowest detectable size), and dynamic range. One requirement for sizing accuracy is a monotonic response curve (intensity or phase versus size); unfortunately, light-scattering techniques are frequently multivalued due to Lorenz-Mie scattering effects (see Section 13.6.3.1). Variations in particle shape and refractive index effects can dramatically affect the shape of the response curve, and will limit system accuracy unless calibrations or calculations are performed with similar particles. Many *in situ* optical systems are based on near-forward scattering techniques, which minimize (but do not eliminate) shape and refractive index effects. The trajectory ambiguity discussed above also degrades accuracy for intensity-based techniques. All optical *in situ* techniques require that the laser beam waist be 4–5 times the size of the largest particle to ensure nominally uniform illumination over the particle's surface (Holve 1980). For example, Hovenac (1987) has shown for SPCs that a single large particle in a small beam could be counted as two smaller ones. Making the linear dimensions of the measurement volume much larger than the largest particles also reduces the fraction of particles that suffer edge effects (Holve and Self 1979a). Note that enlarging the measurement volume can increase coincidence errors, and so trade-offs must be made.

Lens imperfections, misalignment, electronic and photodetector nonlinearities, and other nonidealities can

significantly degrade all aspects of system performance (Holve and Davis 1985). Beam intensity fluctuations and system misalignment transients can impair both instrument precision and accuracy. As a rule of thumb, optical and signal-processing limitations generally limit the dynamic size range that can be measured (with one instrument at one setting) to about a factor of 30. Instrument noise is frequently a limiting factor in determining dynamic range, and can also influence precision, accuracy, and sensitivity.

There is always a desire for improved instrument sensitivity. For *in situ* SPCs, a lower detection limit of about 0.3 μm is typical, although sampling type SPCs can currently detect particles to about 0.05 μm . Knollenberg (1985) describes theoretical detection limits for SPCs and shows that the limit is dominated by background scattering from stray light or gas molecules present in the sampling volume. Interestingly, operating SPCs in vacuum can improve instrument sensitivity by a factor of 2–6 (Knollenberg 1985). In summary, Knollenberg places the theoretical limit for SPCs operating in air or vacuum at around 0.02 μm . Some ensemble techniques offer much lower detection limits, for example, 0.01 μm for dynamic light scattering.

High particle concentrations can also limit system performance. For example, in SPCs this can lead to coincidence, dead time, and intensity attenuation errors. Coincidence occurs when two particles occupy the measuring volume at the same time and are counted as a single large particle, resulting in both a sizing and counting error and consequently skewing the size distribution to larger sizes. Coincidence places an upper limit on the number concentration that can be measured without significant interference for a given system configuration. This upper limit has been shown to be proportional to the probability of interference and inversely proportional to the effective measurement volume (Holve 1980). Dead time occurs when the electronics are not ready when an event occurs because a previous event is still being analyzed; dead time effects can reduce or skew the measured size distribution. High particle concentrations between the sample volume and the receiving optics can reduce the intensity of light scattered by the particle. The resulting error in intensity-based techniques would be to undersize all particles. In ensemble systems, multiple particle scattering occurs at high concentrations. In this case, measurements of the size distribution become concentration dependent. Corrections for coincidence, dead time, or multiple scattering can often be made using either hardware or software.

All of the techniques discussed in this review require sophisticated data analysis, and most require a full inversion or deconvolution to finally resolve the desired size and number distributions. Real-time ensemble instruments demonstrate the classic case of inverting a finite set of measured responses to infer an unknown distribution (Hirleman 1988). For intensity-based SPC techniques, Holve (1980)

has discussed the need to deconvolve the resulting intensity histograms to account for trajectory ambiguity. Although beam intensity variations have minimal effect on particle sizing with phase-Doppler techniques, corrections still need to be made to account for size-velocity correlations and size-dependent sample volumes when concentration is required. The importance of proper data analysis or inversion cannot be overemphasized. Some of the problems and pitfalls of data analysis and inversion are presented in Chapter 22.

The use of exposed laser illumination by most of these systems poses eye safety concerns. Most of the systems use low-power lasers, but focusing can generate dangerous intensity levels. Proper laser safety operations are essential, and should be considered in instrument selection, location, and operation.

13.6.2.3 Environmental Properties Refractive index gradients along the optical path can cause beam steering, with a resulting change in optical collection angles. The length of the optical path, and medium temperature and pressure gradients determine the extent of beam steering. Gas conditions (temperature, pressure, composition) also affect the gas refractive index. Laser systems are readily adaptable to high temperature environments, as they can mitigate the influence of high thermal radiation background. There are also practical issues like optical access and window contamination that must be considered. Also, application of optical techniques in environments with high ambient light levels can lead to spurious measurements unless suitably filtered.

13.6.3 Single Particle Counters: Intensity-Based

This first class of instruments sizes and counts individual particles as they pass through an illuminated sample volume. As the particles pass through this region, they scatter light which is collected over some solid angle by the receiving optics, and focused onto a photodetector (Fig. 13-20). The particle size is determined by the peak intensity of the scattered light. A variety of such techniques are now available, and many reviews of the topic are available (Knollenberg 1979, 1981; Holve et al. 1981; Hovenac 1987; Tayali and Bates 1990; Black et al. 1996; Koo and Hirleman 1996). All of the limitations and concerns reported for SPCs in the overview apply to this class of techniques, including counting statistics at low concentrations and coincidence and dead time effects at high concentrations. In particular, nonuniformities in the illuminating beam can result in both sizing and counting errors for this class of equipment, and some form of correction (either hardware or analytic deconvolution) is required. Intensity-based techniques are particularly sensitive to environmental features that alter either illuminating beam or scattered light intensities, such as window contamination

or high particle densities between the sample volume and collection optics.

13.6.3.1 Forward-Scattering Spectrometer Probe The forward-scattering spectrometer probe (FSSP) models (*PMS*) are ground-based or aircraft-mountable probes that size particles based on the intensity of forward-scattered light as they pass through a laser-illuminated sensing volume. The newer model FSSP-300 provides better sensitivity (down to 0.3 μm) and higher resolution (31 channels) over its range (0.3–20 μm) than the mechanically identical FSSP-100 (15 channels over several size ranges, such as 0.5–8.0 and 5.0–95 μm). The velocity operating range for these instruments is from about 10–125 m/s. In the typical configuration, a particle velocity distribution is not measured by the FSSP. However, an option is available that converts the running mean particle transit time (measured to correct for edge effects) into a mean velocity. The system has been used extensively in atmospheric aerosol studies (e.g., Knollenberg 1981).

The operating principles for the FSSP-100 have been described by Knollenberg (1981), and for the FSSP-300 by Baumgardner et al. (1992). A patented dual-detector arrangement is used to size only those particles passing through a prescribed sampling volume. Briefly, the sampling volume between two probe tips is illuminated by a HeNe laser from one of the tips. When a particle enters the volume, it scatters light, which is collected by optics located in the other probe tip. While a dump spot blocks the main beam, the forward-scattered light enters a beam-splitting prism and is focused onto two photodetectors. The signal photodetector is unmasked and reports an intensity maximum used to size the particle, while the annulus detector is masked to eliminate light from in-focus, centered particles. A comparison between the two signals for each particle is used as an acceptance criterion: particles passing far from the focal plane scatter a larger proportion of light into the annular detector and are rejected. A transit time test is also performed to eliminate particles traversing the beam near an edge. This test can bias the size distribution, particularly for broad distributions with size-dependent particle velocities (Baumgardner et al. 1990).

Several authors have reviewed the optical and electronic limitations of the FSSP technique (Baumgardner et al. 1990, 1992; Wendisch et al. 1996). Issues addressed include sample volume, sizing, and counting uncertainties. Concentration measurement uncertainties can be quite large (>50%; e.g., Knollenberg 1981), although correction algorithms can be applied to improve accuracy (Baumgardner et al. 1990). Size calibration studies using latex and glass spheres (Pinnick et al. 1981) and water droplets (Wendisch et al. 1996) have been reported. Later, Hovenac and Hirleman (1991) developed a rotating pinhole calibrator for use with the FSSP. Investigators have shown that experimental FSSP calibration curves are in reasonably good agreement with

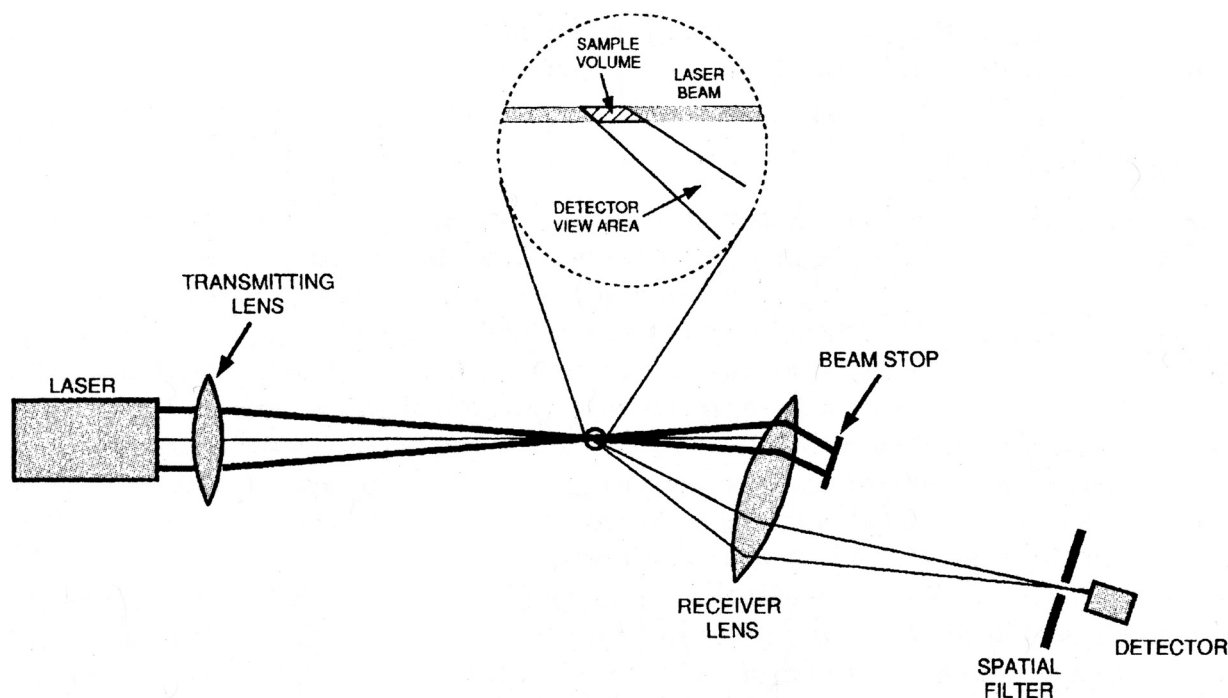


Figure 13-20 Example of a single particle light-scattering system.

Mie calculations if particle refractive index and shape (Jaenicke and Hanusch 1993) and beam nonuniformities (Hovenac and Lock 1993) are considered.

13.6.3.2 90° White Light-Scattering Analyzers A description of an *in situ* SPC based on white light illumination and detection at 90° scattering angle was given by Umhauer (1983). The choice of white light illumination is intended to maximize monotonicity of the scattering intensity versus diameter response curve, and to reduce (though not eliminate) index of refraction effects. These white light systems are well suited to filter efficiency testing, especially at high pressures or temperatures, and have also been used widely in pharmaceutical spray sizing. The velocity operating range is typically from 0.1 to 10 m/s although particle velocities are not measured. Commercial systems based on the Umhauer design have been marketed as the HC series particle sizers by *PLY* (now discontinued) and as the Model PCS-2000 series (*PAS*). Both manufacturers offered several models, differing in optical geometry and, hence, in nominal size and concentration ranges.

The discontinued HC series (*PLY*) provided configurations with particle size ranges from 0.4–22 μm (Model HC-2015) to 1.5–100 μm (Model HC-2470). The larger measurement volume required for the latter size range made the HC-2470 more susceptible to coincidence errors, but the system was less susceptible to edge errors (Borho 1970). Maximum concentrations achievable with the HC

series are in the range of 10^5 particles/ cm^3 . Performance of the HC series has been investigated in several calibration studies: Mitchell et al. (1989, according to British Standard BS3406), Fissan and Helsper (1981), Sachweh et al. (1998), and Friehmelt and Heidenreich (1999, nonspherical particles). These authors generally report smooth, monotonic instrument response functions in good agreement with Lorenz-Mie calculations for spheres, although a strong index of refraction effect was observed. Sachweh et al. (1998) modified an Umhauer-type system to achieve a smaller optical measurement volume, allowing measurements at concentrations up to $\sim 10^7$ particles/ cm^3 with a lower size detection limit of about 0.2 μm .

Depending on the configuration of the PCS-2000 system (*PAL*), the particle size range can be chosen within 0.15 and 100 μm for particle concentrations up to 10^6 particles/ cm^3 . PCS-2000 systems offer two independent photomultipliers to minimize border zone errors (i.e., trajectory ambiguity). Only a few studies of the PCS-2000 system have appeared in the literature. Stier and Quinten (1998) report on an index of refraction correction, and Maus and Umhauer (1996) used a PCS-like instrument in a filter study. Performance of PCS-2000 systems is expected to be generally similar to the HC series (*PLY*), based on their shared ancestry (Umhauer 1983).

13.6.3.3 Particle Counter Sizer Velocimeter (PCSV) The PCSV system (*PRM*) is a single particle counter that measures particle size based on the peak intensity of HeNe

laser light scattered in the near-forward direction (Holve and Self 1979a,b; see Fig. 13-20). Using near-forward-scattered (predominately diffracted) light helps reduce particle shape and refractive index effects; thus, instrument response is mainly dependent on particle cross-sectional area. Particle speed is determined from the widths of the scattered light pulses (Holve 1982). Only average speed is reported, although the entire speed distribution is recorded in the data set. Depending on the specific system configuration, the manufacturer gives the instrument's operating envelope as: particle size between about 0.2 and 200 μm , concentration up to 10^7 particles/ cm^3 for submicrometer and up to 100 ppm by volume for supermicrometer particles, and particle velocity between 0.1 and 400 m/s. A maximum particle count rate of 500 kHz is claimed for the system. To cover the wide range of sizes, two separate laser beams are used to form two independent measurement volumes; the narrower beam (nominal diameter of 20 μm) is used for sizing smaller particles, while the wider beam (nominal diameter of 200 μm) is used for sizing larger particles. Process Metrix (**PRM**) claims an accuracy of $\pm 5\%$ and a precision of $\pm 3\%$ of the indicated size. The system is available in both benchtop (PCSV-E) and probe (PCSV-P) fiber-coupled models. The water-cooled probe version is designed for operation in hostile environments (temperatures to 1400 $^\circ\text{C}$ and pressures from vacuum to 10 atmospheres) and provides gas purging to minimize window contamination. The benchtop version consists of two towers supported by a common bridge about one meter apart, with the measurement volume centrally located. Both systems contain *in situ* alignment systems to correct for beam steering in hostile environments (Holve and Annen 1984). Alignment sensitivity was explored analytically by Holve and Davis (1985).

A major feature of the PCSV system is the use of a deconvolution of the measured scattered intensity histogram to infer the size distribution (Holve and Self 1979a,b; Holve and Annen 1984; Holve and Davis 1985). The deconvolution is required due to the trajectory ambiguity. Generalized Lorenz-Mie scattering theory is used to predict the scattering response function (scattered intensity versus particle size) for the desired geometry, and has been experimentally confirmed (Holve and Self 1979b). Although early work characterized the intensity profile of the sample volume experimentally (Holve 1980), the current technique relies on an analytic description (Holve and Davis 1985) to generate the profile and a single point calibration to bring predicted and observed instrument response into agreement. The validity of the sample volume analytic model was experimentally checked with monodisperse latex spheres (Holve and Davis 1985), and the accuracy of the deconvolution algorithm was established using a mixture of monodisperse oleic acid droplets (Holve and Self 1979b). **PRM** provides a rotating chrome on glass reference reticle for instrument calibration in the 2- to 80- μm size range.

PCSV systems have been used to measure particle size distributions in a variety of combustion environments (Holve 1980; Holve and Annen 1984; Bonin and Queiroz 1996, 1991). Measurements of soda-lime glass beads in both cold and hot flows (Holve and Self 1979b) gave self-consistent results, showing the PCSV's ability to size particles in flames at temperatures of 1600 K. More recently, the PCSV has been used to study plating processes (Bonin et al. 1995).

13.6.3.4 Dual-Beam and Top-Hat Beam Systems

Several techniques have been developed that attempt to provide intensity-based particle sizing that does not depend on the particle trajectory through the beam, thus avoiding deconvolution algorithms. To reduce trajectory ambiguity, investigators have either used two-beam systems or have tried to modify the intensity profile of a single incident beam.

Dual-beam, two-color, or pointer-beam techniques typically employ one beam, which has a relatively wide diameter, and a second, coincident beam focused to a smaller waist coaxial with the larger beam. The light-scattering signal from the smaller (pointer) beam is used to trigger an intensity measurement from the larger beam, which is used for particle sizing. For example, Hess (1984) describes and demonstrates measurements made with a two-color system using a small pointing beam inside a larger Gaussian laser beam of a different wavelength. The pointing beam defines a relatively uniform portion of the large Gaussian beam. Particles are only measured when detected by the pointing beam, indicating that they are in the uniform portion of the outer beam, so the scattered pedestal intensity can be recorded and the size calculated free of trajectory ambiguity. The MetroLaser PAS-100 and PAS-200 (**MEL**) instruments use a similar technique to provide a uniform measurement region for combined LDV, particle sizing, and concentration measurements. The system can be configured to collect diffracted light in cases where the particles are of unknown shape or refractive index, and is designed to operate with no dead time, by collecting groups of particle-scattering events before processing the raw data. The manufacturer-stated operating envelope includes a 0.4- to 6000- μm diameter range, with 2% typical resolution and a 30:1 dynamic range, and a velocity range up to 1000 m/s. Data rates up to 3×10^6 particles/sec can be measured.

Grehan and Gouesbet (1986) describe a laboratory system in which a particle sizing laser beam was modified to a uniform (top-hat) profile using a Gaussian absorption filter. The top-hat concept reduces trajectory ambiguity by creating a beam of nearly constant laser intensity across most of the beam width. Of course, the realized intensity distribution of a top-hat beam is not uniform across the entire beam width, but is characterized by a constant intensity region in the center surrounded by Gaussian-like (intensity decaying) tails towards the beam edge. Thus, some trajectory ambiguity

is still present because of the tails. Black et al. (1996) provide additional discussion of the top-hat beam technique. Note that the present authors are not aware of a commercially available top-hat beam system.

13.6.3.5 Single Particle Counters: Laser Doppler Velocimetry Visibility Based Laser Doppler velocimetry (LDV) is a well-established and documented technique for noninvasive measurement of particle velocities, made by measuring the Doppler-shifted frequency of light scattered by individual particles passing through a laser beam-defined measurement volume (Durst et al. 1981). The most common LDV configuration uses crossed laser beams to define a measurement volume with typical dimensions of the order 1 mm or less. Particles passing through the measurement volume scatter light with a Doppler shift proportional to the particle speed. Speeds as high as several hundred meters per second can be measured using conventional detection electronics. The scattered light intensity signal from each particle passage (“Doppler burst”) consists of a high-frequency Doppler component superimposed on a low-frequency “pedestal” component due to the Gaussian intensity distribution of the illuminating beams. After filtering out the low-frequency pedestal, the remaining component (Fig. 13-21) is the Doppler frequency, directly proportional to the particle velocity. The extent of modulation of the Doppler signal (ratio of the Doppler signal to the pedestal intensity) is called the signal “visibility.”

A number of particle measurement techniques have been developed based on the pedestal intensity or visibility of LDV signals. Jackson (1990) provides a review of interferometry-based droplet-sizing techniques, including on-axis LDV visibility measurements (diffraction dominated), off-axis LDV visibility measurements (refraction dominated), and phase Doppler techniques. Such techniques

are attractive since they can provide simultaneous measurement of single particle size and velocity. Ideally, the peak intensity of the Doppler burst would be directly related to particle size. However, the Gaussian nature of the illuminating beams complicates matters due to trajectory ambiguity.

Particle size determination based on signal visibility was theoretically established by Farmer (1972), and the technique was attractive as a particle’s size could be measured independently of its trajectory through the beam crossing. Recent reviews of the method are available (Jones 1999; Black et al. 1996). One limiting drawback of the technique is that the particle size-visibility relationship becomes oscillatory for larger sizes, thus limiting the available dynamic range (see Bachalo 1980; Durst et al. 1981; Takeo and Hattori 1990). For example, Jackson and Samuelsen (1987) compared phase Doppler and visibility-based interferometers in a spray system, and found that the phase-based systems offered broader size and velocity ranges. Consequently, phase-based interferometers have found wider application than visibility-based systems, and no commercially available visibility systems are known to the authors.

13.6.3.6 Single Particle Counters: Phase-Based The phase Doppler technique is an LDV-based method for simultaneous measurement of single particle size and velocity (see Hirleman 1996 for a historical review). This technique is not intensity dependent like the previous group of SPC techniques, and can therefore offer superior performance by minimizing effects such as beam attenuation or window fouling. A phase Doppler system measures the spatial and temporal frequency of the Doppler-shifted light scattered by individual particles passing through a laser beam-crossing measurement volume. Phase Doppler systems use multiple photodetectors to sample slightly different spatial portions of the light scattered by individual particles. Figure 13-21 demonstrates high-pass filtered Doppler bursts measured by two such detectors. The phase shift between the two signals is a measure of the scattered light spatial frequency, which can be directly related to the particle diameter, refractive index, and receiver geometry. The linear relationship between the spatial frequency of the scattered light and the particle diameter for fixed refractive index and receiver geometry can be shown using either Lorenz-Mie scattering theory (Saffman et al. 1984), geometrical optics (Bachalo and Houser 1984), or GLMT (Grehan et al. 1994). Particle velocity is related to the temporal frequency in the same manner as in conventional LDV. Figure 13-22 is a schematic layout of a generic phase Doppler system.

Particle sphericity is required since the phase shift is calculated for either rays refracted through spherical particles of known, constant refractive index or reflected off the surface of reflective particles. Preliminary work on measurement of nonspherical particles will be presented below.

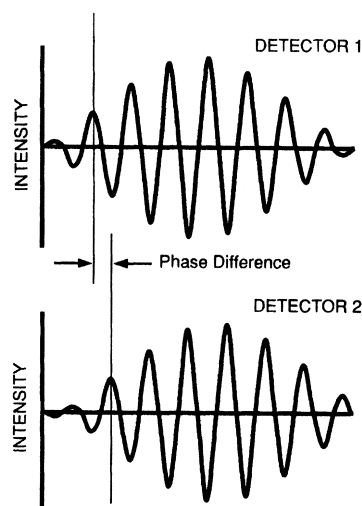


Figure 13-21 Characteristic Doppler burst signals.

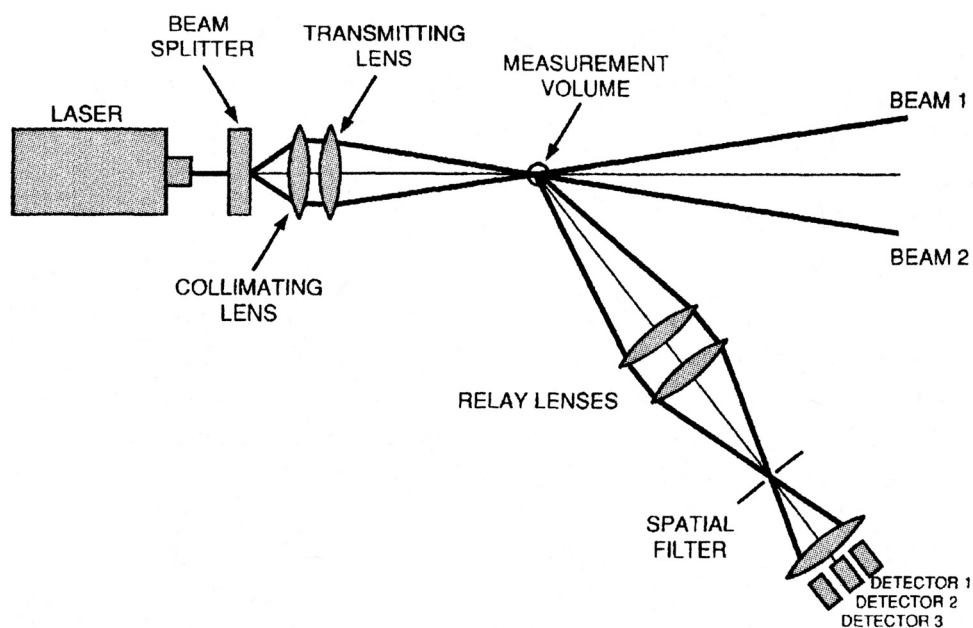


Figure 13-22 Layout of a phase Doppler system.

Most theoretical analyses of the Doppler phase shift have been performed using the geometric optics approximation, and neglecting diffraction, since scattered light is collected at sufficiently large off-axis angles (typically 30° or more). One of the key assumptions in phase Doppler analysis is that a single component of scattering, either refraction or reflection, dominates. Many authors have examined the effect of this assumption when it is violated by trajectory ambiguity, that is, in cases where scattering is first dominated by reflection when a particle's external surface enters the laser beam, then refraction as it passes through the beam center (e.g., Qiu et al. 2000; Strakey et al. 1998; Hardalupas and Liu 1997); these investigators and others have proposed and tested several post-processing trajectory correction routines.

13.6.3.7 Phase Doppler Particle Analyzer The fundamentals of the phase Doppler particle analyzer (PDPA) are described in Bachalo and Houser (1984). The PDPA (*AER*, *TSI*) consists of a laser, transmitting optics, receiver optics package, signal processors, and data collection and analysis software, with all operations, data collection, and analysis computer-controlled. The *TSI* system can be supplied to measure one, two, or three velocity components in addition to particle size. The manufacturer-stated operating envelope includes a 0.5- to 10,000- μm diameter range, with 1% typical accuracy and a 50:1 dynamic range, and a velocity range to over 500 m/s, with 0.2% typical accuracy. This system also calculates number density based on the number of particles passing through a calculated size-dependent measurement volume (to correct for trajectory ambiguity effects). The maximum measurable number density is $10^6/\text{cm}^3$.

13.6.3.8 Particle Dynamics Analyzer The particle dynamics analyzer (PDA; *DAN*) is described theoretically in Saffman (1987) and with applications in Saffman et al. (1984). This system is similar to the *TSI*/Aerometrics PDPA, except that signal phase is measured using a cross-correlation technique instead of a Fourier transform technique. The manufacturer-stated operating envelope for the PDA system includes a 0.5- to 10,000- μm size range, with 1% typical accuracy and a 40:1 dynamic range, and a velocity range to greater than 500 m/s, with 1% typical accuracy. The number density is so highly dependent on specifics of the application that customers are advised to refer to the open literature for specific concentration and mass flux limits for their application. *DAN* offers a dual PDA system that makes two simultaneous particle measurements in perpendicular planes in order to minimize trajectory ambiguity and slit effect (Xu and Tropea 1994) errors (see next section).

13.6.3.9 Phase Doppler Performance and Applications There has been an abundance of recent work with these instruments, both in instrument performance characterization and in applications in industrial and research settings. Note that many of the performance issues pertain to older instruments, many of which are still routinely used in industry and research; the newer generations of commercial instruments have been improved to address such concerns (e.g., frequency shift technique, photomultiplier gain optimization). Jackson (1990) presents an overview of the older AEM PDPA instrument, and discusses the effect of the rotating diffraction grating (formerly used as a combined beam splitter and frequency shifter, replaced on later models

with a beam splitter and Bragg cell frequency shifter) on PDPA concentration and velocity measurements. Dodge et al. (1987) performed liquid droplet measurements in sprays with the PDPA and noted that the PDPA was very sensitive to optical alignment. McDonell and Samuelsen (1990) performed an evaluation of the sensitivity of PDPA measurements to operator input parameters, specifically the photomultiplier tube (PMT) gain voltage and the frequency shift level. They found that mean velocity values were insensitive to PMT voltage and frequency shift, but that fluctuating velocities were strongly dependent on PMT voltage and somewhat dependent on frequency shift, because of wobble of the rotating diffraction grating. Volume flux measurement errors were caused by inconsistencies in determination of probe volume size, and by the strong influence of PMT voltage and the weak influence of frequency shift on particle sizing. They concluded that PDPA operations must be made with a carefully chosen standard operating procedure, and that a need exists for a reference calibration standard to guide operator selections of setup parameters for the PDPA instrument. Ceman (1990) and Bever and Hovenac (1999) have developed two different embodiments of such a standard calibration device (see discussion of performance verification in Section 13.7).

Dressler and Kraemer (1990) calibrated an older PDPA using a multi-jet droplet generator. They found PDPA measurement accuracy of about 5%. In addition, up to 5% measurement error could be caused by lens aberrations. They concluded that the PDPA system should be refocused for each different beam spacing to minimize lens spherical aberration errors. They also found that measurements were quite sensitive to the PMT gain voltage, in that a 50 V difference in gain voltage could lead to spurious data validations and artificially broadened distributions. They concluded that the lowest usable gain setting should be employed for measurements. Determination of this value can be difficult in measurements of unknown, transient particle distributions.

Ceman (1990) and Ceman et al. (1993) report detailed investigations into PDPA oleic acid droplet-sizing performance in the 2.3- to 25- μm range using a vibrating orifice aerosol generator and several different PDPA receiver geometries. They found that there were nonlinearities in PDPA measurements of particles below some critical diameter, in agreement with previous experiments (O'Hern et al. 1989; Ceman et al. 1990) and calculations (Al-Chalabi et al. 1988) using both Lorenz-Mie theory and geometrical optics. Saffman et al. (1984) found that a large receiver lens collection solid angle tended to damp these oscillations. Sankar et al. (1990) indicate that reflections from the surface of the droplet may also contribute to the oscillations in the phase versus diameter curve in the smaller diameter regime. Their work suggests that reflections can be minimized and linearity attained by

collecting light at an angle close to the droplet Brewster angle; however, Ceman's results show that droplet sizing oscillations can be substantially reduced by using a larger collection solid angle (shorter focal length receiver lens), but that working near the droplet Brewster angle provided little or no additional improvement. Gobel et al. (1998) examined the accuracy of phase Doppler particle sizing at 1 μm and below, and concluded that ambiguities exist but can be accounted for when sufficient information is available on the particles.

Alexander et al. (1985) used the PDPA for measurement of nonspherical methanol droplets produced by a vibrating orifice aerosol generator. The mean droplet diameters were 98 μm , with aspect ratios ranging from 0.7 to 1.4. The PDPA diameter measurements were very sensitive to aspect ratio, with the greatest error (45% oversizing) for elongated ellipsoids oriented perpendicular to the horizontal fringes in the PDPA measurement volume. Breña de la Rosa et al. (1989) have shown that the PDPA can be used to examine the shape of large nonspherical bubbles in water (1200- to 1800- μm diameter) by making separate measurement of the bubble major and minor diameters. This technique could possibly be extended to small particle measurements, although such an extension does not appear to be straightforward, especially for particles with rough or angular surfaces. Damaschke et al. (1998) experimentally and numerically analyzed the effects of nonspherical particles on phase measurement by the phase Doppler technique, demonstrating that nonspherical droplets can be a significant error source, especially for the standard three-detector systems. They suggested that alternative detector arrangements and larger measurement volumes may help minimize such errors.

The PDPA has been employed in a large number of applications. Strakey et al. (1998) examined use of the PDPA for measuring sprays from high pressure injectors. Their work included a careful analysis of probe volume dimensions smaller than the droplet diameters, and showed that such a device could perform well even in dense sprays, provided that phase and intensity validation, and probe volume correction algorithms were implemented. Van Den Moortel et al. (1997) applied PDPA to examine turbulent gas-solid flow in a circulating fluidized bed, and developed a post-processing routine to correct for artificially high count rates measured from noisy Doppler bursts. Hardalupas et al. (1988) used both AEM and custom-made phase Doppler devices to measure solid particles transported in a gas-solid dusty jet flow, and found that asphericity of the glass beads used as seed particles in the flow limited the measurement accuracy. Bachalo et al. (1990) presented details of PDPA operations including data analysis routines, and applied the PDPA to measurements of liquid spray droplets in both cold and combusting regimes. Droplet velocity time records showed

significant spray fluctuations, leading to droplet cluster formation.

13.6.4 Single Particle Counters: Imaging

Determining a particle's properties by direct imaging is among the earliest techniques used in particle measurement: consider the optical (and subsequently the electron) microscope. A significant advantage is that the shape and index of refraction issues that complicate single particle light-scattering measurements are avoided. In fact, imaging techniques provide one of the few avenues for investigating particle shape. The accuracy of single particle imaging systems is limited by Fresnel diffraction and depth-of-field effects (Hovenac 1987). Fresnel diffraction blurs image edges and complicates sizing. The depth-of-field effect arises from its dependence on particle size, with the result that large particles remain in focus over a greater axial distance than smaller ones.

Knollenberg (1970, 1979, 1981) designed an automated, *in situ*, single particle, optical imaging system that is commercially available (*PMS*) as the Optical Array Imaging Probe (OAP). In this family of probes, a collimated laser beam defines a measurement volume located between two sensing tips that extend forward from the main body of the system. Receiving optics direct the beam to illuminate a linear array of photodiodes. A particle passing through the measurement volume casts a shadow on the array, resulting in a decreased signal from the individual elements that lie in the shadow. Three methods are used to analyze the resulting data from the array: 1D, 2D, and grey level processing. In a 1D OAP system, the array elements are read and latched during the particle transit in a way that only provides particle size information. In a standard 2D OAP system, the entire 2D image of the particle is stored in high-speed memory as a series of "snapshots" of the particle during its transit. For each image, the status of each of the 32 elements in the photodiode array is recorded by one bit, indicating if the element is being shadowed or not. The great advantage of acquiring 2D particle images becomes apparent when measuring nonspherical particles. In the Grey Probe 2D OAP system, a 64-element array is used where each element reports one of four shadow levels. The increased sophistication of the Grey Probe provides twice the resolution (twice as many elements) of the standard 2D system, as well as providing depth-of-field information.

For all of these imaging systems, both instrument resolution and size range depend on physical spacing of the array elements, magnification, and particle velocity. Consequently, the user must identify the expected velocity range in order to properly configure the system. OAP probes also suffer from depth-of-field limitations, leading to erroneous

interpretation of out-of-focus (blurred) particle images. To characterize OAP performance, Hovenac and Hirleman (1991) and Reuter and Bakan (1998) used a rotating reticle calibrator; the latter authors proposed a depth-of-field correction that allowed accurate sizing (*rms* uncertainty less than 6%) of particles from 50 to 500 μm . In addition, OAP probes reject particles (resulting in counting bias) that shadow elements at either edge of the array, as the fraction of the particle falling outside the array cannot be determined and thus precludes correct sizing.

Rugged, pylon-mountable airborne versions of either the 1D, 2D, or grey probe OAP configurations are available for either cloud droplet or precipitation measurements. Particle sizing ranges and resolution depend on the particular models, which differ in the number of array elements and optical configuration used. The cloud-droplet models are suited to sizing smaller particles, with ranges such as 10–620 μm (with 10- μm resolution) or 200–6000 μm (with 200- μm resolution). The precipitation models are suited to sizing larger particles, with ranges such as 50–3100 μm (with 50- μm resolution) or 150–9300 μm (with 150- μm resolution). The resolution limits given above assume instrument operation at aircraft speeds (100 m/s); significant improvement in instrument resolution can be achieved at lower velocities. The lower limit for OAP sizing [somewhere between 1 and 10 μm according to Knollenberg (1979)] results from the vanishingly small depth-of-field at these sizes. Particle velocities are not measured explicitly, but could be recovered by later analysis of the image sequences using the known imaging frequency. A ground-based precipitation OAP also is available. The system is contained in a weatherized package, with the two sensing tips extending above the top. The distance between probe sensing tips is 50 cm, providing a large sampling area for measuring the droplets in free fall.

13.7 CONCLUSIONS

From the extent of the previous discussion, it is easy to see that there are a wide range of optical *in situ* techniques available for measuring particle size distributions. Although this variety makes it likely that a researcher will find at least one instrument that will perform the required measurement, it is essential that a careful selection process be pursued. Particular attention is required in determining the instrument operating envelope relative to the measurement requirements in order to find the technique best suited to the application. Performance verification should be made as needed to ensure data accuracy and instrument reliability. A tabulation of the various commercial techniques is given in Table 13-4. The authors have tried to include all vendors and equipment in these lists, but realize the field is extensive

TABLE 13-4 Listing of Selected Optical, *In Situ* Particle Size Measurement Systems and Their Characteristics

Method	Commercial Source	Measure Velocity	Comments
SPC intensity	<i>MEL</i>	LDV	PAS
SPC intensity	<i>PAL</i>	N	PCS-2000
SPC intensity	<i>PMS</i>	Y	FSSP, mean velocity option
SPC intensity	<i>PRM</i>	Y	PCSV (probe and bench)
SPC phase	<i>TSI</i>	LDV	PDPA
SPC phase	<i>DAN</i>	LDV	PDA
SPC imaging	<i>PMS</i>	Y	OAP
Ensemble imaging	<i>MEL</i>	Y	Custom holography
Ensemble diffraction	<i>CIL</i>	N	PSA (Particle Size Analyzer)
Ensemble diffraction	<i>MAL</i>	N	Spraytec and EPCS
Ensemble diffraction	<i>MCR</i>	N	Microtrac SRA, X-100
Ensemble diffraction	<i>SYM</i>	N	HELOS
Ensemble PCS	<i>BRK</i>	N	
Ensemble PCS	<i>BEC</i>	N	
Ensemble PCS	<i>MAL</i>	N	
Ensemble PCS	<i>PSS</i>	N	
Ensemble PCS	<i>WYA</i>	N	
Calibration	<i>BAN</i>	—	Standard reference particles
Calibration	<i>DUK</i>	—	Standard reference particles
Calibration	<i>SRD</i>	—	Standard reference particles
Calibration	<i>TSI</i>	—	Single-jet droplet generator

and considerable development efforts are always proceeding. We apologize for any omissions.

13.8 LIST OF SYMBOLS

Roman Symbols

a	particle radius
c_0	number concentration of the aerosol, Eq. 13-59
c_{\min}	lower limit of the detectable number concentration, Eq. 13-60
C_{abs}	absorption cross section, Eq. 13-11
C_{ext}	extinction cross section, Eq. 13-11
C_{sca}	scattering cross section, Eq. 13-5
$Cc(Kn)$	Cunningham correction factor

$dC_{\text{sca}}/d\Omega$

D

D

$E(m)$

$F(m)$

$g^{(2)}(t)$

I_{sca}

$I(q)$

k

k_0

Kn

l

m

n

$n(a)$

N

N_p

q

Q

Q_{absorsca}

P_{scat}

R_g

$R_{g,z}$

s

$S(q)$

t_r

u

α

η

θ and ϕ

ρ

λ

σ_s

τ

τ_c

ω

Ω

differential scattering cross section, Eq. 13-1

diffusion coefficient

fractal dimension, Eq. 13-43

absorption term, Eq. 13-33

Lorentz term, Eq. 13-24

intensity autocorrelation function, Eq. 13-54

scattered intensity, Eq. 13-2

Scattered intensity as a function of q

Boltzmann constant; wave vector

aggregate prefactor, Eq. 13-43

Knudsen number

photon mean free path, Eq. 13-48

relative index of refraction, Eq. 13-20

relative index of refraction, Eq. 13-20; number density

number weighted size distribution (Eq. 13-63)

number of monomers in an aggregate, Eq. 13-43

number of particle counts in OPC, Eq. 13-60

the scattering wave vector magnitude, Eq. 13-38

sample flow rate, Eq. 13-59

absorption or scattering efficiency, Eq. 13-7

power scattered, Eq. 13-2

radius of gyration

z-average radius of gyration, Eq. 13-53

Number of photon scattering events, Eq. 13-50

structure factor, Eq. 13-47

recovery time of electronics between successive count events, Eq. 13-59

dimensionless size, qa , Eq. 13-36

size parameter, Eq. 13-18

shear viscosity

the polar coordinates

phase shift parameter, Eq. 13-34b

wavelength

scattering coefficient, Eq. 13-63

turbidity, Eq. 13-10

correlation time, Eq. 13-56

albedo, Eq. 13-12

solid angle

13.9 REFERENCES

- Al-Chalabi, S.A.M., Hardalupas, Y., Jones, A.R., and Taylor, A.M.K.P. 1988. Calculation of calibration curves for the phase doppler technique: comparison between Mie theory and geometrical optics. In *Optical Particle Sizing*, eds. G. Gouesbet and G. Grehan, Plenum Press, New York, pp. 107–120.
- Alexander, D.R., Wiles, K.J., Schaub, S.A., and Seeman, M.P. 1985. Effects of non-spherical drops on a phase doppler spray analyzer. In *Particle Sizing and Spray Analysis, SPIE Volume 573*, eds. N. Chigier and G.W. Stewart, SPIE, Bellingham, Washington, pp. 67–72.
- Altshuler, B., Yarmus, L., Palmes, E.d., and Nelson, N. 1957. Aerosol deposition in the human respiratory tract. *AMA Arch. Ind. Health* 15: 293–303.
- Armbruster, L., Breuer, H., Gebhart, J., and Neulinger, G. 1984. Photometric determination of respirable dust concentration without elutriation of coarse particles. *Part. Charact.* 1: 96–101.
- Bachalo, W.D. 1980. Method for measuring the size and velocity of spheres by dual-beam light-scatter interferometry. *Appl. Optics* 19(3): 363–370.
- Bachalo, W.D., and Houser, M.J. 1984. Phase doppler spray analyzer for simultaneous measurements of drop size and velocity distributions. *Opt. Eng.* 23: 583–590.
- Bachalo, W.D., Rudoff, R.C., and Sankar, S.V. 1990. Time-resolved measurements of spray drop size and velocity. In *Liquid Particle Size Measurement Techniques*, 2 ed., ASTM STP 1083, eds. E.D. Hirleman, W.D. Bachalo, and P.G. Felton, American Society for Testing and Materials, Philadelphia, pp. 209–224.
- Baumgardner, D., Cooper, W.A., and Dye, J.E. 1990. Optical and electronic limitations of the forward-scattering spectrometer probe. In *Liquid Particle Size Measurement Techniques*, 2 ed., ASTM STP 1083, eds. E.D. Hirleman, W.D. Bachalo, and P.G. Felton, American Society for Testing and Materials, Philadelphia, pp. 115–127.
- Baumgardner, D., Dye, J.E., Gandrud, B.W., and Knollenberg, R.G. 1992. Interpretation of measurements made by the forward scattering spectrometer probe (FSSP-300) during the airborne arctic stratospheric expedition. *J. Geophys. Res.* 97(D8): 8035–8046.
- Berg, M.J., Sorensen, C.M., and Chakrabarti, A. 2005. Patterns in Mie scattering: Evolution when normalized by the Rayleigh cross section. *Applied Optics* 44: 7487–7493.
- Berg, M.J., Sorensen, C.M., and Chakrabarti, A. 2008a. Extinction and the optical theorem. Part I. Multiple particles. *J. Opt. Soc. Am. A* 25: 1504–1513.
- Berg, M.J., Sorensen, C.M., and Chakrabarti, A. 2008b. Extinction and the optical theorem. Part II. Single particles. *J. Opt. Soc. Am. A* 25: 1514–1520.
- Berglund, R.N., and Liu, B.Y.H. 1973. Generation of monodisperse aerosol standards. *Environ. Sci. Technol.* 7: 147–153.
- Berne, B., and Pecora, R. 1976. *Dynamic Light Scattering*. John Wiley and Sons, New York.
- Bever, S.J., and Hovenac, E.A. 1999. Reticle for verification of the correct operation of the phase Doppler particle analyzer. *Opt. Eng.* 38(10): 1730–1734.
- Black, D.L., McQuay, M.Q., and Bonin, M.P. 1996. Laser-based techniques for particle-size measurement: A review of sizing methods and their industrial applications. *Prog. Energy Combust. Sci.* 22: 267–306.
- Bohren, C.F., and Huffman, D.R. 1983. *Absorption and Scattering of Light by Small Particles*, John Wiley and Sons, New York.
- Bonin, M.P., Flower, W.L., Renzi, R.F., and Peng, L.W. 1995. Size and concentration measurements of particles produced in commercial chromium plating processes. *J. Air Waste Management* 45: 902–907.
- Bonin, M.P., and Queiroz, M. 1991. Local particle velocity, size, and concentration measurements in an industrial-scale pulverized coal-fired boiler. *Combust. Flame* 85: 121–133.
- Bonin, M.P., and Queiroz, M. 1996. A parametric evaluation of particle-phase dynamics in an industrial pulverized-coal-fired boiler. *Fuel* 75(2): 195–206.
- Borho, K. 1970. A scattered-light measuring instrument for high dust concentrations. *Staub Reinhalt. Luft* 30: 45–49.
- Born, M., and Wolf, E. 1975. *Principles of Optics*, Pergamon Press, Oxford.
- Breña de la Rosa, A., Sankar, S.V., Weber, B.J., Wang, G., and Bachalo, W.D. 1989. A theoretical and experimental study of the characterization of bubbles using light scattering interferometry. In *ASME International Symposium on Cavitation Inception—1989*, eds. W.B. Morgan and B.R. Parkin, American Society of Mechanical Engineers, New York, pp. 63–72.
- Büttner, H. 1983. Kalibrierung einer Streulichtmesseinrichtung zur Partikelgrößenanalyse mit Impaktoren. *Chemie Ing. Technol.* 55: 65–76.
- Cai, J., Lu, N., and Sorensen, C.M. 1995. Analysis of fractal cluster morphology parameters: structural coefficient and density autocorrelation function cutoff. *J. Colloid Interface Sci.* 171: 470–473.
- Ceman, D.L. 1990. Phase Doppler technique: Factors affecting instrument response and novel calibration system. Master of Science thesis, The University of New Mexico, Albuquerque.
- Ceman, D.L., O'Hern, T.J., and Rader, D.J. 1990. Phase Doppler droplet sizing—Scattering angle effects. In *ASME Fluid Measurements and Instrumentation Forum*, eds. E.P. Rood and C.J. Blechinger, American Society of Mechanical Engineers, New York, pp. 61–63.
- Ceman, D.L., Rader, D.J., and O'Hern, T.J. 1993. Calibration of the phase Doppler particle analyzer with monodisperse droplets. *Aerosol Sci. Technol.* 18: 346–358.
- Charlson, R.J., Horvath, H., and Pueschel, R.F. 1967. The direct measurement of atmospheric light scattering coefficient for studies of visibility and pollution. *Atmos. Environ.* 1: 469–478.
- Chen, B.T., Cheng, Y.S., and Yeh, H.C. 1984. Experimental response of two optical particle counters. *J. Aerosol Sci.* 15: 457–464.
- Chowdhury, D., Taylor, T., Sorensen, C.M., Merklin, J.F., and Lester, T.W. 1984. Application of photon correlation

- spectroscopy to flowing Brownian motion systems. *Appl. Optics* 23: 4149–4154.
- Clark, W.E., and Avol, E.L. 1979. An evaluation of the Climet 208 and Royco 220 light-scattering optical particle counters. In *Aerosol Measurement*, eds. D.A. Lundgren, F.S. Harris, W.H. Marlow, M. Lippmann, W.E. Clark, and M.D. Durham, University Press of Florida, Gainesville, FL, p. 219.
- Dahneke, B.E. 1983. *Measurement of Suspended Particles by Quasi-Elastic Light Scattering*, John Wiley and Sons, New York.
- Damaschke, N., Gouesbet, G., Grehan, G., Mignon, H., and Tropea, C. 1998. Response of phase Doppler anemometer systems to nonspherical droplets. *Appl. Optics* 37(10): 1752–1761.
- Dodge, L.G., Rhodes, D.J., and Reitz, R.D. 1987. Drop-size measurement techniques for sprays: Comparison of Malvern laser-diffraction and Aerometrics phase/Doppler. *Appl. Optics* 26: 2144–2154.
- Draine, B.T. 1988. The discrete-dipole approximation and its application to interstellar graphite grains. *Astrophys. J.* 333: 848–872.
- Draine, B.T., and Flatau, P.J. 1994. Discrete-dipole approximation for scattering calculations. *J. Opt. Soc. Am. A* 11: 1491–1499.
- Dressler, J.L., and Kraemer, G.O. 1990. A multiple drop-size drop generator for calibration of a phase-Doppler particle analyzer. In *Liquid Particle Size Measurement Techniques*, 2 ed., ASTM STP 1083, eds. E.D. Hirleman, W.D. Bachalo, and P.G. Felton, American Society for Testing and Materials, Philadelphia, pp. 30–44.
- Durst, F., Melling, A., and Whitelaw, J.H. 1981. *Principles and Practice of Laser-Doppler Anemometry*, Academic, London.
- Farias, T.L., Koylu, U.O., and Carvalho, M.G. 1996. Range of validity of the Rayleigh-Debye-Gans theory for optics of fractal aggregates. *Appl. Opt.* 35: 6560–6567.
- Farmer, W.M. 1972. Measurement of particle size, number density, and velocity using a laser interferometer. *Appl. Opt.* 11: 2603–2612.
- Ferri, F. 1997. Use of a charge couple device camera for low-angle elastic light scattering. *Rev. Sci. Instr.* 68: 2265–2274.
- Fissan, H.J., and Helsper, C. 1981. Calibration of the Polytec CH-15 and HC-70 optical particle counters. In *Aerosols in the Mining and Industrial Work Environments*, vol. 3, eds. V.A. Marple and B.Y.H. Liu, Ann Arbor Science, Ann Arbor, MI, pp. 825–831.
- Fissan, H., Helsper, C., and Kasper, W. 1984. Calibration of optical particle counters with respect to particle size. *Part. Charact.* 1: 108–111.
- Fissan, H., and Schwientek, G. 1987. Sampling and transport of aerosols. *TSI J. Part. Instrum.* 2(2): 3–10.
- Flower, W.L. 1983. Optical measurements of soot formation in premixed flames. *Combust. Sci. Technol.* 33: 17–33.
- Forrest, S.R., and Witten, T.A. 1979. Long-range correlations in smoke-particle aggregates. *J. Phys. A* 12: L109–L117.
- Friehmelt, R., and Heidenreich, S. 1999. Calibration of a white light/90° optical particle counter for aerodynamic size measurements. *J. Aerosol Sci.* 30: 1271–1279.
- Gebhart, J. 1989a. Funktionsweise und Eigenschaften Optischer Partikelzähler. *Technisches Messen im* 56: 192–203.
- Gebhart, J. 1989b. Dosimetry of inhaled particles by means of light scattering. In *Extrapolation of Dosimetric Relationships for Inhaled Particles and Gases*, eds. J. Crapo, F.J. Miller, J.A. Graham, and A.W. Hayes, Academic New York, pp. 235–245.
- Gebhart, J. 1991. Response of single-particle optical counters to particles of irregular shape. *Part. Syst. Charact.*, 8: 40–47.
- Gebhart, J., Heyder, J., Roth, C., and Stahlhofen, W. 1980. Herstellung und Eigenschaften von Latex-Aerosolen. *Staub-Reinhalt. Luft.* 40: 1–8.
- Gebhart, J., Blankenberg, P., Bormann, S., and Roth, C. 1983. Vergleichsmessungen an optischen Partikelzählern. *Staub-Reinhalt. Luft.* 43: 439–447.
- Gebhart, J., and Roth, C. 1986. Background noise and counting efficiency of single optical particle counters. In *Aerosols, Formation and Reactivity, Proceedings of the 2nd International Aerosol Conference*, 22–26 September, Berlin. Pergamon, New York.
- Gebhart, J., Heigwer, G., Heyder, J., Roth, C., and Stahlhofen, W. 1988. The use of light scattering photometry in aerosol medicine. *J. Aerosol Med.* 1: 89–112.
- Gebhart, J. 2001. Optical direct-reading techniques: Light intensity systems. In *Aerosol Measurement. Principles, Techniques, and Application*, eds. P.A. Baron and K. Willeke, Wiley-Interscience, New York, pp. 419–454.
- Gobel, G., Wriedt, T., and Bauckhage, K., 1998. Micron and sub-micron aerosol sizing with a standard phase-Doppler anemometer. *J. Aerosol Sci.* 29(9): 1063–1073.
- Gouesbet, G., and Grehan, G. (eds.) 1988. *Optical Particle Sizing*, Plenum Press, New York.
- Grehan, G., and Gouesbet, G. 1986. Simultaneous measurements of velocities and sizes of particles in flows using a combined system incorporating a top-hat beam technique. *Appl. Optics* 25: 3527–3538.
- Grehan, G., Gouesbet, G., Naqwi, A., and Durst, F. 1994. Trajectory ambiguities in phase Doppler systems: Study of a near-forward and a near-backward geometry. *Part. Part. Syst. Charact.* 11(12): 133–144.
- Hardalupas, Y., and Liu, C.H. 1997. Implications of the Gaussian intensity distribution of laser beams on the performance of the phase Doppler technique sizing uncertainties. *Prog. Energy Combust. Sci.* 23: 41–63.
- Hardalupas, Y., Taylor, A.M.K.P., and Whitelaw, J.H. 1988. Measurements in heavily-laden dusty jets with phase-Doppler anemometry. In *Transport Phenomena in Turbulent Flows: Theory, Experiment, and Numerical Simulation*, eds. M. Hirata and N. Kasagi, Hemisphere, New York, pp. 821–835.
- Hecht, E. 1987. *Optics*. Addison-Wesley, Reading, MA.
- Helsper, C., and Fissan, H.J. 1980. Response characteristics of a Polytec HC-15 optical particle counter. 8th Annual Meeting Gesellschaft f. Aerosolforschung, Schmallenberg, Germany.
- Hess, C.F. 1984. Nonintrusive optical single particle counter for measuring the size and velocity of droplets in a spray. *Appl. Optics* 23: 4375–4382.

- Heyder, J. 1994. Biomedical aerosol research. In *Proceedings of the 4th International Aerosol Conference*, 29 August–2 September, Los Angeles, California.
- Hinds, W., and Reist, P.C. 1972. Aerosol measurement by laser Doppler spectroscopy. *Aerosol Sci.* 3: 501–514.
- Hinds, W.C., and Kraske, G. 1986. Performance of PMS model LAS-X optical particle counter. *J. Aerosol Sci.* 17: 67–72.
- Hirleman, E.D. 1983. Nonintrusive laser-based particle diagnostics. *Progress in Astronautics and Aeronautics* vol. 92, pp. 177–207.
- Hirleman, E.D. 1984. Particle sizing by optical, nonimaging techniques. In *Liquid Particle Size Measurement Techniques*, ASTM STP 848, eds. J.M. Tishkoff, R.D. Ingebo, and J.B. Kennedy, American Society for Testing and Materials, Philadelphia, pp. 35–60.
- Hirleman, E.D. 1988. Optical techniques for particle size analysis. *Laser Topics* 10: 7–10.
- Hirleman, E.D. (ed.) 1990. *Proceedings of the Second International Congress on Optical Particle Sizing*, Arizona State University Printing Services, Tempe, AZ.
- Hirleman, E.D. 1996. History of development of the phase-Doppler particle-sizing velocimeter. *Part. Part. Syst. Charact.* 13: 59–67.
- Hirleman, E.D., W.D. Bachalo, and P.G. Felton (eds.). 1990. *Liquid Particle Size Measurement Techniques*: 2 ed., ASTM STP 1083, American Society for Testing and Materials, Philadelphia.
- Holve, D.J. 1980. *In situ* optical particle sizing technique. *J. Energy* 4(4): 176–183.
- Holve, D.J., and Annen, K.D. 1984. Optical particle counting, sizing, and velocimetry using intensity deconvolution. *Opt. Eng.* 23: 591–603.
- Holve, D.J., and Davis, G.W. 1985. Sample volume and alignment analysis for an optical particle counter sizer, and other applications. *Appl. Optics*. 24: 998–1005.
- Holve, D.J., and Self, S.A. 1979a. Optical particle sizing for *in situ* measurements. Part 1. *Appl. Optics*. 18: 1632–1645.
- Holve, D.J., and Self, S.A. 1979b. Optical particle sizing for *in situ* measurements. Part 2. *Appl. Optics*. 18: 1646–1652.
- Holve, D., and Self, S.A. 1980. Optical measurements of mean particle size in coal-fired MHD flows. *Combustion and Flame* 37: 211–214.
- Holve, D.J., Tichenor, D., Wang, J.C.F., and Hardesty, D.R. 1981. Design criteria and recent developments of optical single particle counters for fossil fuel systems. *Opt. Eng.* 20: 529–539.
- Holve, D.J. 1982. Transit Timing Velocimetry (TTV) for Two-Phase Reacting Flows. *Combustion and Flame* 48: 105–108.
- Hovenac, E.A. 1987. *Performance and Operating Envelope of Imaging and Scattering Particle Sizing Instruments*, NASA CR-180859, National Aeronautics and Space Administration, Lewis Research Center, Cleveland, OH.
- Hovenac, E.A., and Hirleman, E.D. 1991. Use of rotating pinholes and reticles for calibration of cloud droplet instrumentation. *J. Atmos. Oceanic Technol.* 8: 166–171.
- Hovenac, E.A., and Lock, J.A. 1993. Calibration of the FSSP: Modeling scattering from a multimode laser beam. *J. Atmos. Oceanic Technol.* 10: 518–525.
- Hubbard, J., Eckles, J., and Sorensen, C.M. 2008. Q-space analysis applied to polydisperse, dense random aggregates. *Particle & Particle Systems Characterization* 25: 68–73.
- Jackson, T.A. 1990. Droplet sizing interferometry. In *Liquid Particle Size Measurement Techniques*, 2 ed., ASTM STP 1083, eds. E.D. Hirleman, W.D. Bachalo, and P.G. Felton, American Society for Testing and Materials, Philadelphia, pp. 151–169.
- Jackson, T.A., and Samuelsen, G.S. 1987. Droplet sizing interferometry: A comparison of the visibility and phase/Doppler techniques. *Appl. Optics* 26: 2137–2143.
- Jaenicke, R., and Hanusch, T. 1993. Simulation of the optical particle counter forward scattering spectrometer probe 100 (FSSP-100). *Aerosol Sci. Technol.* 18: 309–322.
- Jones, A.R. 1999. Light scattering for particle characterization. *Progr. Energy Combust. Sci.* 25: 1–53.
- Jullien, R., and Botet, R. 1987. *Aggregation and Fractal Aggregates*, World Scientific, Singapore.
- Kerker, M., Smith, L.B., Matijeric, E., and Farone, W.A. 1964. Determination of particle size by the minima and maxima in the angular dependence of the scattered light. Range of validity of the method. *J. Colloid Sci.* 19: 193–200.
- Kerker, M. 1969. *The Scattering of Light and Other Electromagnetic Radiation*, Academic, New York.
- Kim, W., Sorensen, C.M., and Chakrabarti, A. 2004. Universal occurrence of soot aggregates with a fractal dimension of 2.6 in heavily sooting laminar diffusion flames. *Langmuir* 20: 3969–3973.
- Kim, W., Sorensen, C.M., Fry, D., and Chakrabarti, A. 2006. Soot Aggregates, Superaggregates and Gel-Like Networks in Laminar Diffusion Flames. *J. Aerosol Sci.* 37: 386–401.
- King, G., Sorensen, C.M., Lester, T.W., and Merklin, J.F. 1982. Photon correlation spectroscopy used as a particle size diagnostic in sooting flames. *Appl. Optics* 21: 976–978.
- Knollenberg, R.G. 1970. The optical array: An alternative to scattering or extinction for airborne particle size determination. *J. Appl. Meteor.* 9: 86–103.
- Knollenberg, R.G. 1979. Single particle light scattering spectrometers. In *Aerosol Measurement*, eds. D.A. Lundgren, F.S. Harris, W.H. Marlow, M. Lippmann, W.E. Clark, and M.D. Durham, University Press of Florida, Gainesville, FL, pp. 271–293.
- Knollenberg, R.G. 1981. Techniques for probing cloud microstructure. In *Clouds: Their Formation, Optical Properties, and Effects*, eds. P.V. Hobbs and A. Deepak, Academic, New York, pp. 15–89.
- Knollenberg, R.G. 1985. The measurement of particle sizes below 0.1 micrometers. *J. Environ. Sci.* 28: 32–47.
- Knollenberg, R.G. 1989. The measurement of latex particle sizes using scattering ratios in the Rayleigh scattering size range. *J. Aerosol Sci.* 20: 331–345.
- Knollenberg, R.G., and Luehr, R. 1976. Open cavity laser active scattering particle spectrometry from 0.05 to 5 microns. In *Fine Particles*, ed. B.Y.H. Liu, Academic Press, New York, pp. 669–696.

- Koo, J.H., and Hirleman, E.D. 1996. Review of principles of optical techniques for particle size measurements. In *Recent Advances in Spray Combustion: Spray Atomization and Drop Burning Phenomena*, vol. 1, ed. K.K. Kuo, American Institute of Aeronautics and Astronautics, Reston, VA, pp. 3–32.
- Koylu, U.O., and Faeth, G.M. 1994a. Optical properties of overfire soot in buoyant turbulent diffusion flames at long residence times. *Journal of Heat Transfer* 116: 152–159.
- Koylu, U.O., and Faeth, G.M. 1994b. Optical properties of soot in buoyant laminar diffusion flames. *Journal of Heat Transfer* 116: 971–979.
- Kuo, K.K. (ed.) 1996. *Recent Advances in Spray Combustion: Spray Atomization and Drop Burning Phenomena*, vol.1, American Institute of Aeronautics and Astronautics, Reston, VA.
- Lattuada, M., Wu, H., and Morbidelli, M. 2003. A simple model for the structure of fractal aggregates, *Jour. Coll. and Interface Sci.* 268: 106–120.
- Lefebvre, A.H. 1989. *Atomization and Sprays*, Hemisphere, New York, pp. 367–409.
- Lieberman, A. 1986. Evolution of optical airborne particle counters in the U.S.A. In *Aerosols: Formation and Reactivity, Proceedings of the 2nd International Aerosol Conference*, 22–26, September, Berlin, Pergamon, New York, pp. 590–593.
- Lilienfeld, P. 1983. Current mine dust monitoring developments. In *Aerosols in the Mining and Industrial Work Environments*, eds. V.A. Marple and B.Y.H. Liu, Ann Arbor Science Publishers, Ann Arbor, MI, pp. 733–757.
- Liu, B.Y.H., Berglund, R.N., and Agarwal, J.K. 1974. Experimental studies of optical particle counters. *Atmos. Environ.* 8: 717–732.
- Liu, B.Y.H., Marple, V.A., Whitby, K.T., and Barsic, N.J. 1974a. Size distribution measurement of airborne coal dust by optical particle counters. *Am. Ind. Hyg. Assoc. J.* 8: 443–451.
- Liu, B.Y.H., and Pui, D.Y.H. 1974b. A submicron aerosol standard and the primary absolute calibration of the condensation nucleus counter. *J. Colloid Interf. Sci.* 47: 155–171.
- Liu, B.Y.H., and Szymanski, W.W. 1986. On sizing accuracy, counting efficiency and noise level of optical particle counters. In *Aerosols, Formation and Reactivity. Proceedings of the 2nd International Aerosol Conference*, 22–26, September, Berlin, Pergamon, New York, pp. 603–606.
- Liu, B.Y.H., and Szymanski, W.W. 1987. Counting efficiency, lower detection limit and noise level of optical particle counters. In *Proceedings of the 33rd Annual Meeting of IES*, San Jose, CA.
- Liu, B.Y.H., Szymanski, W.W., and Ahn, K.H. 1985. On aerosol size distribution measurements by laser and white light optical particle counters. *J. Environ. Sci.* 28: 19–24.
- Mackowski, D.W. 1991. Analysis of radiative scattering for multiple sphere configurations. *Proc. R. Soc. Lond. A. Mat.* 433: 599–614.
- Mackowski, D.W. 1994. Calculation of total cross sections of multiple-sphere clusters. *J. Opt. Soc. Am. A.* 11: 2851–2861.
- Mackowski, D.W., and Mishchenko, M.I. 1996. Calculation of the T matrix and the scattering matrix for ensembles of spheres. *J. Opt. Soc. Am. A.* 13: 2266–2278.
- Mäkynen, J., Hakulinen, J., Kivistö, T., and Lektimäki, M. 1982. Optical particle counters: Response, resolution and counting efficiency. *J. Aerosol Sci.* 13: 529–535.
- Mandelbrot, B. 1983. *The Fractal Geometry of Nature*, Freeman, San Francisco, CA.
- Maron, S.H., and Elder, M.E. 1963. Determination of latex particle size by light scattering I. Minimum intensity method. *J. Colloid Sci.* 18: 107–118.
- Marple, V.A., and Rubow, K.L. 1976. Aerodynamic particle size calibration of optical particle counters. *J. Aerosol Sci.* 7: 425–433.
- Maus, R., and Umhauer, H. 1996. Determination of the fractional efficiencies of fibrous filter media by optical in situ measurements. *Aerosol Sci. Technol.* 24: 161–173.
- McDonnell, V.G., and Samuelsen, G.S. 1990. Sensitivity assessment of a phase-Doppler interferometer to user-controlled settings. In *Liquid Particle Size Measurement Techniques: 2 ed.*, ASTM STP 1083, eds. E.D. Hirleman, W.D. Bachalo, and P.G. Felton, American Society for Testing and Materials, Philadelphia, pp. 170–189.
- Minneart, M.G.J. 1993. *Light and Color in the Outdoors*, Springer-Verlag, New York.
- Mitchell, J.P., Nichols, A.L., and van Santen, A. 1989. The characterization of water-droplet aerosols by Polytec optical particle analysers. *Part. Part. Syst. Charact.* 6: 119–123.
- Mishchenko, M.I., Travis, L.D., and Lacis, A.A. 2002. *Scattering, Absorption and Emission of Light by Small Particles*, Cambridge University Press, Cambridge.
- Mokhtari, T., Sorensen, C.M., and Chakrabarti, A. 2005. Multiple scattering effects on optical structure factor measurements. *Appl. Opt.* 44: 7858–7861.
- Oh, C., and Sorensen, C.M. 1997. The effect of monomer overlap on the morphology of fractal aggregates. *J. Colloid Interface Sci.* 193: 17–25.
- O'Hern, T.J., Rader, D.J., and Ceman, D.L. 1989. Droplet sizing calibration of the phase Doppler particle analyzer. In *ASME Fluid Measurements and Instrumentation Forum*, eds. E.P. Rood and C.J. Blechinger, American Society of Mechanical Engineers, New York, pp. 49–51.
- Okazaki, K., and Willeke, K. 1987. Transmission and deposition behaviour of aerosols in sampling inlets. *Aerosol Sci. Technol.* 7: 275–83.
- Pesic, P. 2005. *Sky in a Bottle*, MIT Press, Cambridge, MA.
- Pierce, P.E., and Maron, S.H. 1964. Prediction of minima and maxima in intensities of scattered light and of higher order Tyndall spectra. *J. Colloid Sci.* 19: 658–672.
- Pinnick, R.G., Garvey, D.M., and Duncan, L.D. 1981. Calibration of Knollenberg FSSP light-scattering counters for measurement of cloud droplets. *J. Appl. Meteor.* 20: 1049–1057.
- Plomb, A., Alderliesten, P.T., and Galjee, F.W. 1986. On calibration and performance of laser optical particle counters. In *Aerosols*,

- Formation and Reactivity, Proceedings of the 2nd International Aerosol Conference*, 22–26, September, Berlin, Pergamon, New York, pp. 594–598.
- Qiu, H.-H., Hsu, C.T., and Sommerfeld, M. 2000. High accuracy optical particle sizing in phase-doppler anemometry. *Meas. Sci. Technol.* 11: 142–151.
- Rader, D.J., and O'Hern, T.J. 2001. Optical direct-reading techniques: In situ sensing. In *Aerosol Measurement. Principles, Techniques, and Application*, eds. P.A. Baron and K. Willeke, Wiley-Interscience, New York, 455–494.
- Reist, P. 1990. Mie theory calculations for your PC. Order: R. Enterprises, 205 Glenhill Lane, Chapel Hill, NC 27514, USA.
- Reuter, A., and Bakan, S. 1998. Improvements of cloud particle sizing with a 2D-grey probe. *J. Atmos. Oceanic Technol.* 15: 1196–1203.
- Rieker, T.P., Hanprasopwattana, A., Datye, A., and Hubbard, P. 1999. Particle size distribution inferred from small-angle x-ray scattering and transmission electron microscopy. *Langmuir* 15: 638–641.
- Roth, C., and Gebhart, J. 1978. Rapid particle size analysis with an ultra-microscope. *Microscopica Acta* 81: 119–129.
- Sachweh, B., Büttner, H., and Ebert, F. 1989. Improvement of the resolution and the counting accuracy of an optical particle counter by fast digital signal recording. *J. Aerosol Sci.* 20: 1541–1544.
- Sachweh, B., Umhauer, H., Ebert, F., Büttner, H., and Friehmelt, R. 1998. In situ optical particle counter with improved coincidence error correction for number concentrations up to 10^7 particles cm^{-3} . *J. Aerosol Sci.* 29: 1075–1086.
- Saffman, M. 1987. Optical particle sizing using the phase of LDA signals. *Dantec Information, Measurement and Analysis* 5: 8–13.
- Saffman, M., Buchave, P., and Tanger, H. 1984. Simultaneous measurement of size, concentration and velocity of spherical particles by a laser doppler method. In *Second International Symposium on Applications of Laser Anemometry to Fluid Mechanics*, eds. R.J. Adrian, D.F.G. Durão, F. Durst, H. Mishina, and J.H. Whitelaw, Ladoan, Lisbon, pp. 85–103.
- Sankar, S.V., Weber, B.J., Kamemoto, D.Y., and Bachalo, W.D. 1990. Sizing fine particles with the phase Doppler interferometric technique. In *Proceedings of the Second International Congress on Optical Particle Sizing*, ed. E.D. Hirtleman, Arizona State University Printing Services, Tempe, AZ, pp. 277–287.
- Scrivner, S.M., Taylor, T.W., Sorensen, C.M., and Merklin, J.F. 1986. Soot particle size distribution measurements in a premixed flame using photon correlation spectroscopy. *Appl. Optics* 25: 291–297.
- Sorensen, C.M., and Feke, G.D. 1996. The morphology of macroscopic soot. *Aerosol Sci. Tech.* 25: 328–337.
- Sorensen, C.M., and Roberts, G. 1997. The prefactor of fractal aggregates. *J. Colloid Interface Sci.* 186: 447–452.
- Sorensen, C.M., and Fischbach, D.E. 2000. Patterns in Mie scattering. *Opt. Commun.* 173: 145–153.
- Sorensen, C.M., and Shi, D. 2000. Guinier analysis for homogeneous dielectric spheres of arbitrary size. *Opt. Commun.* 178: 31–36.
- Sorensen, C.M., and Shi, D. 2002. Patterns in the ripple structure in Mie scattering. *JOSA* 19: 122–125.
- Sorensen, C.M. 2001. Light scattering from fractal aggregates. A review. *Aerosol Sci. Tech.* 35: 2648–2687.
- Sorensen, C.M., Kim, W., Fry, D., and Chakrabarti, A. 2003. Observation of soot superaggregates with a fractal dimension of 2.6 in laminar acetylene/air diffusion flames. *Langmuir* 19: 7560–7563.
- Stier, J. and Quinten, M. 1998. Simple refractive index correction for the optical particle counter PCS 2000 by Palas. *J. Aerosol Sci.* 29: 223–225.
- Strakey, P.A., Talley, D.G., Sankar, S.V., and Bachalo, W.D. 1998. The use of small probe volumes with phase Doppler interferometry. *Proceedings of ILASS Americas '98*, Sacramento, CA, May 17–20, 1998.
- Szymanski, W.W., and Liu, B.Y.H. 1986. On the sizing accuracy of laser optical particle counters. *Part. Charact.* 3: 1–7.
- Takeo, T., and Hattori, H. 1990. Visibility analysis of laser Doppler anemometry for spherical particles smaller than several light wavelengths. *Jpn. J. Appl. Phys.* 29: 419–426.
- Tanford, C. 1961. *Physical Chemistry of Macromolecules*, John Wiley and Sons, New York.
- Tayali, N.E., and Bates, C.J. 1990. Particle sizing techniques in multiphase flows: A review. *Flow Meas. Instrum.* 1: 77–105.
- Taylor, T., Scrivner, C., Sorensen, C.M., and Merklin, J.F. 1985. Determination of the relative number distribution of particle sizes using photon correlation spectroscopy. *Appl. Optics* 24: 3713–3717.
- Taylor, T.W. and Sorensen, C.M. 1986. Gaussian beam effects on the photon correlation spectrum from a flowing brownian motion system. *Appl. Optics* 25: 2421–2426.
- Tufto, P.A., and Willeke, K. 1982. Dependence of particulate sampling efficiency on inlet orientation and flow velocities. *Am. Ind. Hyg. Assoc. J.* 43: 436–443.
- Umhauer, H. 1980. Partikelgrößenbestimmung in Suspensionen mit Hilfe eines Streulichtzahlverfahrens. *Chemie Ing. Technol.* 52: 55–63.
- Umhauer, H. 1983. Particle size distribution analysis by scattered light measurements using an optically defined measuring volume. *J. Aerosol Sci.* 14: 765–770.
- Vandehulst, H.C. 1981. *Light Scattering by Small Particles*, Dover, New York.
- Vanden Moortel, T., Santini, R., Tadriss, L., and Pantaloni, J. 1997. Experimental study of the particle flow in a circulating fluidized bed using a phase Doppler particle analyser: A new post-processing data algorithm. *Int. J. Multiphase Flow* 23(6): 1189–1209.
- Vander Meulen, A., Plomp, A., Oeseburg, F., Buringh, E., van Aalst, R.M., and Hoevers, W. 1980. Intercomparison of optical particle counters under conditions of normal operation. *Atmos. Environ.* 14: 495–499.

- Wang, G.M., and Sorensen, C.M. 2002. Experimental Test of the Rayleigh-Debye-Gans theory for light scattering by fractal aggregates. *Applied Optics* 41: 4645–4651.
- Wen, H.Y., and Kasper, G. 1986. Counting efficiencies of six commercial particle counters. *J. Aerosol Sci.* 17: 947–961.
- Wendisch, M., Keil, A., and Korolev, A.V. 1996. FSSP Characterization with monodisperse water droplets. *J. Atmos. Oceanic Technol.* 13: 1152–1165.
- Westenberger, S., Gebhart, J., Jaser, S., Koch, M., and Köstler, R. 1992. A novel device for the generation and recording of aerosol micro-pulses in lung diagnostics. *J. Aerosol Sci.* 23(Suppl. 1): 449–452.
- Whitby, K.T., and Vomela, R.A. 1967. Response of single particle optical counters to nonideal particles. *Environ. Sci. Technol.* 1: 801–814.
- Willeke, K.T., and Liu, B.Y.H. 1976. Single particle optical counter: Principle and application. In *Fine Particles*, ed. B.Y.H. Liu, Academic, New York, pp. 697–729.
- Xu, T.-H., and Tropea, C. 1994. Improving the performance of two-component phase Doppler anemometers. *Meas. Sci. Technol.* 5: 969–975.
- Zimm, B.H. 1948. Apparatus and methods for measurement and interpretation of the angular variation of light scattering. *J. Chem. Phys.* 16: 1009–1116.